INTEGRATED MICROFLUIDIC SYSTEMS FOR DROPLET DETECTION AND SORTING

A THESIS SUBMITTED TO

THE GRADUATE SCHOOL OF ENGINEERING AND SCIENCE

OF BILKENT UNIVERSITY

IN PARTIAL FULFILLMENT OF THE REQUIREMENTS FOR

THE DEGREE OF MASTER OF SCIENCE

IN

MATERIALS SCIENCE AND NANOTECHNOLOGY

By

Pelin Kubra Isgor

September, 2015

I certify that I have read this thesis and that in my opinion it is fully adequate, in scope and in quality, as a thesis for the degree of Master of Science.

Assist. Prof. Dr. Çağlar Elbüken (Supervisor)

I certify that I have read this thesis and that in my opinion it is fully adequate, in scope and in quality, as a thesis for the degree of Master of Science.

Prof. Dr. Haluk Külah

I certify that I have read this thesis and that in my opinion it is fully adequate, in scope and in quality, as a thesis for the degree of Master of Science.

Assist. Prof. Dr. Yegân Erdem

Approved for the Graduate School of Engineering and Science:

Prof. Dr. Levent Onural
Director of Graduate School

ABSTRACT

INTEGRATED MICROFLUIDIC SYSTEMS FOR DROPLET DETECTION AND SORTING

Pelin Kubra Isgor
M.S. in Materials Science and Nanotechnology
Supervisor: Assist. Prof. Dr. Caglar Elbuken
September 2015

Microdroplet based microfluidic systems have gained a lot of attention during the last decades due to enhanced analytical performance, low cost and high-throughput. One of the fundamental requirements of a droplet based system is detection of droplets. Capacitive sensing of droplets have been used for droplet detection, however they lack the required sensitivity for droplet content detection. Here a portable, low cost, scalable and highly sensitive droplet content detection system is demonstrated using coplanar electrodes. The designed microfluidic system enables droplet content modification on the run. While changing droplet content, i.e., dielectric content, capacitive signal amplitude is measured. The system resolves 3 unit of dielectric permittivity. 5% material change in droplet is detected.

Following droplet content detection, sorting of laden droplets enables further experimentation with material of interest in the droplet. Dielectrophoresis is a commonly used method for droplet sorting. Dielectrophoretic sorting of droplets is demonstrated using two dimensional and there dimensional electrodes.

Low cost and portable electronic components are integrated with microfluidic devices for droplet content detection and sorting using microfabricated electrodes. The cost and signal to noise ratio of the system are aimed to be decreased by implementing detection and sorting system on a printed circuit board. Sensing and sorting electrodes are fabricated and all of the electronic components are placed on a printed circuit board. Microchannels are reversibly placed over electrodes, therefore the platform becomes reusable. This feature of the system enables various experimentation using microdroplets on the same base platform.

This approach will lead to microfluidic systems that are programmable and easy-to-use by means of off-the-shelf and low cost electronic components.

***Keywords**: droplet content sensing, droplet sorting, printed circuit board, integrated circuits, coplanar electrodes, dielectrophoresis*

ÖZET

DAMLACIK TANIMA VE AYRIŞTIRMA İÇİN ENTEGRE MİKROAKIŞKAN SİSTEMLER

Pelin Kübra İşgör
Malzeme Bilimi ve Nanoteknoloji Bölümü Yüksek Lisans
Tez Yöneticisi: Yrd. Doç. Dr. Çağlar Elbüken
Eylül 2015

Son zamanlarda, microdamlacık temelli mikroakışkan sistemler geliştirilmiş işlem yetenekleri, ucuz olmaları, ve kısa zamanda pek çok deneyi gerçekleştirebiliyor olmaları nedeniyle ilgi odağı olmaya başladı. Damlacık temelli sistemlerin gerekliliklerinden bir tanesi de damlacıkların sistem içinde tanınmasıdır. Literatürde damlacıkların kapasitif olarak belirlenmesine ait çalışmalar olmasına rağmen, bu çalışmalar damlacığın içinde yer alan malzemeyi tanımlayabilmek için gereken hassasiyete sahip değildir. Aynı düzlemde konumlandırılan elektrotlar ile taşınabilir, ucuz, ölçeklenebilir ve oldukça hassas bir damlacık tanıma sistemi bu tezde gösterilmiştir. Tasarlanan mikroakışkan sistem damlacık oluşurken içindeki malzemenin değiştirilmesine olanak sağlamaktadır. Damlacığın içeriği değiştirilirip, kapasitif olarak damlacıktan sinyal alınmıştır. Bu sistemim çözünürlüğü 3 birim dielektrik sabiti kadardır. Ayrıca, damlacığın içindeki yüzde beşlik değişim sistem tarafından algılanabilmektedir.

Damlacığın içinin tanınabiliyor olmasına ek olarak, içerisinde ilgilenenilen malzeme bulunan damlacıklar ayrıştırılarak daha fazla deneysel işlemin yapılmasına olanak sağlamaktadır. Damlacık ayrıştırma için dielektroforesis

yaygın olarak kullanılan bir yöntemdir. Bu tezde iki boyutlu ve üç boyutlu elektrotlar kullanılarak damlacıkların dielektroforetik olarak ayrıştırılması gösterilmiştir.

Ucuz ve kolaylıkla taşınabilir tümleşik devreler damlacık içini tanıma ve damlacığı ayrıştırma işlemleri için mikroakışkan sistemlerle birleştirilmiştir. Bunun için mikro boyutta üretilen elektrotlar kullanılmıştır. Bütün sistem baskı devre kartına taşınarak, maliyet ve sinyalin gürültüye oranının düşürülmesi amaçlanmıştır. Damlacık tanıma ve ayrıştırma için kullanılan elektrotlar ve bütün tümleşik devreler baskı devre kartına taşınmıştır. Mikrokanallar sistemin yeniden kullanılmasına olanak sağlayacak şekilde elektrotların üstüne yerleştirilmiştir. Sistemin bu özelliği, aynı platform üstünde damlacıkları kullanarak çeşitli deneylerin yapılmasına olanak sağlamaktadır.

Bu teknik kolayca bulunabilen ve oldukça ucuz elektronik parçaları kullanıyor olması sayesinde mikroakışkan sistemleri programlanabilir ve kolayca kullanılabilen platformlara dönüştürecektir.

Anahtar sözcükler: *damlacık içeriği tanıma, damlacık ayrıştırma, baskı devre kartı, tümleşik devreler, dielektroforesis*

Acknowledgement

I would like to acknowledge and thank European Union Marie Curie 7th Frame Programme (Project no. 322019) for the financial support throughout my M.Sc. studies. Also, I would like to thank TUBITAK (Project no. 213S127) for partial financial support.

Dedicated to my family

Mevlüde, Hasan and Aylin

and my grandmother

Cevriye

Table of Contents

CHAPTER 1 INTRODUCTION 1

1.1 MOTIVATION OF THE THESIS 1

1.2 OVERVIEW OF THESIS 3

CHAPTER 2 SCIENTIFIC BACKGROUND 4

2.1 WHAT IS MICROFLUIDICS ? 4

2.2 DROPLET-BASED MICROFLUIDIC SYSTEMS 6

2.2.1 DROPLET FORMATION 6

2.2.3 DROPLET BREAK-UP 9

2.2.4 DROPLET COALESCENCE 9

CHAPTER 3 FABRICATION AND CHARACTERIZATION METHODS ... 11

3.1 FABRICATION OF COPLANAR ELECTRODES AND PASSIVATION LAYER 11

3.1.1 PHOTOLITHOGRAPHY 12

3.1.2 THIN FILM METALLIZATION 13

3.1.2.1 SPUTTERING 13

3.1.2.2. THERMAL EVAPORATOR 14

3.1.3 DIELECTRIC FILM COATING 15

3.1.3.1 PLASMA ENHANCED CHEMICAL VAPOR DEPOSITION (PECVD) 15

3.2 FABRICATION OF MICROCHANNEL MOLD 15

3.3 SOFT LITHOGRAPHY 19

3.4 CHARACTERIZATION METHODS 22

3.4.1 ATOMIC FORCE MICROSCOPY (AFM) 22

3.4.2 VARIABLE ANGLE SPECTROSCOPIC ELLIPSOMETER 23

3.4.3 STYLUS PROFILOMETER 24

CHAPTER 4 DROPLET CONTENT DETECTION USING INTEGRATED CAPACITIVE SENSORS 25

4.1 INTRODUCTION 25

4.2 CAPACITIVE DETECTION THEORY 27

4.3 DESIGN AND FABRICATION OF THE MICROFLUIDIC DEVICE 32

4.3.1 Design of the Device 32
4.3.2 Fabrication of the device 33
4.4 Experimental Procedure 34
4.4.1 Experimental Set-up 34
4.4.2 Experimental Procedure 36
4.5 Results and Discussion 40
4.5.1 Analytical model comparison 40
4.5.2 Choosing the data rate 42
4.5.3 Finding proper electrode width 43
4.5.4 Signal enhancement through thinner passivation layer . 45
4.5.5 Droplet dielectric content measurement 47
4.5.6 Verification 50
4.6 Possible Future Applications 51
4.7 Conclusion 53
Chapter 5 Droplet Sorting Using 2D Coplanar and 3D EGaIn Electrodes 54
5.1 Introduction 54
5.2 Dielectrophoresis (DEP) Theory 57
5.3 Design and Fabrication 63
5.3.1 2D DEP device design and fabrication 63
5.3.2 3D EGaIn electrode and channel design and fabrication 67
5.4 Experimental Procedure 69
5.5 Results 72
5.6 Conclusion 75
Chapter 6 Droplet Detection and Sorting on a Printed Circuit Board (PCB) 76
Droplet Detection and Sorting on a Printed Circuit Board (PCB) 76
6.1 Introduction 76
6.2 Comsol Simulations 78

6.3 DESIGN AND FABRICATION 84
6.4 EXPERIMENTAL PROCEDURE 89
6.5 RESULTS 91
6.5.1 ON-PCB DROPLET CONTENT DETECTION 91
6.5.2 COMSOL SIMULATION RESULTS 93
6.6 CONCLUSIONS 100
CHAPTER 7 CONCLUSIONS 101
7.1 CONCLUSIONS 101
7.2 FUTURE WORK 102
7.3 CONTRIBUTIONS 103
BIBLIOGRAPHY 104

List of Figures

Figure 3.1. Schematic of mold fabrication using SU-8 negative photoresist... 19

Figure 4.1. Schematic of the system studied by Chen *et al*. [33]..... 28

Figure 4.2. Schematic of the system studied by Otter [34]. 29

Figure 4.3. Illustration of the capacitance formed by coplanar electrodes. a) Field lines through the passivation layer, microchannel and PDMS bulk. b) Capacitances through passivation layer (C_p) and microchannel (C_{ch}). Dielectric permittivities of materials are; $\varepsilon_{r\_water} = 80$, $\varepsilon_{r\_oil} = 2.5$, $\varepsilon_{r\_PDMS} = 2.5$, $\varepsilon_{r\_SiO2} = 3.85$. Effective width of the electrodes is shown as w_{eff}. 31

Figure 4.4. Schematic of the microfluidic device. The insets show the (a) droplet generation region and mixing region, (b) detection region..... 32

Figure 4.5. Photograph of the fabricated microfluidic device. Channels were filled with dye solutions for clarity. 34

Figure 4.6. a) Images of the droplet formation and their travel along the serpentine section in our system. b) Droplets before the mixing region. c) Droplets after mixing region, completely mixed. 35

Figure 4.7. Capacitance signal for varied DI ethanol mixtures (a) only DI, (b) 25% ethanol, (c) 50% ethanol, (d) 75% ethanol, (e) only ethanol. The real-time capacitance signal amplitude was displayed through the LabView interface and recorded when droplet enters to the detection region. Each peak corresponds to a single droplet in the sensing region. The plots show the data for 17 seconds. 38

Figure 4.8. Capacitance measurement system for verification purposes: (a) Close-up view of the electrodes and the reservoirs. Capacitance change is measured by pipetting 50 µl of solution, (b) the schematic of the complete

device with multiple electrodes, (c) photograph of the fabricated device, (d) exemplary capacitance change plot, (e) probe station for electrical connections. 39

Figure 4.9. Capacitance signal for DI droplets measured at different sampling rates of AD7746. 43

Figure 4.10. Capacitance change for electrodes with varying width. The coplanar electrodes were passivated by 375 nm thick SiO_2. The results were averaged over 50 droplets. 44

Figure 4.11. PDMS and toluene thinned PDMS thickness. PDMS thickness (red, square) for 5 min. spinning time and PDMS:toluene, 1:3 (w/w) thickness (blue, diamond) for 2 min. spinning time..... 45

Figure 4.12. Capacitance change recorded using the semiconductor parameter analyzer for DI water at different PDMS passivation layer thicknesses. 47

Figure 4.13. Solution dependent capacitance signal amplitudes obtained from Figure 4.7. Error bars denote one standard deviation across 50 droplet peaks. Coplanar electrodes that have width of 200 μm and gap of 50 μm were used. The electrodes were passivated with 360 nm SiO_2. 48

Figure 4.14. Calibration plot obtained by pre-mixed solutions. Error bars denote one standard deviation across 50 droplet peaks..... 49

Figure 4.15. Capacitance change recorded using the semiconductor parameter analyzer. 50 μl droplets were precisely pipetted onto the 375 nm SiO_2 passivated electrodes using the pre-mixed DI water ethanol solutions..... 51

Figure 4.16. (Top image) Each peak corresponds to a single cell flowing past to electrodes. (Bottom image) Distribution of cell capacitance from 2 DNA phase (G_0/G_1) to 4 DNA phase (G_2/M). Reprinted (adapted) with permission

from ref. [39] (Copyright 2000 Proceedings of the National Academy of Sciences)..... 52

Figure 5.1. Microscope image of DEP device designed by Ahn *et al*. a) The dark gray areas are ITO electrodes. The lower and side electrodes are for applying ground and voltage, respectively. White area represents the energized electrodes. b) Droplets flow to left channel when left electrode is energized. c) Droplets flow to right channel when right electrode is energized. Reprinted (adapted) with permission from ref. [46]. (Copyright 2006 American Physics Society)..... 56

Figure 5.2. Polarizable particle response to (A) uniform (B) non uniform electric field. Reprinted (adapted) with permission from ref. [42]. (Copyright 2006 Elsevier). 57

Figure 5. 3 a) 2D DEP electrodes that are bonded to flow focusing device with side junctions. b) 3D microscope photograph that shows microchannel bifurcation 64

Figure 5. 4. a) 2D DEP electrodes that are bonded to flow focusing device. b) 3D microscope photograph that shows microchannel bifurcation, after bifurcation channels do not expand..... 66

Figure 5. 5. Photograph of the PMMA stage. A PIC and a connector is integrated to PMMA in order to provide connection between DC to AC inverter and 2D DEP device. 67

Figure 5. 6. a) 3D DEP electrodes that are bonded to flow focusing device. b) 3D microscope photograph that shows microchannel bifurcation, after bifurcation channels do not expand. EGaIn was injected to microchannels in order to fabricate 3D DEP electrodes..... 69

Figure 5. 7. Photograph of all DEP sorters. Scale bar is 1 cm. 70

Figure 5. 8. a) 2D DEP set-up. b) Close-up view of 2D DEP device. c) CXA-M10L-L DC to AC inverter. 71

Figure 5.9. On-demand droplet sorting using 3D electrodes. When the AC signal is off, droplets go either channel. When AC signal is given to the upper electrodes, droplets are sorted towards the upper channel, vice versa. Scale bar is 500 μm. 73

Figure 5. 10. Frequency dependent real part of Clausius-Mossotti factor calculation at varying droplet conductivities. 74

Figure 6. 1. COMSOL snapshot of DEP electrodes that have 2 μm height in z direction. 82

Figure 6. 2. COMSOL snapshot of DEP electrodes that have 80 μm height in z direction. 82

Figure 6. 3. COMSOL snapshot of side electrodes. 83

Figure 6. 4. COMSOL snapshot of our electrodes. 84

Figure 6.5. T-junction microchannel bonded to 20 μm PDMS membrane. Scale bar is 1 cm. 86

Figure 6. 6. Three different on-PCB DEP electrodes. a) Design 1, b) Design 2, c) Design 3. 87

Figure 6. 7. Both microchannel types were designed for on PCB droplet sorting experiments. a) Design 1, b) Design 2 88

Figure 6.8. The portable system photograph. This system includes AD7746 capacitance-to-digital converter, DC to AC inverter, Arduino Duemilanove, droplet sensing electrodes, DEP electrodes and microchannel. Scale bar is 1 cm. 89

Figure 6.9. On-PCB droplet detection set-up. T-junction microchannels that have 300 μm width and 80 μm height was used. Scale bar is 20 cm. 90

Figure 6.10. Data point versus capacitance signal amplitude graph. The plot was taken using T-junction microchannel bonded with 20 μm PDMS membrane. After collecting data from LabView, the data was processed in MATLAB. Each peak represents a droplet in the plot. 93

Figure 6. 11. All electrode configurations in Table 6.2 are derivatives of this configuration (Design 1 for DEP electrode). 94

Figure 6. 12. All electrode configurations in Table 6.3 are derivatives of this configuration. 95

Figure 6. 13. All electrode configurations in Table 6.4 are derivatives of this configuration. 96

List of Tables

Table 3.1. Sputtering process parameters for 220 nm Cr/Cu deposition..... 14

Table 4.1. Capacitance change results (ΔC) when a DI droplet in silicone oil passes through coplanar electrodes with SiO_2 passivation layer. Both analytical model calculation results are given. The electrode length is equal to microfluidic channel width, 150 μm. The thickness of SiO_2 passivation layer (t_P) is 360 nm. Gap (2a) between electrodes is 50 μm. n is taken from 1 to 10000 while calculating Bessel function in Equation 4.3. 41

Table 4.2. Capacitance change (ΔC) results when a DI droplet in silicone oil passes through coplanar electrodes with SiO_2 passivation layer. Both analytical model calculation results are given. The electrode length is equal to microfluidic channel width, 150 μm. The thickness of PDMS passivation layer (t_P) is 10 μm. Gap (2a) between electrodes is 50 μm. n is taken from 1 to 10000 while calculating Bessel function in Equation 4.3. 41

Table 5.1. Droplet sorting efficiency with respect to droplet speed, droplet size and electrode type..... 73

Table 6. 1. Capacitance change results (ΔC) when a DI droplet in silicone oil passes through PCB electrodes. 100 μm thick glass slide is bonded to microchannels. Devices 1 to 13 are square electrodes and devices 14 to 16 are rectangular electrodes. Capacitance signal amplitudes averaged over 50 droplets for each device. 91

Table 6.2. Electric field square gradient results when different configurations of PCB DEP electrode Design 1 is used (Figure 6.11)..... 94

Table 6.3. Electric field square gradient results. In PCB DEP electrode Design 1, there are four sharp edges at voltage electrode. In all of these designs, there is only one sharp edge at voltage electrode (Figure 6.12). 95

Table 6.4. Electric field square gradient results. PCB DEP electrode Design 2 is fabricated version of Configuration 15. Electrode length (p) is 800 μm and the distance determines the voltage electrode sharpness (u) is 800 μm for all configurations. 96

Table 6.5. Electric field square gradient results calculated through a line in y direction. The distance between the tip of the voltage electrode and the line is 75 μm. The calculation was done by changing line height in z direction. Figure 6.1 & Figure 6.2 show COMSOL snapshots of these electrodes. 97

Table 6.6. Side PCB electrode and our PCB electrode comparison. Electric field square gradient results calculated through a line that lies in y direction. The distance between the tip of the voltage electrode and the line is 75 μm. The calculation was done by changing line height in z direction. The height of electrodes is 60 μm. Figure 6.3 & Figure 6.4 show COMSOL snapshots of these electrodes. 99

Table 6.7. DEP force comparison at different y and z for 60 μm height side PCB electrodes (Figure 6.3). Electric field square gradient results calculated through a line that lies in y direction. The distance between the tip of the voltage electrode and the line was varied as 65 μm, 75 μm and 500 μm. 99

Chapter 1

Introduction

1.1 Motivation of the Thesis

During the last decades, microfluidic systems became a widespread research area and gave birth to easy-to-use and miniaturized platforms that can be applied to biological and chemical analysis. Microfluidic systems or lab-on-a-chip technologies are of particular interest in this domain owing to the ability of generating, manipulating and processing of small liquid volumes. Due to their miniaturized nature, microfluidic systems especially microdroplet based microfluidic systems provide several advantages such as, enhanced analytical performance with respect to macroscale techniques, low cost and ability to process large libraries of samples in a short amount of time (high-throughput). Nowadays, these platforms are used for deoxyribonucleic acid (DNA) sequencing, chemical and biochemical screening, polymerase chain reaction (PCR), protein crystallization, directed evolution of proteins, detection of rare diseases, cell-cell interactions, single cell analysis etc.

For most of the microdroplet-based systems, one of the fundamental requirements is detection of droplets. Droplet detection has been generally done using optical detection techniques in the literature. Although these systems can detect droplets on the order of kiloHertz (kHz), they are costly and bulky. Also, labeling is needed for detection. On the other hand, electrical sensing provides scalable and label-free alternative for droplet detection, that

allows multiple sensors in a small footprint at low cost. Capacitive detection of droplets is a label-free, non-contact detection method. Previously, several groups have demonstrated capacitive sensing [1]–[3]. However, these studies lack the sensitivity that is required for droplet content detection. For this purpose, a droplet content detection system that is scalable, portable and low cost is proposed, designed and fabricated.

Besides droplet content detection, droplet sorting is needed for separating desired material laden microdroplets for further experimentation in microfluidic devices. Dielectrophoresis (DEP) is a commonly used technique for this purpose. Here, DEP systems are investigated using two dimensional (2D) coplanar and three dimensional (3D) eutectic gallium indium (EGaIn) DEP electrodes.

Both droplet content detection and sorting has been accomplished by integrating low cost and portable electronic components with microfluidic devices that have microfabricated electrodes. The fabrication of these conventional electrodes requires costly and time consuming clean room process. In order to decrease the signal to noise ratio and compactness of the system, the use of printed circuit board (PCB) as reusable electrodes has been demonstrated in this thesis. Although dielectrophoretic droplet sorting has been done using various systems, it has never been demonstrated on a printed circuit board. It is shown that PCB based detection and sorting systems would offer portability and scalability when integrated circuits and on PCB electrodes are used.

The finalized integrated system is composed of electrical detection and sorting units that have been completely implemented on a custom designed printed circuit board. The electrodes required for both sensing and actuation of droplets are fabricated using copper traces on printed circuit boards. Placing the microchannels reversibly over the electrodes finalizes the system.

An additional benefit of this approach is that the microchannels can be easily replaced while the base platform can be reused for various experiments that can be designed using microdroplets. This integrated system can be reprogrammed for the desired manipulation of droplets. Therefore, this approach provides a versatile microfluidic system.

It is believed that, using off-the-shelf and low cost electrical components can take microdroplet-based microfluidic systems one step further, and turn them into programmable, easy-to-use platforms.

1.2 Overview of Thesis

The thesis continues by reviewing existing microfluidic systems in the literature. In Chapter 3, fabrication and characterization methods are presented. Equipment operation principles are briefly explained. Following Chapter 3, highly sensitive capacitive droplet content detection system is introduced and experimental results are given. In Chapter 5, dielectrophoretic sorting of droplets are presented using 2D coplanar and 3D EGaIn electrodes. On PCB droplet detection is demonstrated and COMSOL simulations are done for finding optimum on PCB DEP electrodes in Chapter 6. The final chapter summarizes the thesis and gives some future outlook.

Chapter 2

Scientific Background

2.1 What is microfluidics ?

Microfluidics is the key science and technology that enables fluid manipulation and control in channels that have dimensions on the order of micrometers. The change in fluid physics in microscale ensures novel usages of microfluidic systems. Although the first microfluidic device was a gas chromatograph invented in 1975, these systems were not used for biological or chemical applications since 1990s [4]. Microfluidic device fabrication technology was derived from microelectromechanical system (MEMS) technology. During the last decades, microfluidic systems became a widespread research area and gave birth to easy-to-use and miniaturized platforms that can be applied to the biological and chemical analysis.

Microfluidics can be divided into three groups as continuous microfluidics, discrete (multi-phase flow or droplet-based) microfluidics and digital microfluidics. Continuous microfluidics is based on continuous liquid flow manipulation. These systems are usually used for simple and well-defined functions such as chemical separation and biochemical applications. Since the surface property of the entire system affects fluid flow at any location in the system, these systems are not suitable for integration and scalability. Discrete microfluidics compartmentalizes and manipulates small volumes of liquid with

two immiscible phases. Microdroplets are suitable for very small amount of liquid handling. Since droplet is isolated from its surrounding, any material inside droplet (reagent, cell, protein etc.) is preserved throughout the system. Droplet loading, mixing, sorting, merging, break-up enables high-throughput chemical and biological experimentation due to kHz level droplet generation. Both continuous and discrete microfluidics operates in microchannels. However, digital microfluidics is manipulation of small liquid volumes on open structures using electrowetting method. Electrowetting is changing surface properties of a material by applying electric field. On independently addressed electrodes, small volume of liquids is moved one electrode to another. These systems enable merging of different material loaded droplets. Electrowetting-on-dielectric (EWOD) is common method in digital microfluidics.

Paper-based microfluidic systems are considered as Microfluidics 2.0 by some researchers. This method is inexpensive and easy-to-use. Changing hydrophobicity of the paper at different zones using a printer and wax, channels are fabricated [5]. Printing reagents and other materials to the test zones makes microfluidic paper-based analytical devices (μPADs) cheaper point-of-care-diagnostic devices. Being user-friendly and cheap, paper-based microfluidic systems are developed for disease diagnostics in third world countries [6].

Glass, Si and polymers are three main materials for fabricating microchannels. According to application, any of these three materials can be used. Si wafer is not a suitable material for optical measurement techniques due to its opacity. Glass is a fragile material and etching of it rather difficult than etching a Si wafer. The bonding process requires high voltages or temperatures. Also, a clean-room was needed for the fabrication process [7]. Dimensions of polymers change when they interact with some chemicals such as alcohols. Silicon can be used for applications requiring high temperatures such as quantum dot synthesis [8]. Glass microchannels are resistant to chemicals and reusable. A polymer type, polymethylmethacrylate (PMMA), is suitable for high volume production

of cartridges. On the other hand, polydimethylsiloxane (PDMS), is the "working horse" of scientists, since it is non-toxic, opaque material and can be cured at low temperatures. PDMS is a rather cheap material and fabrication of a microfluidic device becomes quite easy with soft lithography techniques.

Microfluidic systems are integrated with different components in order to operate properly. Pumps, valves, mixers, pressure and flow sensors are some of the fluidic components that are used.

2.2 Droplet-based microfluidic systems

Microfluidic systems or lab-on-a-chip technologies generate, manipulate and process small liquid volumes. Due to their miniaturized nature, microfluidic systems especially microdroplet based microfluidic systems provide several advantages such as, enhanced analytical performance with respect to macroscale techniques, low cost and ability to process large libraries of samples in a short amount of time (high-throughput). Nowadays, these platforms are used for DNA sequencing, chemical and biochemical screening, PCR (polymerase chain reaction), protein crystallization, directed evolution of proteins, detection of rare diseases, cell-cell interactions, single cell analysis [9]–[15].

In this section, droplet formation, break-up and merging will be explained and examples from the literature will be given.

2.2.1 Droplet formation

In the literature, there are two main passive droplet formation generators, T-junction and flow-focusing device. Two immiscible fluids are driven from two

separate channels and meet a junction that is determined by specific geometry of the channels.

In 2001, Thorsen *et al.* published an article titled "Dynamic pattern formation in a Vesicle-Generating Microfluidic Device" [16]. For the first time, they accomplished droplet generation with two immiscible fluids using a T-junction. Both water and oil were continuously driven to the microchannel. The water obstructs the main channel at the junction, while oil flows through the channel. At this moment, high shear forces occur. The flow is not linear and static due to interactions between the boundary of two liquids. This instability arises from the competition between surface tension and shear forces. The competition generates droplets. The size and speed of droplets are finely tuned by adjusting water and oil flow rates or pressures.

Anna *et al.* used flow-focusing technique in a planar microchannel two form droplets [17]. In this technique, two immiscible phases are driven to the one orifice, where the outer channel carries oil and the inner channel carries water. These three channels form a cross at the intersection. The oil comes from two sides of the water and applies pressure to it so that water breaks into droplets. Using this technique, varying size of droplets can be generated at very high speeds.

Three regimes occur during droplet formation depending on physical properties of fluids and external variables. These regimes are categorized as squeezing, dripping and jetting [18]. The physical properties of liquids such as interfacial tensions, viscosities, and external variables as flow rates of fluids, channel dimensions and geometry are used to categorize droplet formations [19]. The dimensionless numbers originated from aforementioned variables determine these regimes. Capillary (Ca) number is the most important dimensionless number for droplet formation and its value varies between 10^{-3} and 10 (Equation 3.1).

$$Ca = \frac{\mu * V}{\gamma} \tag{3.1}$$

In Equation 3.1, μ is the dynamic viscosity of the fluid, V is velocity of the fluid and γ is interfacial tension between two liquids. Capillary number relates viscous forces with interfacial tension. Abate *et al.* stated that monodisperse droplets are generated at low capillary numbers for T-junctions and at high capillary numbers for flow-focusing devices [19].

In a T-junction two regimes occur : squeezing and dripping. When dispersed phase (water) completely blocks the main stream channel and there is pressure drop along the droplet due to channel blockage, the regime is called squeezing regime. In dripping regime, droplets do not completely block the main channel and are smaller than the dimension of the main channel. In a flow-focusing device dripping and jetting are two regimes that occur during droplet formation. In dripping regime, the dispersed phase breaks at the moment it enters the junction and turns into droplets. These droplets are immediately carried away by continuous phase. In jetting regime, dispersed phase goes into continuous phase and for a while they co-exist in the main channel [18].

Zeng *et al*. presents actively controlled droplet formation [20]. In this study, they precisely control droplet formation using a pneumatic PDMS microvalve. This valve controls droplet formation time and size. Abate *et al.* presents another droplet formation mechanism where they used air bubbles for pinching dispersed phase [21].

2.2.3 Droplet Break-up

Droplet break-up provides precisely size controlled daughter droplets from larger droplets. Link *et al.* demonstrates droplet break up by adjusting microchannel geometry [22]. Passive T-junction and obstacles in the channel are used for studying break-up dynamics. When a droplet flow into a T-junction it breaks itself into two equal sized droplets independent from initial droplet length ratio to the channel width. A T-junction always causes long droplets to break for any flow rate. If a droplet is too small and slowly goes to the junction, it will not break but directs one of the channels. At the bifurcation, droplets break inversely proportional to channel resistances. The channel with higher resistance gets the small portion of the droplet. By making a T-junction tree, it is possible to break larger droplets into 2^n daughter droplets, where n is the bifurcation number. Placing a square obstacle in the main channel breaks droplets into varying sizes depending on the obstacle's distance to the walls. An obstacle placed in the middle of the channel creates equal sized droplets, whereas closer side of the obstacle to the channel wall creates smaller droplets. Another study of Link *et al*. demonstrates droplet break-up in the presence of electric field [23]. Ting *et al.* studies droplet break-up due to heat. In this study, they use a heater to induce interfacial stress on droplet [24].

2.2.4 Droplet Coalescence

Coalescence of droplets is important in order to provide extended, complex chemical and biological experimentation. Since droplets are little compartments and preserved from the environment, it is not possible to merge content of two droplets in a controllable manner without modifications to the microfluidic system. Bremond *et al.* states that separation of two droplets favors coalescence [25]. In a diverging-converging channel they accomplish to merge two droplets. When two droplets goes into a diverging channel, they slow down, come closer but do not collide. They collide while first droplet is going through converging

channel. Designing an asymmetric chamber is a passive way to merge droplets. Baroud *et al.* demonstrates that merging of two droplets can be accomplished by lasing the interface of droplets and generating temperature gradient [26]. Also, droplets are prevented from advancing due to laser spot. Surface modification inside microchannel is another droplet merging method [27]. Fidalgo *et al*. graft hydrophilic polyacrylic acid on PDMS surface that contains benzophenone using photopolymerization method. Hydrophilic region traps droplets so that they merge. One of the passive droplet merging method is to use pillars where first droplet is trapped inside pillars and the second one bumps into it [28]. In this technique, droplet size is important. Applying electric field for merging of droplets is electrocoalescence. Zagnoni *et al.* demonstrates electrocoalescence with varying electrode shapes and droplet sizes [29]. When a droplet enters to the electrode region, applied electric field causes coalescence. Magnitude of electric field and interdroplet distance are two important parameters to accomplish electrocoalescence.

Chapter 3

Fabrication and Characterization Methods

Electrode, passivation layer and mold fabrication were done in class-100 clean room. For fabrication of substrates underneath microchannels, we benefited from the recipes that was optimized by UNAM clean room engineers. We utilized microchannel mold fabrication and soft lithography knowledge in the group. In this chapter, we give fabrication recipes and briefly explain characterization methods. Soft lithography technique will be introduced and explained.

3.1 Fabrication of Coplanar Electrodes and Passivation Layer

Before fabrication of the device, both microchannels and coplanar electrodes were designed in a CAD software. Microfluidic device fabrication consists of three steps: patterning of coplanar electrodes on a glass slide, coating of passivation layer onto the electrodes, fabrication of microchannels and bonding. In this section, electrode and passivation layer fabrication will be explained respectively describing photolithography, thin film metallization and dielectric coating. Afterwards, microchannel mold fabrication will be described.

3.1.1 Photolithography

Photolithography is the first step of realization of a microstructure. It is for patterning desired geometry to a substrate. In this process, UV (ultraviolet) or optical light is used to transfer the geometry on a mask to a radiation sensitive material, photoresist, that is on the substrate, i.e glass or Si (Silicone) wafer. This process enables micro and even nano sized structures i.e transistors, photodiodes, membranes, electrodes to be fabricated. There are two types of photoresists as positive and negative. In developer solution, UV radiated part and non-radiated part of positive and negative photoresist dissolves, respectively. Generally, photomasks are used for the cases where higher resolution is needed. For fabrication of photomasks, generally chrome deposited and resist coated glass substrates are used and desired structures are written on it using a mask writer or e-beam lithography. Eventhough using a photomask is good for obtaining higher resolution, transparency mask is better choice for resolutions equal or higher than 20 μm since it is cheap. Using a high DPI (dot-per-inch) printer and an acetate film, it is possible to transfer software design to this film. In our case, for fabrication of electrodes we used transparency masks and 1 mm glass slides as substrate. Photolithography recipe for fabricating coplanar electrodes is,

- Design coplanar electrodes using a CAD software.
- Use a high dpi printer to print the mask designs on an acetate film. The more dpi of the printer, the more resolution you can get. Tape this film on a 4 inch square glass to obtain your mask.
- Clean glass substrate with acetone, IPA and DI water respectively. Dry with nitrogen. Bake it on a 110 ℃ hot plate on 5 - 10 minutes. This is dehdyration bake.

- Spin coat HMDS (hexamethyldisilazane) on the glass 4000 rpm for 40 seconds. HMDS increases adhesion of photoresist to the substrate.
- On top of HMDS, spin coat AZ5214 positive photoresist at 4000 rpm for 40 seconds.
- Bake substrate for 50 seconds at 110 ℃ hot plate.
- Expose photoresist coated glass substrate to 365 nm UV light with dose of 50 mJ/cm^2 (EVG620).
- Put glass substrate into AZ400K developer : DI water (1:4 v/v) mixture for 30 seconds in order to dissolve UV radiated regions.
- Control the sharpness of developed regions using a microscope.

3.1.2 Thin film metallization

Coplanar electrodes on a 1 mm thick glass slide was fabricated using metal deposition technique. After photolithography, one of the physical vapor deposition methods (sputtering, thermal evaporator) was used to deposit metal on photoresist coated substrates. Cr/Cu pair is used to fabricate coplanar electrodes. Cr easily sticks to the glass substrate, therefore forms adhesive layer for Cu. Following metallization, lift-off is done by immersing metal coated substrates into acetone. Acetone removes photoresist, so regions without photoresist that was defined by photomask determine the structure after lift-off. In order to remove the photoresist, ultrasonic agitator can be used for short period of time.

3.1.2.1 Sputtering

Sputtering is one of the physical vapor deposition methods. Using sputtering, insulating or conductive thin films can be fabricated. For conductive coatings like in our case, DC magnetron sputtering is used (Vaksis, NanoD-4S). Sputtering chamber operates at room temperature. Substrate is rotated for

uniform film thickness. Under optimum chamber pressure, Ar gas flows into the chamber. Highly energized Ar ions physically bombard targets (coating materials, Cr and Cu consecutively) and break-off atoms from the target material under plasma. These atoms move towards the substrate and coat the substrate surface. The recipe for 220 nm Cr/Cu coplanar electrodes is given in Table 3.1.

Table 3.1. Sputtering process parameters for 220 nm Cr/Cu deposition

Parameters	**20 nm Cr coating**	**200 nm Cu coating**
DC power	150 W	150 W
Argon gas flow	70 sccm	50 sccm
Chamber pressure	8 mTorr	20 mTorr
Time	2 min	8 min

3.1.2.2. Thermal Evaporator

Thermal evaporator is another physical vapor deposition method. This deposition method relies on melting of coating materials at temperatures until 1500 ℃. Cr and Cu pellets are placed on tungsten boots. Passing through tungsten boots, after some time current leads to temperature increase on boots resulting in melting of the coating material. Depending on the material and thickness of the tungsten boot, the applied current is changed. The vapor of the melted material moves toward the substrate and coats it. The rate of evaporation is important while coating the substrate. It should be observed during the process to adjust it properly. Substrate rotation is used for uniform film thickness. In our case, first Cr then Cu is coated. Since the melting point of Cr is higher than Cu, higher current (100 A) was used for melting Cr.

3.1.3 Dielectric film coating

Dielectric film coating on coplanar electrodes is needed as passivation layer to prevent droplet pinning onto the electrodes and contamination between consecutive droplets. For droplet and droplet content sensing applications, thinner passivation layer between microchannels and coplanar electrodes enhances the capacitance signal amplitude, therefore, increases the resolution of the system.

3.1.3.1 Plasma Enhanced Chemical Vapor Deposition (PECVD)

PECVD is a method for coating dielectric films. Unlike other chemical vapor deposition techniques, PECVD operates at low temperature (200 ℃ - 400 ℃). It is a good candidate for applications where high temperature damages the device. While reactant gases flow through between ground and energized RF electrodes, capacitive coupling of electrodes initiates plasma. The resulting chemical reaction yields solid film on the substrate. The substrate is placed onto the ground electrode that is heated. For fabrication of devices, SiO_2 (silicon dioxide) is used as passivation layer between microchannels and coplanar electrodes. SiH_4 (silane) and N_2O gases were used to form plasma at 200 ℃. SiH_4 and N_2O reacts to form solid SiO_2, N_2 and H_2 gases. He gas were used to slow the reaction. Target pressure and RF power were set as 1 Torr and 10 W. Thin film thickness is adjusted by changing process time.

3.2 Fabrication of Microchannel Mold

Microchannels were fabricated by taking replica of channel mold that is on a SU-8 coated Si wafer using PDMS (polydimethlysiloxane). For fabrication of microchannel molds two types of negative photoresist , SU-8 2005 and SU-8 2050, were used by applying photolithography techniques. During this process,

transparency mask was used. SU-8 2005 and 2050 were spin coated on Si wafer respectively. Dispensing SU-8 2005 beneath SU-8 2050 prevents the stiction of PDMS on silicon wafer and enables easy removal of cured PDMS from the mold since PDMS sticks to Si, but not SU-8. Generally, instead of spinning thin SU-8 2005 beneath SU-8 2050, researchers apply silanization process before PDMS molding to make Si surface hydrophobic. At the end of the process, SU-8 developer was used for extracting the mold structure. Process flow is given in Figure 3.1. For 80 μm height mold, detailed process is given below:

- Design microchannels using a CAD software.
- Use a high dpi printer to print the mask designs on an acetate film. The Tape this film on a 4 inch square glass to obtain your mask.
- Clean the 4 inch Si wafer with acetone, IPA and DI water respectively. Dry with nitrogen. Bake the wafer on a 120 ℃ hot plate on 5 - 10 minutes. This is dehdyration bake.
- Cool it to room temperature.
- Spin coat SU-8 2005 using the following parameters :

Time	25 sec	40 sec
Speed	500 rpm	2500 rpm
Acceleration	100 rpm/s	200 rpm/s

This is a two step spinning process. The first step provides dispersion of the SU-8 to the whole surface of the Si wafer.

- After spinning SU-8 2005, bake it using a three step baking process on a hot plate. This is a gradual process to prevent film from forming cracks. This is soft baking.

65^{o}C	2 min
95^{o}C	4 min
65^{o}C	1 min

- Cool the wafer down to room temperature.
- Expose the baked Si wafer with 120 mJ /cm ^{2} UV light at 365 nm without using a mask. This is exposure.
- Bake it on hot plate using a gradual process. This is post exposure bake.

65^{o}C	1 min
95^{o}C	3 min
65^{o}C	1 min

- Cool it to room temperature.
- Spin coat SU-8 2050 using the following parameters :

Time	45 sec	35 sec
Speed	500 rpm	2000 rpm
Acceleration	50 rpm/s	300 rpm/s

- After coating process is finished, take the excess SU-8 2050 from the edges of the wafer using a glass slide. This is edge bead removal.
- Bake it on hot plate using a gradual process.

65^{o}C	4 min
95^{o}C	8 min
65^{o}C	2 min

- Cool it down to room temperature.
- Expose the baked Si wafer with 230 mJ /cm ^{2} UV light at 365 nm using acetate film taped 4 inch glass (mask).
- Bake it on hot plate using a gradual process.

65^{o}C	3 min
95^{o}C	8 min
65^{o}C	1 min

- Cool it down to room temperature.
- Pour SU-8 developer solution into a glass container. Put your wafer into the solution for 6 minutes. Depending on the freshness of the developer solution this time may decrease or increase. Therefore, observe it during the process.
- Dry it with nitrogen. Never use water in this step.
- Control the microstructures under a microscope.
- In order to prevent delamination of SU-8 layers during PDMS replica molding, apply epoxy to the edges of the wafer and kept it at room temperature overnight. After epoxy is dried, apply baby powder to the epoxy applied regions prevent stiction of PDMS.

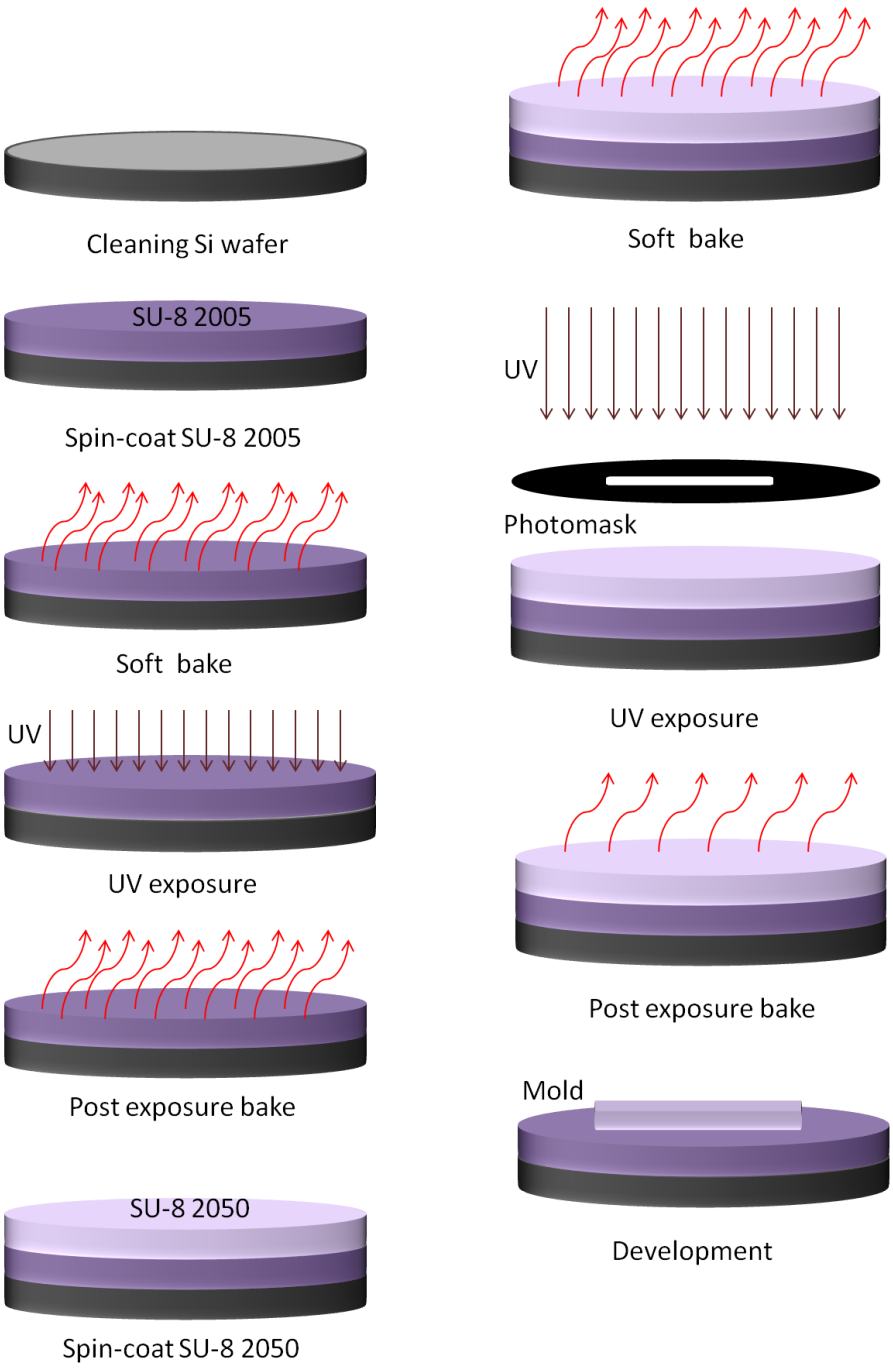

Figure 3.1. Schematic of mold fabrication using SU-8 negative photoresist

3.3 Soft Lithography

Soft lithography is a method that refers replicating mold structure using polymeric, "soft", materials by stamping. For fabrication of microchannels,

PDMS (polydimethylsiloxane) is used as soft material. Soft lithography steps are written below :

- Pour 10:1 (w/w) ratio Dow Corning Sylgard 184 silicone elastomer and silicone elastomer curing agent into a plastic cup. First pour 30 g silicone elastomer , then 3 g curing agent. Since curing agent amount is less, be careful while pouring it.
- Using a plastic spoon, mix them. Let silicone elastomer absorb curing agent. Do this with using spoon and don't daub it to the sidewalls of the cup. While mixing, a lot of air bubbles will be generated. Try to increase amount of air bubbles. Until all mixture is composed of air bubbles continue to mix.
- Remove plastic spoon. Put the mixture into a dessicator. The air inside the dessicator will be removed by pump. While the pressure inside the chamber is decreasing, the bubbles expand. When lid of the dessicator is opened, due to increasing pressure bubbles will explode. Continue this process until all the bubbles explode and the mixture become transparent. The bubbles explode when the mixture is left in a room for some time. However, this process takes too much time that while bubbles are exploding, curing occurs. It is wise to use a dessicator.
- Use VWR aluminum pans that a 4 inch wafer fit into. Raise sidewalls of the aluminum pan to prevent leakage of PDMS. Put mold into it. Dispense transparent PDMS mixture from the center of the mold at a low altitude. During this process, prevent air trapping inside PDMS. Pouring PDMS mixture from high altitude causes air trapping. After dispensing all the mixture inside the cap, using a needle pop the air bubbles in the mixture. If these bubbles are close to your channel, they will damage the structure of the channel. Also, for better view under microscope try to pop all the bubbles.
- Put aluminum pan on a 100 ℃ hot plate for 4 hrs to cure PDMS. In about 30 minutes, the PDMS becomes solid. Be sure that hot plate is flat. An uneven hot plate causes non uniform distribution of liquid

PDMS. Therefore, precision tips are not stay in inlets where the thickness of the PDMS slab is too thin.

- After 4 hours, take the solid PDMS from the hot plate. Lay stretch film on a flat surface. Be sure that stretch film is not too tight. Remove mold containing PDMS from the aluminum pan. Put upper side of the PDMS slab onto stretch film. Using a scalpel, cut excess PDMS around the mold.
- Lay another layer of stretch film on a flat surface. By putting your fingernail between PDMS and mold, try to release PDMS from the mold at the borders of the mold. After releasing the PDMS along the mold contour, using your hand release the PDMS from the mold. Put it onto stretch film.
- Using a scalpel divide the PDMS slab into separate sections that contain microchannels.
- Punch inlet and outlet using a biopsy punch. These holes provide connection between microchannel and liquids. While using biopsy punch be sure that stretch film on both sides of the inlet is slightly removed.

This PDMS slab only contains three walls of the microchannel. By bonding PDMS to glass or PDMS provides four walled microchannels. Bonding can be done using air or oxygen plasma. Plasma treatment converts naturally hydrophobic PDMS surface into hydrophilic one, so it is possible to use water inside microchannels. Therefore, after plasma treatment dangling bonds occur on the surface of both materials. When two surfaces come together, they form unbreakable bonds. This is bonding of PDMS to glass slide. For PDMS glass bonding the following recipe can be used :

- Clean glass slide using acetone, IPA and DI water.
- Dry it with nitrogen. Put it on 100 ℃ hot plate for 60 minutes.

- Put PDMS slab into a plasma cleaner (Nanoplas, DSB6000) chamber where microchannel is at upward position. Also, put glass slide into chamber.
- Apply oxygen plasma for 1 min., 30 sccm O_2 flow rate at 50 W.
- Quickly get treated surface of PDMS and glass slide together.
- Immediately after bonding, bake bonded device on 100 ℃ hot plate for 12 hours for enhancement of the bonding.

For PDMS-PDMS bonding parameters are, 30 W, 30 sec, 56 sccm O_2 flow rate.

3.4 Characterization Methods

Characteristics of fabricated devices were measured using different apparatus. After every fabrication process, i.e., fabrication of coplanar electrodes, mold, spin coating of PDMS on coplanar electrodes, characterization step was completed. Thickness of coplanar electrodes on glass slides, spin coated PDMS layer and deposited SiO_2 on coplanar electrodes, mold height were measured using Atomic Force Microscopy (AFM) (PSIA, XE-100E, Suwon) , Variable Angle Spectroscopic Ellipsometer (J.A. Woollam, V-VASE) and Stylus Profilometer (KLA Tencor, P6 Surface Profiler). During the experiments, microfluidic devices were tested using a pressure pump. In this part, characterization methods that are used during the studies will be explained briefly.

3.4.1 Atomic Force Microscopy (AFM)

Binnig, Quate and Gerber invented Atomic Force Microscope in 1986 [30]. Atomic force microscope combines properties of a surface profilometer and a scanning tunneling microscope. Unlike scanning tunneling microscope, atomic force microscope can be used on both conductive and insulating surfaces. It is a powerful microscopy technique, since it is possible to measure angstrom scale surface thickness with it. The AFM operation principle as follows: AFM

cantilever is brought close to the sample to scan the surface, so attractive force occurs between the surface and the cantilever tip. This force leads cantilever to deflect towards the sample surface. After some proximity, i.e tip contacts with the surface, the force becomes repulsive, so the cantilever tip deflects away the surface. A laser beam is reflected from the flat top of the cantilever while it is operating through a surface. This information is collected by position sensitive photodiode and turned into a surface topography image with software.

The mostly used operation modes of an AFM are contact, noncontact, and tapping mode. Contact mode is static and the other two modes are dynamic modes. The difference between tapping and noncontact mode is that, in tapping mode cantilever tip touches to the surface, but in noncontact mode cantilever tip is close to the surface throughout the measurement.

For measuring coplanar electrode thickness, AFM (PSIA, XE-100E, Suwon) is used with tapping (intermittent contact) mode in air under ambient temperature . A Tap190Al-G probe with a force constant of approximately 48 N/m and resonance frequency of 190 kHz was used.

3.4.2 Variable Angle Spectroscopic Ellipsometer

Ellipsometry is an optical technique that measures the polarization change of the reflected light beam from the surface. It is non-destructive and requires neither sample preparation nor special environment. When the incident beam reflected from the surface and the substrate beneath the surface, it experiences polarization change that is specific to structure of the surface. Using polarization change data, various information can be extracted; film thickness, refractive index (n), extinction coefficient (k), surface roughness and anisotropy of grown materials by fitting the experimental data to a theoretical model. Ellipsometry is capable of measuring film thicknesses from several angstroms to micrometers.

Thickness of the SiO_2, PDMS and toluene-thinned PDMS passivation layers were measured using an Ellipsometer (J.A. Woollam, V-VASE). Ellipsometer was used at an incidence angle of 65^o. Cauchy dispersion function was used to determine passivation layer thicknesses. The refractive indices of PDMS and toluene-thinned PDMS are the same, since toluene evaporates during and after spin coating, leaving only PDMS as a passivation layer. In that regard, toluene is only used to decrease the viscosity of the PDMS mixture before spinning, in order to decrease passivation layer thickness. In order to fit experimental data, refractive indices of PDMS and toluene-thinned PDMS were taken as 1.42, and refractive index of SiO_2 was taken as 1.55.

3.4.3 Stylus Profilometer

Profilometer is a surface thickness and roughness measurement apparatus. A diamond stylus contacts with the surface of the sample and goes along the surface for a specified distance. Depending on stylus diameter and the contact force of the stylus, it can measure various thicknesses from nanometer to millimeter. Scan rate and signal sampling rate controls horizontal resolution. The software converts analog stylus vertical position into digital data.

In order to characterize microchannel heights, molds were measured using a stylus profilometer (KLA Tencor, P6 Surface Profiler). Also, spin coated PDMS membrane thicknesses for on PCB droplet detection and sorting experiments were measured.

Chapter 4

Droplet content detection using integrated capacitive sensors

This chapter is based in part on the publication “Microfluidic droplet content detection using integrated capacitive sensors,” **P. K. Isgor**, M. Marcali, M. Keser, and C. Elbuken, Sensors and Actuators B : Chemical, (2015).

4.1 Introduction

Detecting analytical content of droplets is one of the fundamental requirements for most of the microdroplet based systems. Electrical droplet sensing provides a scalable and label free alternative for the more prevalent optical detection techniques, which allows multiple sensors in a small footprint at very low cost. Although, optical systems can detect droplets at very high rates (on the order of kHz), these systems are not scalable [31]. Microfluidic capacitive sensors have been used for detection of droplets, however they have been lacking the sensitivity required for detecting the content of droplets. The previous studies that utilize off-the-shelf electronic components fall short in providing the sensitivity that is required for droplet content detection [32], [2] . For instance, Demori *et al.* have reported capacitive detection of liquids due to different dielectric properties. They have used a custom-made electronic circuitry for

liquid detection and reported the resolution of their system as 0.06 fF. However, the resolution of the system is a function of sensor geometry, which determines the absolute value of the capacitance value measured. A better metric for this study is the resolution in terms of the dielectric constant unit. When the study is analyzed in depth, their dielectric constant resolution is found 5.5 dielectric units. Moreover, these measurements were performed in a continuous flow regime. Thus, there is need for off-the-shelf detection systems that provide high sensitivity for droplet content detection. In order to fill this gap, we demonstrated capacitive droplet content detection using commercially available sensors.

We developed a scalable, portable, and highly sensitive capacitive microdroplet content detection system using coplanar electrodes with nanometer thick silicon dioxide (SiO_2) passivation layer and commercially available, low-cost capacitive sensors and a microprocessor. For this purpose, we designed a Y-junction microfluidic device that allows modification of droplet content by mixing ethanol and distilled (DI) water at any ratio. When a droplet enters the sensing region where coplanar electrodes are placed, the change in dielectric permittivity leads to the change in capacitive signal. Moreover, changing droplet content changes capacitive signal amplitude. We characterized the system by modifying the dielectric content of the droplets on the run and measuring the corresponding capacitance signal. We calculated the system resolution as 3 dielectric permittivity units. We verified the results using a semiconductor parameter analyzer. We enhanced the signal by minimizing the thickness of the passivation layer. The application specific integrated circuit used in this work enables a portable, low-cost detection system and matches the performance of bench-top analyzers. To the best of our knowledge, we achieved the most sensitive capacitive detection signal in the literature. This system can be used for very precise droplet size and speed detection as well as droplet counting.

We believe that using off-the-shelf and low cost electrical components for high sensitivity droplet content can take microdroplet-based microfluidic systems one step further, and turn them into programmable and easy-to-use platforms. This study takes a step in that direction by utilizing very low cost electronics (in total $24) for high sensitivity droplet content measurement.

4.2 Capacitive detection theory

In a droplet based microfluidic system that includes coplanar electrodes beneath microchannel, DI water droplets in silicone oil lead to capacitance value change when droplets enter sensing region due to stark contrast between dielectric permittivity of silicone oil ($\mathcal{E}_r$ = 2.5) and water ($\mathcal{E}_{r\_water}$ = 80). In order to calculate the capacitance formed by coplanar electrodes under changing medium, there are two theoretical models in the literature. Chen *et al*. calculated capacitance using conformal mapping with an inverse-cosine transform, and Otter used Fourier series approximation of surface potential [33], [34]. In this part, these two models will be briefly explained. The models are used for calculating capacitance change value for a DI droplet in silicone oil.

Chen *et al*. have computed capacitance of parallel coplanar electrodes. They studied a system which has a single dielectric layer on top of planar electrodes, as shown in Figure 4.1 [33]. An electrical potential difference was applied to the electrodes and electric field distribution was solved using conformal mapping techniques. The authors concluded with the following formula (Equation 4.1) for the calculation of capacitance formed by fringing fields

$$C = \frac{2.\varepsilon_r.\varepsilon_0.L}{\pi} \ln\left[1 + \frac{w}{a}\sqrt{\left(1 + \frac{w}{a}\right)^2 - 1}\right] \quad (4.1)$$

where w is the width of the electrode, L is the overlapping length of the electrodes ($L \gg w$), a is the half gap between the electrodes, ε_r is the

permittivity of the dielectric layer and ε_o is the dielectric permittivity of the vacuum. This equation gives very good results for electrode designs satisfying $w/a \gg 1$ and close approximation for $w \sim a$ [33].

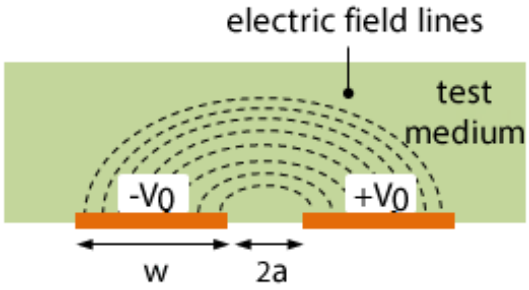

Figure 4.1. Schematic of the system studied by Chen *et al*. [33]

Another analytical model was suggested by Otter, where approximate surface potential was used in order to simplify Engan's equation [34], [35]. For an interdigitated electrode, as shown in Figure 4.2, an approximate capacitance expression was computed [34]. In this model, the potential around the electrode was described using Fourier series, since interdigitated electrodes have a periodicity and fringing fields at the electrode periphery was neglected. The capacitance of the interdigitated electrode was found as

$$C = \frac{4.p.q.\varepsilon_r.\varepsilon_0}{\pi.a} \sum_{n=1}^{\infty} \frac{1}{2n-1} J_0^2 \left(\frac{(2n-1).\pi.s}{2a}\right) \qquad (4.2)$$

where p is the length of the overlap of the electrodes, q is the total width of the interdigitated electrode, s is the gap between electrodes, $a=s+w$ is the periodicity and J_0 is the zeroth order Bessel function. In this model, the thickness of the electrodes was neglected as compared to the system's other dimensions and number of electrodes was assumed to be large. Moreover, the width and gap between electrodes were taken as uniform. Also, p was assumed to be much larger than w and s.

As seen from Equation 4.1 and Equation 4.2, the two models for the calculation of capacitance by coplanar electrodes look quite different. For the ease of comparison, it is wise to use the same notation for these two models. Therefore, Equation 4.2 was rewritten by using variables consistent with Equation 4.1 as

$$C = \frac{4.L.N.\varepsilon_r.\varepsilon_0}{\pi} \sum_{n=1}^{\infty} \frac{1}{2n-1} J_0^2 \left(\frac{(2n-1).\pi.2a}{2(2a+w)} \right) \quad (4.3)$$

where a is the half gap between electrodes, w is the width of the electrodes, L is the overlapping electrode length, N is the number of electrodes which was found by dividing q by a.

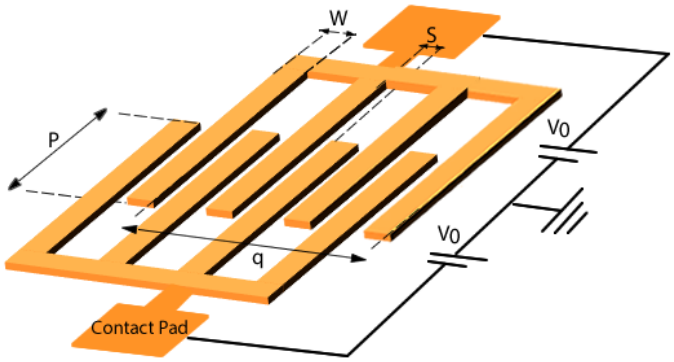

Figure 4.2. Schematic of the system studied by Otter [34].

Electrode width and gap determines the penetration depth of electric field lines. Some of field lines go through the PDMS bulk as shown in Figure 4.3.a. Owing to lower dielectric permittivity than the channel, the contribution of bulk PDMS to the capacitance signal is negligible. Therefore, only a portion, effective width, of the electrode is responsible for the signal detected by the sensor [33]. Using FEM simulations, Sun *et al*. have shown that for a fixed channel height and electrode gap, increasing electrode width does not excessively change electric field magnitude [36]. As a result, the capacitance formed by (w-w_{eff}) part of the electrodes was neglected while calculating capacitance.

For a droplet based microfluidic system that includes capacitive sensing using coplanar electrodes, a passivation layer should be used between the electrodes and material under test to prevent pinning of the droplets onto electrodes and cross contamination. Therefore, total capacitance is calculated by taking into account of passivation layer capacitance.

In order to compare two analytical models, we calculated capacitance that is generated by coplanar electrodes passivated by either 10 μm PDMS or 360 nm SiO_2. The material change is from DI water to silicone oil in a microchannel. The electrode dimensions are given in Section 4.5.1. As it can be seen from Figure 4.3, the total capacitance is formed through passivation layer and the microchannel. We denoted capacitance over the channel and capacitance through the passivation layer as C_{ch} and C_p, respectively. C_{ch} is calculated using both Equation 4.1 and Equation 4.3. The total capacitance, C_T, is calculated using the following formula

$$\frac{1}{C_T} = \frac{2}{C_P} + \frac{1}{C_{ch}} \tag{4.4}$$

Total capacitance is written as

$$C_T = \frac{C_{ch}.C_P}{2.C_{ch} + C_P} \tag{4.5}$$

The change in total capacitance due to a material property change on electrodes is written as

$$\Delta C_T = \frac{(\Delta C_{ch}).C_P}{2.(\Delta C_{ch}) + C_P} = \frac{\Delta C_{ch}}{2.\left(\frac{\Delta C_{ch}}{C_P}\right)+1} \tag{4.6}$$

In this equation, passivation layer capacitance, C_p, is calculated as follows

$$C_P = \frac{\varepsilon_r . \varepsilon_0 . A}{t_P} \tag{4.7}$$

where A is the multiplication of channel width by electrode width, and t_P is the thickness of the passivation layer.

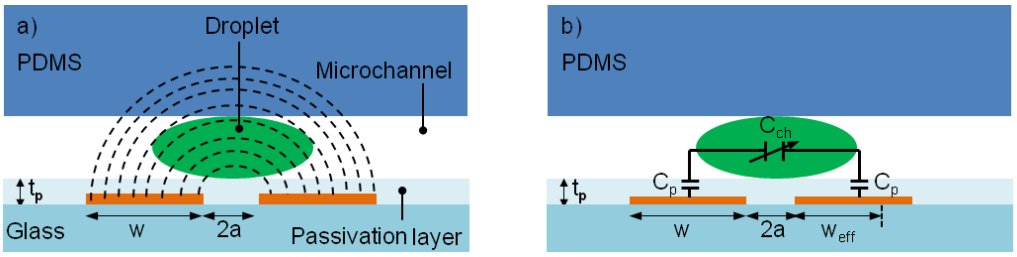

Figure 4.3. Illustration of the capacitance formed by coplanar electrodes. a) Field lines through the passivation layer, microchannel and PDMS bulk. b) Capacitances through passivation layer (C_p) and microchannel (C_{ch}). Dielectric permittivities of materials are; $\varepsilon_{r\_water} = 80$, $\varepsilon_{r\_oil} = 2.5$, $\varepsilon_{r\_PDMS} = 2.5$, $\varepsilon_{r\_SiO2} = 3.85$. Effective width of the electrodes is shown as w_{eff}.

Therefore, the total capacitance change from silicone oil to DI water droplet is

$$\Delta C = \frac{C_{water}}{\left(2.\left(\frac{C_{water}}{C_P}\right)+1\right)} - \frac{C_{oil}}{\left(2.\left(\frac{C_{oil}}{C_P}\right)+1\right)} \tag{4.8}$$

C_{water} and C_{oil} were calculated using both Equation 4.1 and Equation 4.3. While using Equation 4.3, n parameter in Bessel function is taken from 1 to 10000. C_p was calculated using Equation 4.7. Then, these values were plugged into Equation 4.8 in order to estimate capacitance change (ΔC). Dielectric permittivity of the vacuum was taken as $8.85x10^{-12}$ F/m.

4.3 Design and Fabrication of the Microfluidic Device

4.3.1 Design of the Device

For droplet content detection studies, we used a microfluidic device schematically shown in Figure 4.4. To form droplets a T-junction was designed. Also, a Y-junction was designed to drive two different aqueous phases [16], [37]. Y-junction ensures droplet content modification on the run. After droplet generation section, mixing and detection region were placed, respectively. A photograph of the fabricated device is shown in Figure 4.5.

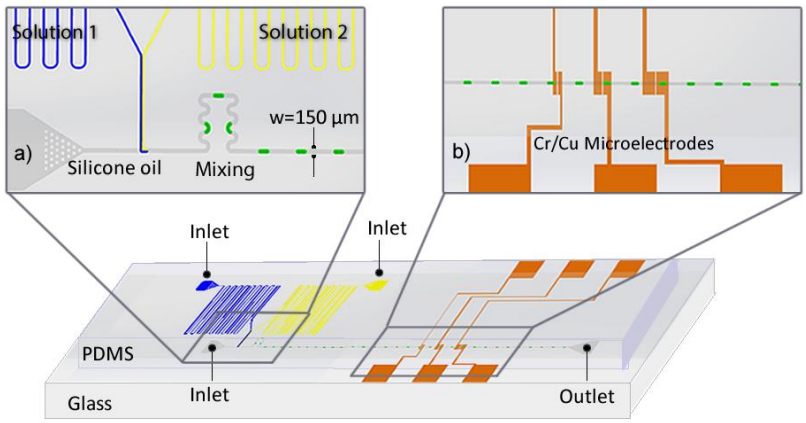

Figure 4.4. Schematic of the microfluidic device. The insets show the (a) droplet generation region and mixing region, (b) detection region.

A mixing region was designed to passively mix two aqueous phases i.e., ethanol and DI water to get homogeneous droplets. Coplanar electrodes were designed to detect droplet content. Electrode width and gap were determined as 200 µm and 50 µm using the aforementioned analytical models.

4.3.2 Fabrication of the device

Microfluidic device fabrication consists of three steps: patterning of coplanar electrodes on a glass slide, coating of passivation layer onto the electrodes, fabrication of microchannels and bonding. After photolithography step, 20 nm Cr and 200 nm Cu were deposited onto glass slides using magnetron sputtering. Electrode thickness was measured with an AFM.

In order to prevent cross-contamination between droplets and pinning of droplets onto the electrodes, coplanar electrodes should be passivated. It can be seen from the analytical formula (Equation 4.8) that increasing passivation layer thickness decreases the capacitance signal amplitude. Therefore, our primary concern was to passivate electrodes with a pin-hole free, thin coating while finding most suitable passivation layer type. It is known that for passivation of electrodes, there are two fabrication options, spin-coating and thin film deposition. Bare glass slides were coated with either spin coating of PDMS, toluene-thinned PDMS or thin film deposition of SiO_2. For studying the effect of spin speed on the thickness of the coated layer, the PDMS mixture was spun on microscope slides for 5 minutes at spin rates varying from 1000 rpm to 7000 rpm. In order to get the toluene thinned PDMS, PDMS mixture was mixed with toluene in 1:3 (w/w) ratio. Then, the prepared mixture was spun coated on microscope slides for 2 minutes at same spin rates. After spin coating, glass slides were baked at 110 ℃ for 2 hours. SiO_2 was deposited using a PECVD. Thickness of the SiO_2, PDMS and toluene-thinned PDMS passivation layers were measured using a Variable Angle Spectroscopic Ellipsometer. Variation of passivation layer thickness with respect to spin rate is discussed in Section 4.5.4.

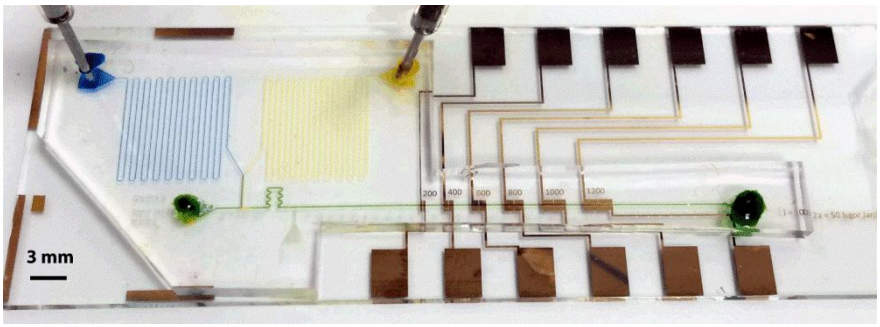

Figure 4.5. Photograph of the fabricated microfluidic device. Channels were filled with dye solutions for clarity.

Coplanar electrodes were passivated either by spin coating of polydimethylsiloxane (PDMS) or plasma enhanced chemical vapor deposition of SiO_2. We have studied both methods to enhance the capacitance signal.

The microchannels were fabricated using standard soft lithography methods [38]. The channel height was measured as 100 μm using Stylus Profilometer. Microchannels were bonded to the glass slides with passivated coplanar electrodes using oxygen plasma. The devices were baked at 100 ^{o}C for 12 hours immediately after plasma activated bonding to enhance the bonding.

4.4 Experimental Procedure

4.4.1 Experimental Set-up

Experiments were done using a microfluidic device shown in Figure 4.5. Liquids were driven to the channels with a pressure pump (Elveflow). Silicone oil with 50 mPa s viscosity was chosen as continuous phase. Droplets were formed at varying ethanol and DI water concentrations. We experimentally verified mixing with colored DI water using yellow and blue dyes as shown in Figure 4.6.

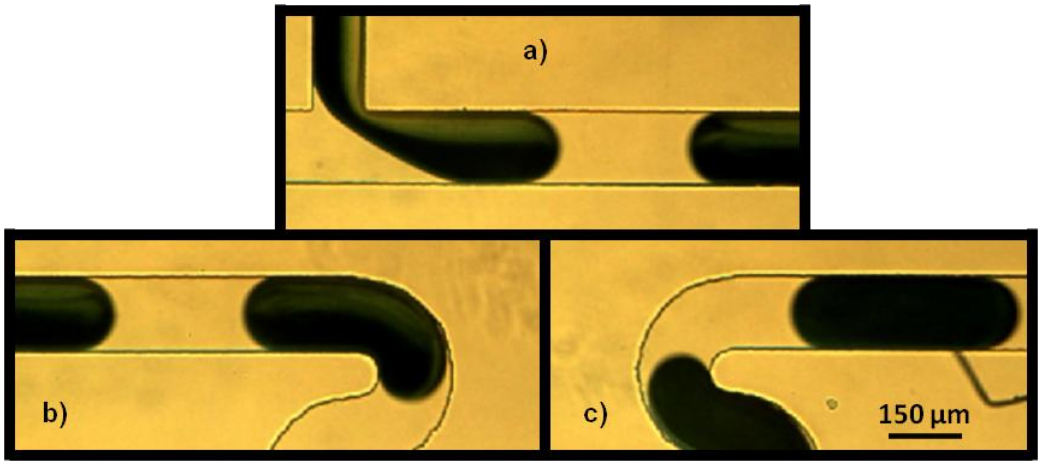

Figure 4.6. a) Images of the droplet formation and their travel along the serpentine section in our system. b) Droplets before the mixing region. c) Droplets after mixing region, completely mixed.

Due to stark contrast between dielectric permittivity of silicone oil ($\mathcal{E}_r$ = 2.5) and microdroplet ($\mathcal{E}_{r\_ethanol}$ = 24 < $\mathcal{E}_r$ < $\mathcal{E}_{r\_water}$ = 80), capacitance signal amplitude changes when a droplet enters the sensing region. The signal was measured using a capacitive-to-digital converter integrated circuit (Analog Devices, AD7746). Unlike bench-top analyzers such as LCR, AD7746 is a low-cost and portable apparatus. Also, it can easily be integrated to a microfluidic system. Capacitance measurement range of AD7746 is ±4 pF with a precision of 4 fF. It uses an excitation signal at a constant frequency of 32 kHz during the measurement. The read-out data rate was kept constant at 50 Hz to have enough sampling rate and low background noise. Internal offset capacitor was tuned for self-calibration during the test start-up cycle to prevent imprecision of the signal. During this study, single-ended mode was used. AD7746 was communicated with LabView using a USB-powered microcontroller (Arduino Duemilanove ATmega328). This microcontroller was used for displaying real-time capacitance signal through a LabView interface.

During the experiments, droplets were observed using an inverted compound microscope (Omano OMFL600) to maintain the droplet sizes similar.

4.4.2 Experimental Procedure

Before droplet content measurement experiments, AD7746 characteristics and increasing electrode width effect on capacitance signal were studied. For both of the experiments the same device was used and capacitance change of DI droplets of same size and speed were detected. The coplanar electrodes were passivated by 375 nm thick SiO_2. The real-time capacitance signal amplitude was recorded and signal level for each droplet was measured from the recorded data. The characterization of AD7746 was done using 200 μm width 50 μm gap electrodes at different data read-out rates; 10 Hz, 50 Hz, 90 Hz. Increasing electrode width effect on capacitance signal was studied using coplanar electrodes that have a width of 200 μm, 400 μm and 600 μm and a gap of 50 μm.

For droplet content detection, coplanar electrodes that have a width of 200 μm and a gap of 50 μm were used. These electrodes were passivated by 360 nm SiO_2 dielectric layer. In order to change the dielectric content of the droplets, ethanol and blue colored DI water were separately driven from aqueous solution inlets. The streamline that separates colored DI water and ethanol was observed to form the aqueous droplets of predetermined concentrations. Experiments were done at five different concentrations of ethanol DI water mixtures (0%, 25%, 50%, 75%, 100% (v/v) ethanol concentration). For each concentration, snapshot images were captured both at the Y-junction and detection region as shown in Figure 4.7. Plug-like droplets of similar size and speed were generated by tuning flow rates. The length of droplets was larger than the gap between electrodes to completely occupy the sensing domain. When droplet enters to the detection region, the real-time capacitance signal amplitude was displayed through the LabView interface and recorded.

In order to verify the results and determine the resolution of the system, seven different solutions of ethanol and DI water mixtures were prepared with ethanol concentrations of 0%, 5%, 10%, 25%, 50%, 75% and 100% (v/v) in vials. These mixtures were used as dispersed phase and droplets of these solutions were generated separately. Capacitive droplet content measurements were done as explained above. These results form the calibration plot which shows dependence of capacitance signal amplitude on ethanol concentration as shown in Figure 4.14.

Capacitance signal amplitude was recorded using a bench-top semiconductor parameter analyzer (SPA) (Keithley 4200) and a probe station (Figure 4.8.e) to verify this calibration plot. Coplanar electrodes that have 200 μm width and 50 μm gap were passivated with 375 nm SiO_2 layer. 50 μL of same pre-mixed solutions were dispensed onto coplanar electrodes using a micropipette. The dispensed volume was high enough to completely fill the sensing domain. Between different runs, the glass slide was washed thoroughly and dried with nitrogen.

The effect of passivation layer thickness on capacitance signal amplitude was studied by additional spin coating of PDMS on coplanar electrodes after each measurement. 50 μL of DI water was dispensed onto the electrodes have 200 μm width and 50 μm gap. 50 μl of DI water was pipetted onto these electrodes while measuring the capacitance change using a semiconductor parameter analyzer.

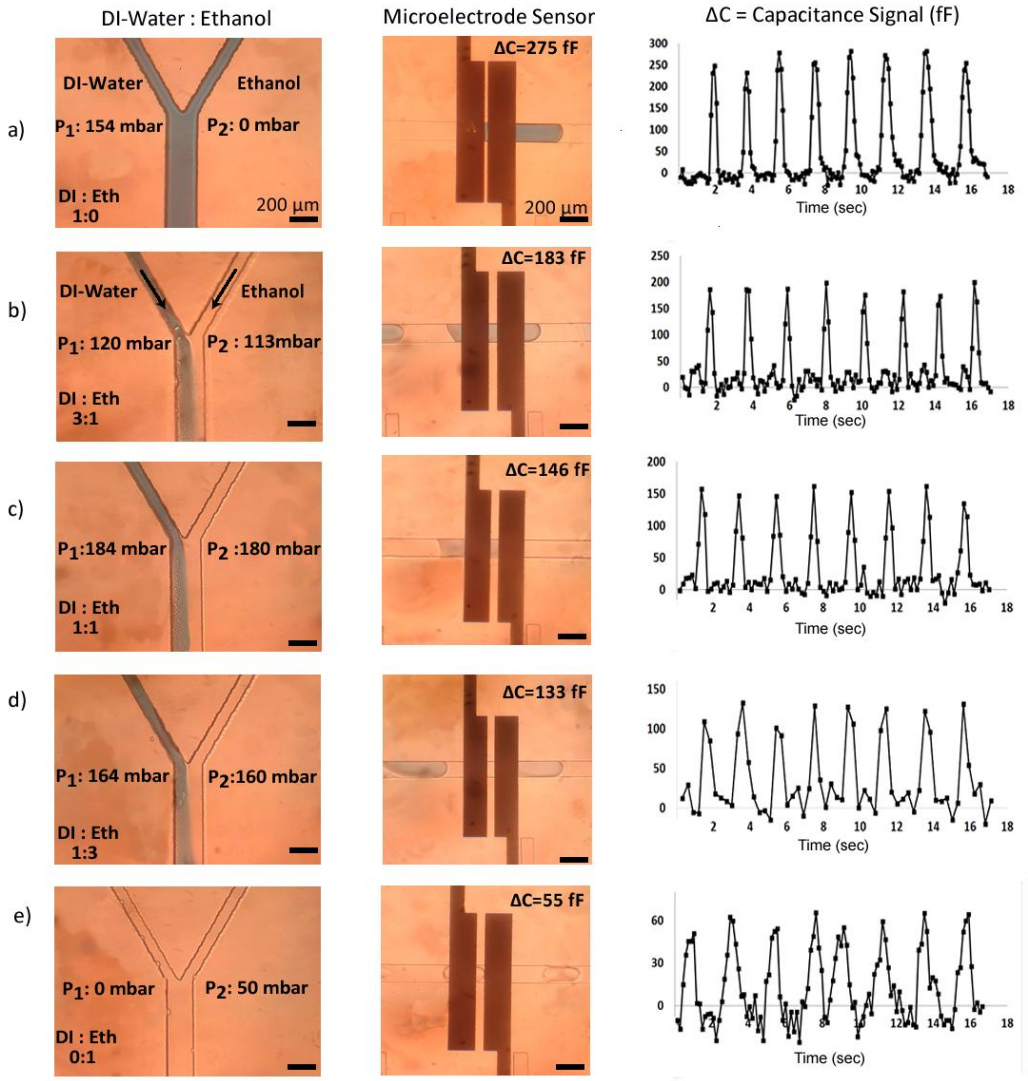

Figure 4.7. Capacitance signal for varied DI ethanol mixtures (a) only DI, (b) 25% ethanol, (c) 50% ethanol, (d) 75% ethanol, (e) only ethanol. The real-time capacitance signal amplitude was displayed through the LabView interface and recorded when droplet enters to the detection region. Each peak corresponds to a single droplet in the sensing region. The plots show the data for 17 seconds.

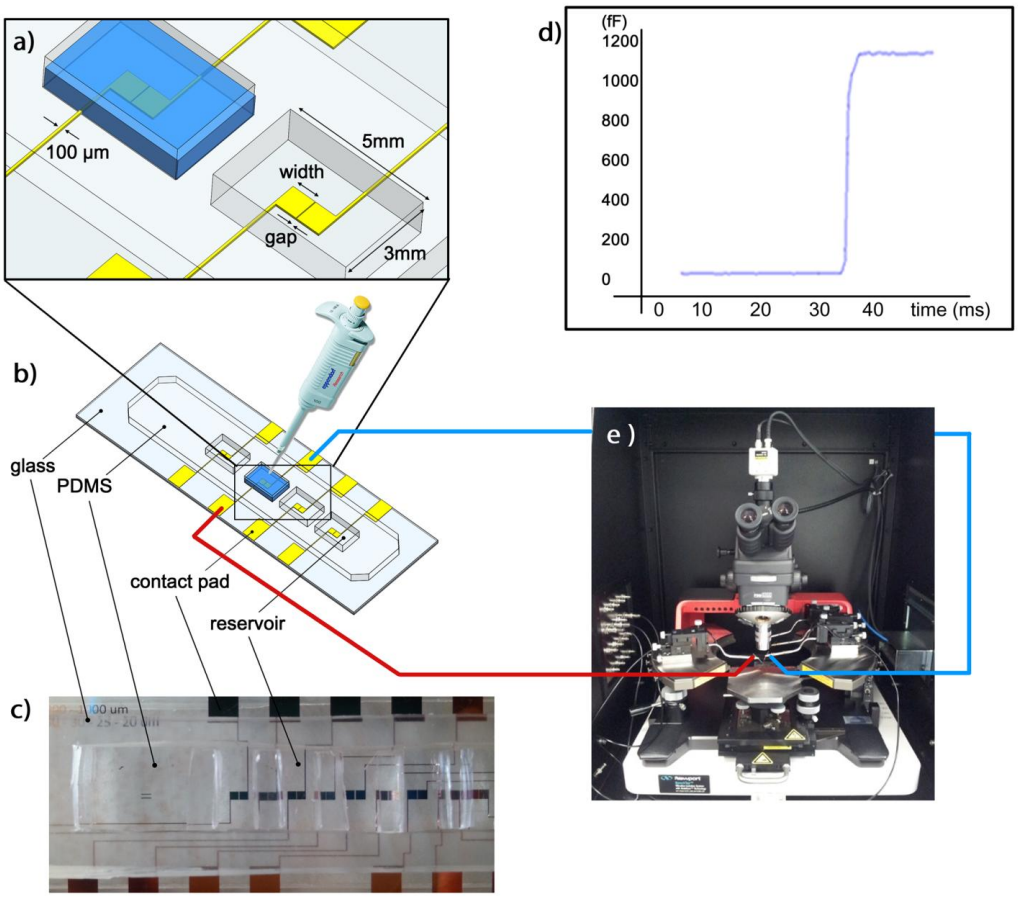

Figure 4.8. Capacitance measurement system for verification purposes: (a) Close-up view of the electrodes and the reservoirs. Capacitance change is measured by pipetting 50 µl of solution, (b) the schematic of the complete device with multiple electrodes, (c) photograph of the fabricated device, (d) exemplary capacitance change plot, (e) probe station for electrical connections.

4.5 Results and Discussion

4.5.1 Analytical model comparison

In order to compare two analytical capacitance formulas, we used Equation 4.1 and Equation 4.3 for different coplanar electrode geometries shown in Table 4.1 and Table 4.2. The coplanar electrodes were passivated either 10 μm PDMS or 360 nm SiO_2. The calculations were done for DI droplets passing through electrodes. As it can be seen from Table 4.1, there is 30 fF difference between two analytical model calculations for SiO_2 passivation layer. During experiments, we got 275 fF signal amplitude for Device 1 geometry and passivation layer thickness. For the same device, the models that Chen *et al*. and Otter proposing result in 170 fF and 147 fF, respectively. Therefore, both analytical models match with 30 fF discrepancy and they are in accordance with experimental result. This models prove that increasing passivation layer thickness decreases capacitance signal amplitude. For same geometry but increasing passivation layer thickness, both analytical models give lower capacitance signal amplitude. We believe that, these two models are quite beneficial for determining electrode geometry and passivation layer thickness.

Table 4.1. Capacitance change results (ΔC) when a DI droplet in silicone oil passes through coplanar electrodes with SiO_2 passivation layer. Both analytical model calculation results are given. The electrode length is equal to microfluidic channel width, 150 μm. The thickness of SiO_2 passivation layer (t_P) is 360 nm. Gap (2a) between electrodes is 50 μm. n is taken from 1 to 10000 while calculating Bessel function in Equation 4.3.

Electrode ID	**Width (*w*) (μm)**	**w/a ratio**	**ΔC using analytical model of Chen *et al*. Eq.4.1 (fF)**	**ΔC using analytical model of Otter Eq.4.3 (fF)**
Device 1	200	8	170,85	147,59
Device 2	400	16	223,70	190,30
Device 3	600	24	252,25	216,72
Device 4	800	32	271,88	235,84
Device 5	1000	40	286,88	250,82
Device 6	1200	48	299,02	263,12

Table 4.2. Capacitance change (ΔC) results when a DI droplet in silicone oil passes through coplanar electrodes with SiO_2 passivation layer. Both analytical model calculation results are given. The electrode length is equal to microfluidic channel width, 150 μm. The thickness of PDMS passivation layer (t_P) is 10 μm. Gap (2a) between electrodes is 50 μm. n is taken from 1 to 10000 while calculating Bessel function in Equation 4.3.

Electrode ID	Width (*w*) (µm)	w/a ratio	Δ*C* using analytical model of Chen *et al*. Eq.4.1 (fF)	Δ*C* using analytical model of Otter Eq.4.3 (fF)
Device 1	200	8	30,73	23,20
Device 2	400	16	94,47	44,53
Device 3	600	24	150,90	63,21
Device 4	800	32	193,66	79,79
Device 5	1000	40	225,59	94,67
Device 6	1200	48	249,98	108,15

4.5.2 Choosing the data rate

Minimizing the baseline noise level is critical to perform high sensitivity droplet content measurements. The shielding of the measurement system including electrodes and measurement read-out rate are two important parameters for the accuracy of AD7746. The read-out rate of AD7746 varies between 10 Hz and 90 Hz. We characterized the baseline noise level by measuring DI water droplets at three different data rates; 10 Hz, 50 Hz and 90 Hz. We observed the smallest noise level at 10 Hz, but it is not high enough to truly analyze the capacitance signal due to low sampling rate. Droplets pass over the sensing region in 200-300 ms, which only yields three data points for each droplet. Although the droplets are of the same size, this leads to significant variation in the capacitance signal amplitude. Measurements at 90 Hz provide enough samples however, the minimal conversion times in AD7746 increases the baseline noise. Comparing our results obtained by different data read-out rate, we set our data rate as 50 Hz in order to keep both the baseline noise and

the signal variation in certain limits. Our baseline noise level at this speed was 25 fF (Figure 4.9).

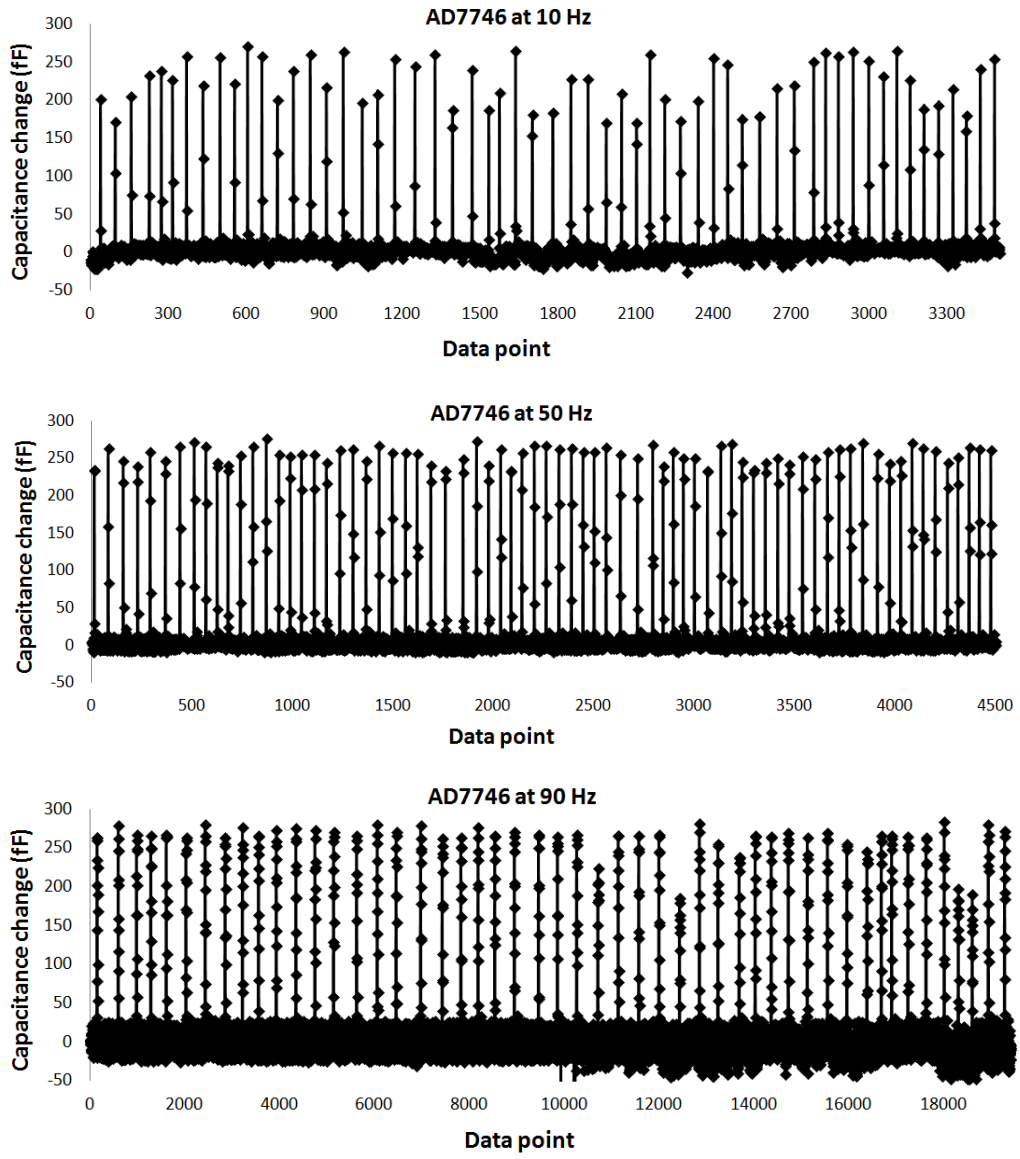

Figure 4.9. Capacitance signal for DI droplets measured at different sampling rates of AD7746.

4.5.3 Finding proper electrode width

The affect of electrode width on capacitance signal was studied using coplanar electrodes that have 200 µm, 400 µm and 600 µm width and 50 µm gap. These

measurements were done using DI droplets with same size and speed. The results were averaged over 50 droplets. As it can be seen in Figure 4.10, there is only 10 fF difference between 200 µm and 600 µm electrodes. We chose to use 200 µm width electrodes in order to keep the footprint of the sensing area as small as possible. It is important to have small sensing area, since the spacing between consecutive droplets should be distant enough to prevent capacitance signal interference between successive droplets. In our study, the spacing between droplets is approximately between 500 and 600 µm. Since the total sensing area of the coplanar electrodes is 450 µm (200 µm + 50 µm + 200 µm), the droplet leaves the sensing area before the next droplet enters the region.

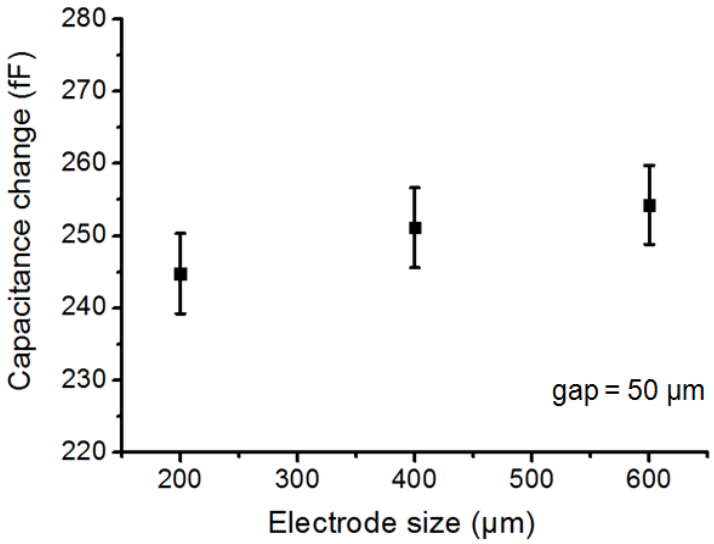

Figure 4.10. Capacitance change for electrodes with varying width. The coplanar electrodes were passivated by 375 nm thick SiO_2. The results were averaged over 50 droplets.

Therefore, we demonstrated that increasing electrode width does not increase capacitive signal amplitude as stated by Chen *et al* [33].

4.5.4 Signal enhancement through thinner passivation layer

The thickness of the passivation layer determines the distance of the microchannel from the electrodes (Figure 4.3). Therefore, it is important to keep the thickness as low as possible to improve the signal amplitude. We used PDMS, toluene-thinned PDMS and SiO_2 to compare different passivation layer types in terms of thickness, uniformity and quality. In order to obtain thinner passivation layer, we studied the effect of spin speed on thickness of PDMS and toluene-thinned PDMS.

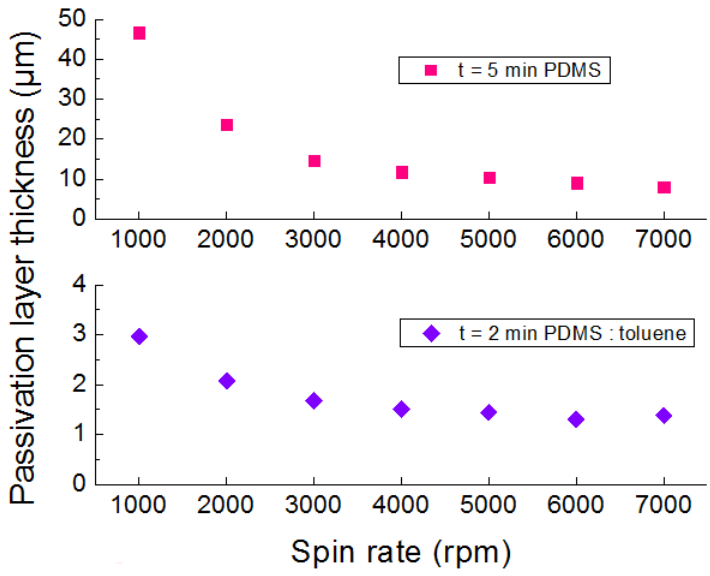

Figure 4.11. PDMS and toluene thinned PDMS thickness. PDMS thickness (red, square) for 5 min. spinning time and PDMS:toluene, 1:3 (w/w) thickness (blue, diamond) for 2 min. spinning time.

As it can be seen from Figure 4.11, increasing spin speed exponentially decreases PDMS passivation layer thickness, but does not significantly decrease the thickness of toluene thinned PDMS. It is because toluene thinned PDMS is much less viscous than PDMS. We measured the viscosities of PDMS and 1:3

(w/w) toluene thinned PDMS at 25 ^{o}C using a rheometer (Anton Paar, MCR-301) as 4220 mPa s and 7.9 mPa s, respectively.

Thickness of PDMS depends on spin speed, duration, mixing ratio of silicone elastomer and curing agent, ambient conditions (temperature, humidity), time between PDMS preparation and spin coating. Since PDMS gets gradually cured at room temperature, the more time passes between the preparation and spinning, the thicker the PDMS passivation layer becomes. Therefore, fresh PDMS mixture should be used for thinner PDMS passivation layer.

Although spinner was used at highest spinning speed, both PDMS and toluene thinned PDMS passivation layer thicknesses were higher than 1 μm. The thickness of passivation layer will plateau at a certain thickness despite substantial increment in spinning time. Therefore, we used PECVD to get nanometer scale thickness and uniformity.

We confirmed the effect of passivation layer thickness on the signal level by measuring the capacitance change signal using PDMS coated electrodes. As it can be seen in Figure 4.12, for 9 μm thick PDMS passivation layer, the capacitance change is 388 fF. Increasing the PDMS passivation layer thickness to 47 μm decreased the capacitance signal to 89 fF. For the same electrodes and measurement setup, we obtained 1054 fF signal amplitude from 375 nm SiO_2 passivation layer coating.

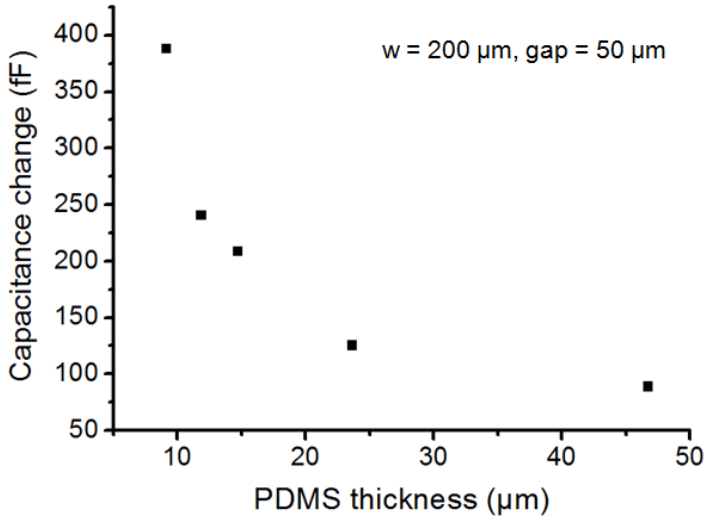

Figure 4.12. Capacitance change recorded using the semiconductor parameter analyzer for DI water at different PDMS passivation layer thicknesses.

Also, we coated the coplanar electrodes with two different SiO_2 passivation layer thicknesses and generated DI droplets using the same Y-junction channel. Then, we measured the capacitance signal amplitudes using our portable measurement system (AD7746 and Arduino). For 180 nm and 360 nm thick SiO_2 passivation layers, we got 514 fF and 275fF capacitance signal amplitudes, respectively. These results prove a 10-fold capacitance signal amplitude enhancement as compared to our previous study where toluene-thinned PDMS passivation layer was used and the capacitance signal was measured as 26 fF [1]. Therefore, it is important to decrease the thickness of the passivation layer using thin film deposition techniques for signal enhancement.

4.5.5 Droplet dielectric content measurement

Figure 4.13 summarizes the capacitive droplet content detection experiments. As seen in Figure 4.13, DI droplets (0% ethanol) ($\mathcal{E}_r$ = 80) and ethanol droplets (100% ethanol) ($\mathcal{E}_r$ = 24) caused the highest and lowest signal change with an average of 275 fF and 55 fF, respectively. At separating boundary of DI water and ethanol a shift toward left occurs due to DI water pressure drop.

For the five cases shown in Figure 4.7, the capacitance signals were analyzed. Figure 4.13 proves the relationship between ethanol concentration of droplets and capacitance signal amplitudes averaged over 50 droplets. It can be seen from Figure 4.13 that increasing droplet ethanol concentration a steady decrease in the detected signal.

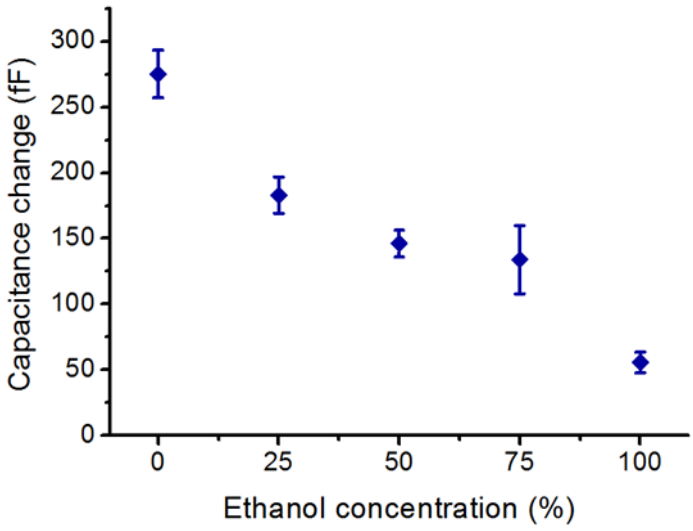

Figure 4.13. Solution dependent capacitance signal amplitudes obtained from Figure 4.7. Error bars denote one standard deviation across 50 droplet peaks. Coplanar electrodes that have width of 200 μm and gap of 50 μm were used. The electrodes were passivated with 360 nm SiO_2.

Using pre-mixed solutions, we obtained the calibration plot (Figure 4.14). This plot confirms that increase in ethanol concentration causes linear decrease in capacitive signal amplitude. DI ethanol mixtures were prepared with ethanol concentrations of 0%, 5%, 10%, 25%, 50%, 75% and 100% (v/v) in vials. For each ethanol concentration, capacitive signal amplitude was averaged over 50 droplets.

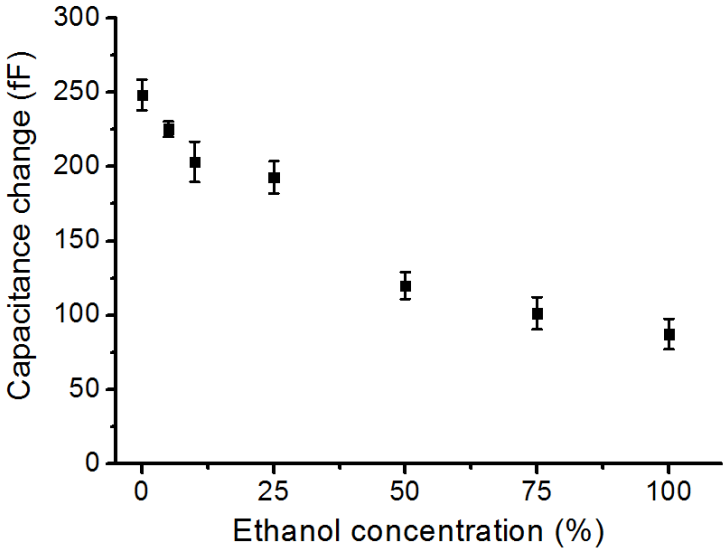

Figure 4.14. Calibration plot obtained by pre-mixed solutions. Error bars denote one standard deviation across 50 droplet peaks.

Figure 4.13 and Figure 4.14 demonstrate that higher ethanol concentration leads to capacitance signal decrease. Pressure fluctuations during droplet break-up process cause fluctuation in relative flow rates of ethanol and DI water. This results in higher standard deviation when mixing is performed on the run (Figure 4.13) as opposed to pre-mixed solutions (Figure 4.14). We obtained the largest standard deviation for 75% ethanol concentration since generating monodisperse droplets at this concentration was very challenging. The increase in droplet ethanol concentration causes a switch from squeezing regime to dripping regime. In this regime, the droplet break-up point is a function of the ethanol and DI water ratio. We observed higher variation in the break-up point during the formation of 75% ethanol concentration droplets that leads to the highest standard deviation in Figure 4.13. Over time partial droplet wetting occurs, since ethanol changes the surface properties of the PDMS microfluidic device.

Elbuken *et al.* have showed that this sensor is suitable for measuring droplet size and speed [1]. Also, they have demonstrated that any size variation in droplets affects the capacitance signal amplitude. Increasing droplet size or

decreasing droplet speed leads to higher capacitance signal amplitude. Therefore, the variation in Figure 4.13 and Figure 4.14 is partially due to the variation in droplet size and speed. We generated approximately 450 μm length droplets during the measurements. We observed smaller standard deviations in Figure 4.14 compared to Figure 4.13, since monodispersity was higher for the droplets that were generated using the pre-mixed solutions. Both measurements follow a linear trendline other than 75% ethanol concentration measurements. As it can be seen from Figure 4.13 and Figure 4.14, it is possible to resolve 5% change in ethanol concentration using our system. This change corresponds to a dielectric constant unit resolution of less than 3.

4.5.6 Verification

The linear decrease of capacitance signal due to the increasing ethanol concentration was verified using a semiconductor parameter analyzer. Since the sensing domain is completely covered with the solutions, the variation due to changing droplet size was eliminated. We observed a linear response with R^2=0.99 (Figure 4.15). These measurements are in agreement with the theoretical predictions that the signal linearly decreases with increasing ethanol concentrations. The signal for DI sample ($\mathcal{E}_r$ = 80) and ethanol sample ($\mathcal{E}_r$ = 24) were measured as 1054 fF and 276 fF, respectively. These results ensured that the variation in droplet generation dynamics leads to the variation and nonlinearity shown in Figure 4.13 and Figure 4.14. Moreover, content change of dispersed phase affects both viscosity and wetting conditions. This makes alteration to droplet break-up point at the T-junction.

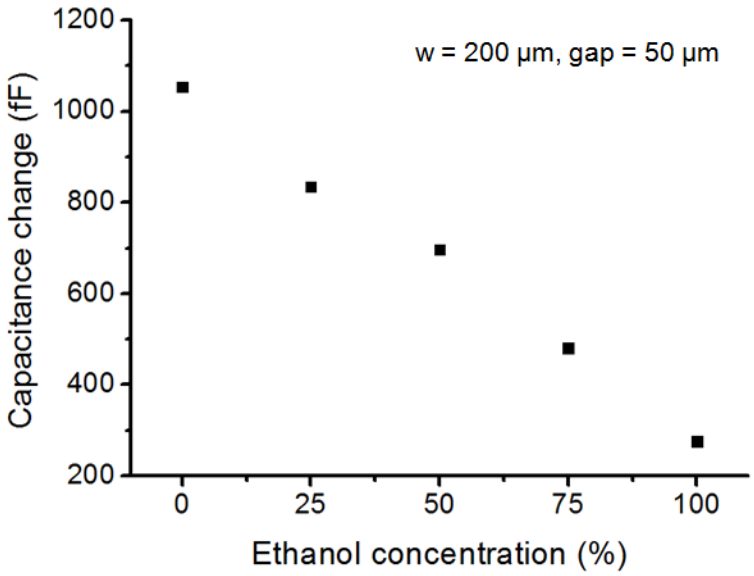

Figure 4.15. Capacitance change recorded using the semiconductor parameter analyzer. 50 µl droplets were precisely pipetted onto the 375 nm SiO_2 passivated electrodes using the pre-mixed DI water ethanol solutions.

4.6 Possible Future Applications

We believe that it is an assignment for us to consider the manufacturability and scalability of the technologies we develop as the microfluidic community. This study takes a step in that direction by utilizing very low cost electronics for high sensitivity measurement of droplet content (Arduino Nano $20, AD7746 $4). This system is capable of measuring droplet size and speed as well as droplet counting. We think that our system is suitable for biochemical assays. For instance, it is possible to use this system for measuring DNA content in a single cell. Sohn *et al.* have developed a microfluidic system that detects DNA content of eukaryotic cell. They evaluated each peak as a cell passing between the electrodes (Figure 4.16) [39]. As seen from their results in Figure 4.16, G_2/M phase in a single cell corresponds to 25 fF capacitance change, which can be detected using our system. Moreover, monitoring metabolic activity of cells encapsulated in droplets using coplanar electrodes will be an interesting application of this system [40]. Joensson *et al.* have detected cell viability in

microdroplets using a optical detection system [31]. The metabolic activity of yeast cells in droplets turns glucose into byproducts which diffuse out of the droplet by osmosis. Therefore, droplets encapsulating active cells shrink in size over time. Interestingly, the cellular activity of yeast cells in droplets lead to production of ethanol in the meantime. We believe our system is suitable for monitoring the same activity by measuring the ethanol concentration change. Another potential application of this system is dielectric indexing of droplets as an alternative to chemical indexing that is accomplished by encoded particles or labeled beads [41].

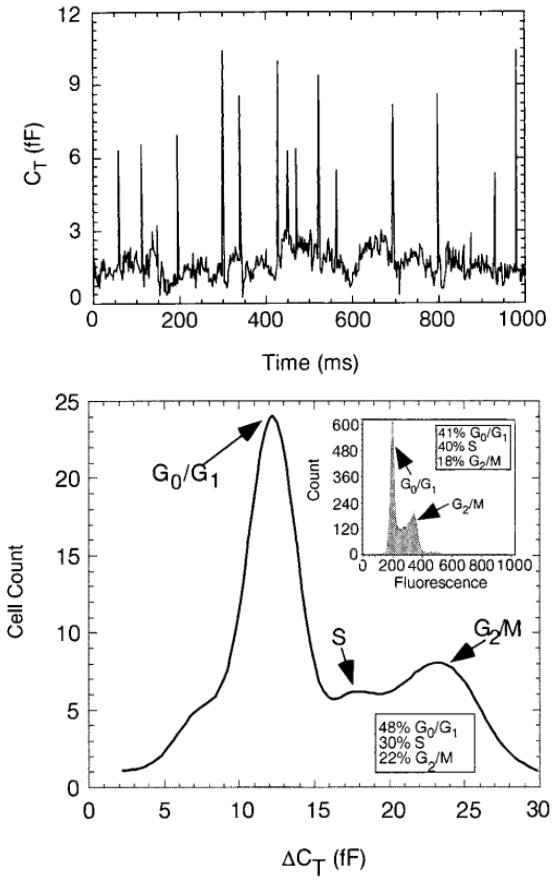

Figure 4.16. (Top image) Each peak corresponds to a single cell flowing past to electrodes. (Bottom image) Distribution of cell capacitance from 2 DNA phase (G_0/G_1) to 4 DNA phase (G_2/M). Reprinted (adapted) with permission from ref. [39] (Copyright 2000 Proceedings of the National Academy of Sciences).

4.7 Conclusion

In this chapter, high sensitivity capacitive droplet content detection was demonstrated using a scalable, portable, and cost-effective method. It was shown that there is a linear relationship between the decrease in dielectric permittivity of droplet content and the capacitive signal. These results were verified using a semiconductor parameter analyzer. It was demonstrated that sensitivity can be improved by minimizing the thickness of the passivation layer. It was shown that the two analytical models are in agreement and they can be used for designing coplanar electrodes. It was demonstrated that increasing electrode width does not exceedingly change capacitance signal amplitude. It is believed that droplet content can be detected in robust, precise and scalable manner at high sensitivity using commercially available, low-cost electrical components. Moreover, the presented system is an alternative for bulky and costly bench-top analyzers.

Chapter 5

Droplet Sorting Using 2D Coplanar and 3D EGaIn Electrodes

5.1 Introduction

Dielectrophoretic (DEP) platforms that are integrated with lab-on-a-chip systems are used to manipulate, sort, characterize, transport microparticles or cells in a controllable, accurate and selective way. Separating viable and non-viable cells, blood cells from plasma, blood cells into its components (monocytes, granulocytes, T and B cells), investigating cell response to different drugs, sorting cell laden microdroplets are some applications of DEP platforms [42]–[46].

Dielectophoretic systems is realized using different electrode configurations. Interdigitated, microwell, contactless, extruded, top-bottom patterned and side-wall patterned electrodes are some of the configurations that are used to apply electric field. Moreover, these systems have different operation types such as gravitational field-flow-fraction (FFF), lateral sorting, barrier-assisted, multiple frequency, pulsed DEP, immune-assisted, and light induced [42].

Dielectrophoresis is the movement of electrically polarizable particles in a non-uniform electric field. Under non-uniform electric field, the Coulomb forces on sides of a spherical particle is different, therefore particle movement occurs. The force leading to particle movement is DEP force. This force is expected to overcome gravity, hydrodynamic drag, intra-particle and surface-particle adhesive forces for manipulation of the particles [42]. Designing a DEP platform requires taking into account of different characteristics. In a LOC integrated DEP system, incompressible Navier-Stokes equations should be solved with DEP force equations simultaneously while considering drag, lifting and sedimentation forces. Like electrical properties of materials, viscosity, density and velocity of the medium (hydrodynamic properties of the medium) become important in these systems [43].

In this chapter, droplet sorting was demonstrated using 2D coplanar and 3D EGaIn electrodes. The main aim was to gain knowledge about DEP.

In order to realize droplet sorting using 2D coplanar electrodes, we imitated the device configuration that is presented by Ahn *et* al (Figure 5.1). They fabricate a flow focusing device that is bonded to ITO (indium-thin-oxide) electrode deposited glass slide. The tip of electrodes are aligned to proximity of the center of the microchannels to maximize the force exerted on droplets. Microfluidic channels are expanded at the sorting region [46].

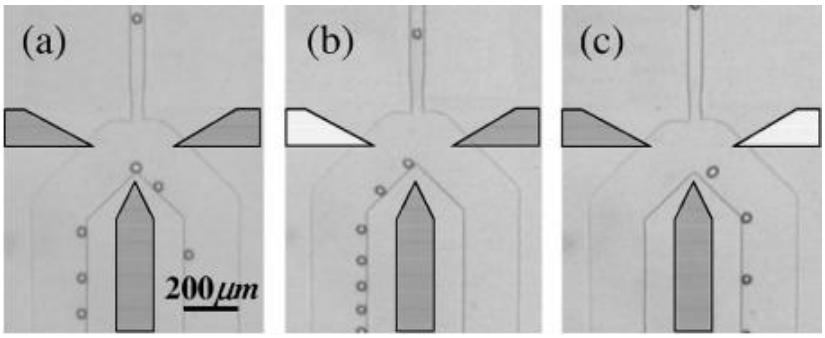

Figure 5.1. Microscope image of DEP device designed by Ahn *et al*. a) The dark gray areas are ITO electrodes. The lower and side electrodes are for applying ground and voltage, respectively. White area represents the energized electrodes. b) Droplets flow to left channel when left electrode is energized. c) Droplets flow to right channel when right electrode is energized. Reprinted (adapted) with permission from ref. [46]. (Copyright 2006 American Physics Society).

3D EGaIn electrodes were fabricated using the technique that was developed by So *et al* [47]. In 2011, So *et al.* injected eutectic gallium indium (EGaIn) to the microchannels in order to fabricate microelectrodes. EGaIn is composed of eutectic alloys; gallium and indium. It is liquid at room temperature since its melting point is -19 ^{o}C. It has low viscosity (twice the viscosity of water), so it is possible to inject it into the PDMS microchannels using syringes without need of heating. Before this method, 3D electrodes in microchannels were fabricated by injecting molten indium into PDMS. The fabrication consists of three steps: silanization of the microchannels, injection of molten solder into channels and cool molten solder down. Although, these steps seem quite easy for the reader, it still needs expertise for silanization and injecting molten solder into the channels without letting it to cool down [48]. This method, microsolidics, opened new gates for fabricating microstructures in PDMS without a need of clean room [49].

5.2 Dielectrophoresis (DEP) Theory

Dielectrophoresis defines the movement of dielectric particles in a non-uniform electric field. Under electric field, charges in the particle are induced at the particle medium interface and dipoles are aligned parallel to the electric field. Net force on a particle under uniform electric field is zero due to equal Coulomb forces. Therefore, there is no movement of the particle under uniform electric field (Figure 5.2.A). However, under non-uniform electric field the net force on the particle is not zero due to unequal Coulomb forces on each half of the particle. This results in movement of the particle (Figure 5.2.B) [42].

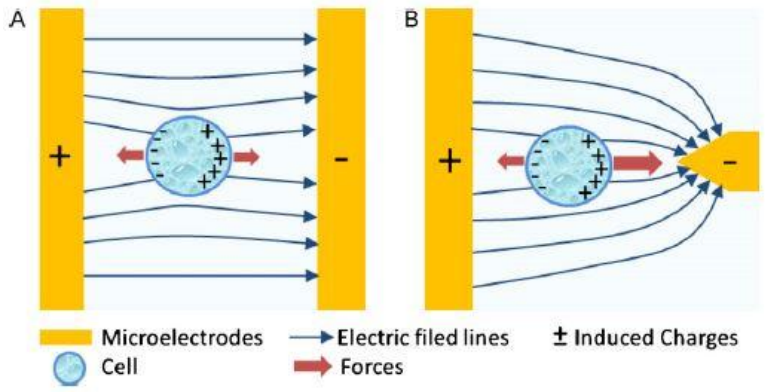

Figure 5.2. Polarizable particle response to (A) uniform (B) non uniform electric field. Reprinted (adapted) with permission from ref. [42]. (Copyright 2006 Elsevier).

The resulting force that leads to particle movement is dielectrophoretic force. Under an alternating current (AC) field, time-averaged DEP force for a spherical particle is

$$< F_{DEP} >= 2 * \pi * \mathcal{E}_m * \mathcal{E}_0 * r^3 * Re(f_{CM}) \nabla |E|^2 \quad (5.1)$$

where $\mathcal{E}_m$ is the dielectric permittivity of the medium, $\mathcal{E}_0$ is the dielectric permittivity of the vacuum ($8.854*10^{-12}$ *F/m*), *r* is the particle radius, $Re(f_{CM})$ is

the real part of the Clausius-Mossotti factor and ∇E is the gradient of the applied electric field [42]. In this formula, Clausius-Mossotti factor (f_{CM}) relates polarizability of a spherical particle with respect to its surrounding medium

$$f_{CM} = \frac{\mathcal{E}_p^* - \mathcal{E}_m^*}{\mathcal{E}_p^* + 2\mathcal{E}_m^*} \tag{5.2}$$

where $\mathcal{E}_p^*$ is the complex permittivity of the particle and $\mathcal{E}_m^*$ is the complex permittivity of the medium. $\mathcal{E}^*$ can be defined as

$$\mathcal{E}_p^* = \mathcal{E}_p - j\frac{\sigma_p}{w} \tag{5.3.a}$$

$$\mathcal{E}_m^* = \mathcal{E}_m - j\frac{\sigma_m}{w} \tag{5.3.b}$$

where ε is the dielectric permittivity, σ is the electrical conductivity, w is the angular frequency of electric field that is applied to the electrodes.

For low electric field frequency, the conductivity of the particle and medium determine the sign of Clausius-Mossotti factor. On the other hand, permittivity of the medium and particle become dominant under high electric field frequency.

$$\lim_{w\to 0} Re(f_{CM}) = \frac{\sigma_p - \sigma_m}{\sigma_p + 2\sigma_m} \tag{5.4.a}$$

$$\lim_{w\to \infty} Re(f_{CM}) = \frac{\mathcal{E}_p - \mathcal{E}_m}{\mathcal{E}_p + 2\mathcal{E}_m} \tag{5.4.b}$$

Clausius-Mossotti factor reaches its highest value (1.00) due to higher particle conductivity compared to medium conductivity according to Equation 5.4.a. Higher conductivity of the medium results in minimum value (-0.5) of the

Clausius-Mossotti factor. This is also valid for permittivies of the particle and the medium according to Equation 5.4.b.

The sign of real part of the Clausius-Mossotti factor determines whether a particle is affected by positive or negative DEP. When particle is more polarizable than its medium ($\varepsilon_p^* > \varepsilon_m^*$ so that Re(f_{CM}) > 0), particle is affected by positive DEP (pDEP) force and pushed towards the highest electric field areas. On the other hand, when medium is more polarizable than particle ($\varepsilon_m^* > \varepsilon_p^*$ so that Re(f_{CM}) < 0), particle is affected by negative DEP (nDEP) force and repelled from the highest electric field areas [43].

The crossover frequency is identification of the point where the DEP force switches from nDEP to pDEP or vice versa. This frequency is sufficient enough to understand the electrical polarizability of the materials. The crossover frequency is the point where real part of the Clausius-Mossotti factor is equal to zero

$$f_{cross} = \frac{1}{2\pi}\sqrt{\frac{(\sigma_m - \sigma_p)(\sigma_p - 2\sigma_m)}{(\varepsilon_p - \varepsilon_m)(\varepsilon_p + 2\varepsilon_m)}} = \frac{1}{2\pi}\sqrt{\frac{(\sigma_m - \sigma_p)}{(\varepsilon_p - \varepsilon_m)}} f_{MW} \tag{5.5}$$

$$f_{cross} = \frac{1}{2\pi\tau_{MW}} \tag{5.6}$$

$$\tau_{MW} = \frac{(\varepsilon_p + 2\varepsilon_m)}{(\sigma_p + 2\sigma_m)} \tag{5.7}$$

where f_{cross} is the crossover frequency, f_{MW} is the Maxwell-Wagner relaxation frequency and τ_{MW} is Maxwell-Wagner charge relaxation time [50].

In the literature, there are numerous formulas for real part of the Clausius-Mossotti factor like following two notations. For calculation of the real part of the Clausius-Mossotti factor, we will explicitly formulate both of them.

$$\mathbf{1}.\,Re\,(f_{CM}) = \frac{\varepsilon_m''(\varepsilon_p''-2\varepsilon_m'')+\varepsilon_p'^2+\varepsilon_p''^2+\varepsilon_p'\varepsilon_m'-2\varepsilon_m'^2}{\varepsilon_p'^2+\varepsilon_p''^2+4\varepsilon_p'\varepsilon_m'+4\varepsilon_m'^2+4\varepsilon_m''(\varepsilon_p''+\varepsilon_m'')} \tag{5.8}$$

$$\text{where } \varepsilon_p^{\sim} = \varepsilon_p' - j\varepsilon_p'' \tag{5.9.a}$$

$$\text{so that } \varepsilon_p'' = \frac{\sigma_p}{w} \tag{5.9.b}$$

$$\mathbf{2}.\,Re(f_{CM}) = \frac{(\varepsilon_p-\varepsilon_m)w^2\ {\tau_{MW}}^2}{(\varepsilon_p+2\varepsilon_m)(1+w^2\ {\tau_{MW}}^2)} + \frac{(\sigma_p-\sigma_m)}{(\sigma_p+2\sigma_m)(1+w^2\ {\tau_{MW}}^2)} \tag{5.10}$$

where τ_{MW} is the Maxwell-Wagner charge relaxation time in Equation 5.7.

For finding Notation 1, Clausius-Mossotti factor is written using Equation 5.2 and Equation 5.9 to find Equation 5.11,

$$f_{CM} = \frac{\varepsilon_p'-j\varepsilon_p''-\varepsilon_m'+j\varepsilon_m''}{\varepsilon_p'-j\varepsilon_p''+2\varepsilon_m'-2j\varepsilon_m''} \tag{5.11}$$

In order to find real part of the Clausius-Mossotti factor, both nominator and denominator are multiplied by $\varepsilon_p' + 2\varepsilon_m' + j(\varepsilon_p'' + 2\varepsilon_m'')$. For ease of calculation nominator and denominator will be written separately. After multiplication, nominator (A) of the Equation 5.11 becomes

$$A = \varepsilon_p'^2 + 2\varepsilon_p'\varepsilon_m' + j\varepsilon_p'\varepsilon_p'' + 2j\varepsilon_p'\varepsilon_m'' - j\varepsilon_p'\varepsilon_p'' - 2j\varepsilon_m'\varepsilon_p'' + \varepsilon_p''^2 + 2\varepsilon_p''\varepsilon_m'' - \varepsilon_p'\varepsilon_m' - 2\varepsilon_m'^2 - j\varepsilon_m'\varepsilon_p'' - 2j\varepsilon_m''\varepsilon_m' + j\varepsilon_p'\varepsilon_m'' + 2j\varepsilon_m''\varepsilon_m' - \varepsilon_p''\varepsilon_m'' - 2\varepsilon_m''^2 \tag{5.12}$$

After cancelling out j terms and making the calculation, nominator becomes

$$A = \varepsilon_p'^2 + \varepsilon_p'\varepsilon_m' + \varepsilon_p''\varepsilon_m'' - 2\varepsilon_m'^2 + \varepsilon_p''^2 - 2\varepsilon_m''^2 \tag{5.13}$$

After multiplication, denominator (B) of the Equation 5.11 becomes

$$B = (\varepsilon'_p + 2\varepsilon'_m)^2 + (\varepsilon''_p + 2\varepsilon''_m)^2 = \varepsilon'^2_p + 4\varepsilon'_p\varepsilon'_m + 4\varepsilon'^2_m + \varepsilon''^2_p + 4\varepsilon''_p\varepsilon''_m + 4\varepsilon''^2_m \quad (5.14)$$

Bringing nominator and denominator together, real part of the Clausius-Mossotti factor becomes

$$Re(f_{CM}) = \frac{\varepsilon'^2_p+\varepsilon'_p\varepsilon'_m+\varepsilon''_p\varepsilon''_m-2\varepsilon'^2_m+\varepsilon''^2_p-2\varepsilon''^2_m}{\varepsilon'^2_p+4\varepsilon'_p\varepsilon'_m+4\varepsilon'^2_m+\varepsilon''^2_p+4\varepsilon''_p\varepsilon''_m+4\varepsilon''^2_m} \quad (5.15)$$

Using Equation 5.9.b

$$Re(f_{CM}) = \frac{\varepsilon_p^2+\varepsilon_p\varepsilon_m+\frac{\sigma_p\sigma_m}{w^2}-2\varepsilon_m^2+\frac{\sigma_p^2}{w^2}-2\frac{\sigma_m^2}{w^2}}{\varepsilon_p^2+4\varepsilon_p\varepsilon_m+4\varepsilon_m^2+\frac{\sigma_p^2}{w^2}+4\frac{\sigma_p\sigma_m}{w^2}+4\frac{\sigma_m^2}{w^2}} \quad (5.16)$$

By multiplying both nominator and denominator by w^2 and then simplifying them with w^2, the real part of the Clausius-Mossotti factor becomes

$$Re(f_{CM}) = \frac{\varepsilon_p^2w^2+\varepsilon_p\varepsilon_mw^2+\sigma_p\sigma_m-2\varepsilon_m^2w^2+\sigma_p^2-2\sigma_m^2}{\varepsilon_p^2w^2+4\varepsilon_p\varepsilon_mw^2+4\varepsilon_m^2w^2+\sigma_p^2+4\sigma_p\sigma_m+4\sigma_m^2} \quad (5.17)$$

Equation 5.17 shows the real part of the Clausius-Mossotti factor when Notation 1 is used. When Notation 2 is used and Equation 5.7 is put into the Equation 5.10,

$$Re(f_{CM}) = \frac{(\varepsilon_p-\varepsilon_m)w^2\left[\frac{(\varepsilon_p+2\varepsilon_m)}{(\sigma_p+2\sigma_m)}\right]^2}{(\varepsilon_p+2\varepsilon_m)\left[1+w^2\left[\frac{(\varepsilon_p+2\varepsilon_m)}{(\sigma_p+2\sigma_m)}\right]^2\right]} + \frac{(\sigma_p-\sigma_m)}{(\sigma_p+2\sigma_m)\left[1+w^2\left[\frac{(\varepsilon_p+2\varepsilon_m)}{(\sigma_p+2\sigma_m)}\right]^2\right]} \quad (5.18)$$

Left hand side of the plus is multiplied by $(\sigma_p + 2\sigma_m)$ and right hand side of the plus is multiplied by $(\varepsilon_p + 2\varepsilon_m)$ and denominators become equal.

$$Re(f_{CM}) = \frac{(\varepsilon_p - \varepsilon_m)w^2 \frac{(\varepsilon_p + 2\varepsilon_m)^2}{(\sigma_p + 2\sigma_m)} + (\sigma_p - \sigma_m)(\varepsilon_p + 2\varepsilon_m)}{(\varepsilon_p + 2\varepsilon_m)(\sigma_p + 2\sigma_m) + \left[1 + w^2 \left[\frac{(\varepsilon_p + 2\varepsilon_m)}{(\sigma_p + 2\sigma_m)}\right]^2\right]} \quad (5.19)$$

Multiplying both nominator and denominator by $(\sigma_p + 2\sigma_m)$

$$Re(f_{CM}) = \frac{(\varepsilon_p - \varepsilon_m)w^2 (\varepsilon_p + 2\varepsilon_m)^2 + (\sigma_p - \sigma_m)(\sigma_p + 2\sigma_m)(\varepsilon_p + 2\varepsilon_m)}{(\varepsilon_p + 2\varepsilon_m)\left[(\sigma_p + 2\sigma_m)^2 + w^2 (\varepsilon_p + 2\varepsilon_m)^2\right]} \quad (5.20)$$

By taking both nominator and denominator $(\varepsilon_p + 2\varepsilon_m)$ parenthesis and then simplifying them

$$Re(f_{CM}) = \frac{(\varepsilon_p - \varepsilon_m)w^2 (\varepsilon_p + 2\varepsilon_m) + (\sigma_p - \sigma_m)(\sigma_p + 2\sigma_m)}{(\sigma_p + 2\sigma_m)^2 + w^2 (\varepsilon_p + 2\varepsilon_m)^2} \quad (5.21)$$

For ease of calculation, nominator (C) and denominator (D) of Equation 5.21 are calculated separately.

$$C = \varepsilon_p^2 w^2 + 2\varepsilon_p \varepsilon_m w^2 - \varepsilon_p \varepsilon_m w^2 - 2\varepsilon_m^2 w^2 + \sigma_p^2 + 2\sigma_p \sigma_m - \sigma_p \sigma_m - 2\sigma_m^2 \quad (5.22)$$

$$D = \varepsilon_p^2 w^2 + 4\varepsilon_p \varepsilon_m w^2 + 4\varepsilon_m^2 w^2 + \sigma_p^2 + 4\sigma_p \sigma_m + 4\sigma_m^2 \quad (5.23)$$

By bringing nominator and denominator together, the real part of the Clausius-Mossoti factor becomes

$$Re(f_{CM}) = \frac{\varepsilon_p^2 w^2 + \varepsilon_p \varepsilon_m w^2 + \sigma_p \sigma_m - 2\varepsilon_m^2 w^2 + \sigma_p^2 - 2\sigma_m^2}{\varepsilon_p^2 w^2 + 4\varepsilon_p \varepsilon_m w^2 + 4\varepsilon_m^2 w^2 + \sigma_p^2 + 4\sigma_p \sigma_m + 4\sigma_m^2} \quad (5.24)$$

Therefore, Equation 5.17 or Equation 5.24 can be used for calculating the real part of the Clausius-Mossoti factor.

5.3 Design and Fabrication

5.3.1 2D DEP device design and fabrication

In the literature, it is common to use two channels one of which has lower resistance than the other, so that unwanted droplets goes to lower resistance channel and droplets of interest are sorted using DEP side electrodes [51]. However, taking DEP device that was fabricated by Ahn *et al*. as an example, we designed our 2D DEP electrodes and microchannels since we wanted to sort droplets on demand. For this purpose, we used two different microchannel and electrode designs. Like in the example, we expanded microchannels after the bifurcation and aligned DEP electrodes closer to the center of the microchannels. Fabrication of 2D electrodes and microchannels are likewise fabricated as explained in Chapter 3. Hydrodynamic flow focusing device was used for generating slug like droplets at high speeds [17]. DEP electrodes were passivated with 550 nm SiO_2. Channel, electrode and passivation layer heights were measured using profilometer, AFM and ellipsometer respectively as explained in Chapter 3. Microchannel height is 80 μm and electrode height is 220 nm. The fabricated device is shown in Figure 5.3. Microchannels were fabricated using standard soft lithography methods that is explained in Chapter 3. As can be seen from Figure 5.3, oil channels are wider than water channels in order to ensure timing of reaching oil and water to the droplet generation part is equal. Increasing oil channel width decreases channel resistance and increases flow rate of the oil according to Hagen-Poiseuille law. Side injection channels were added to the design for increasing the distance between consecutive droplets. However, these channels were not used since distance between droplets were adjusted properly by changing pressure of the oil and water. Although there is a passivation layer between channels and electrodes, droplets were pinning to the electrode tips when 1200 V AC signal is applied. Therefore,

this passivation layer was not thick enough for preventing electrodes from hydrolysis of water. After hydrolysis of water, electrode tips become useless. The passivation layer of the device was not increased since the microchannels will be integrated to the capacitive sensors in future. Since we do not use surfactant in our experiments, pinning of droplets to the electrodes and slowing droplets due to decreasing resistance at the bifurcation leads to droplet merging. Consequently, the proper modifications were done for second design.

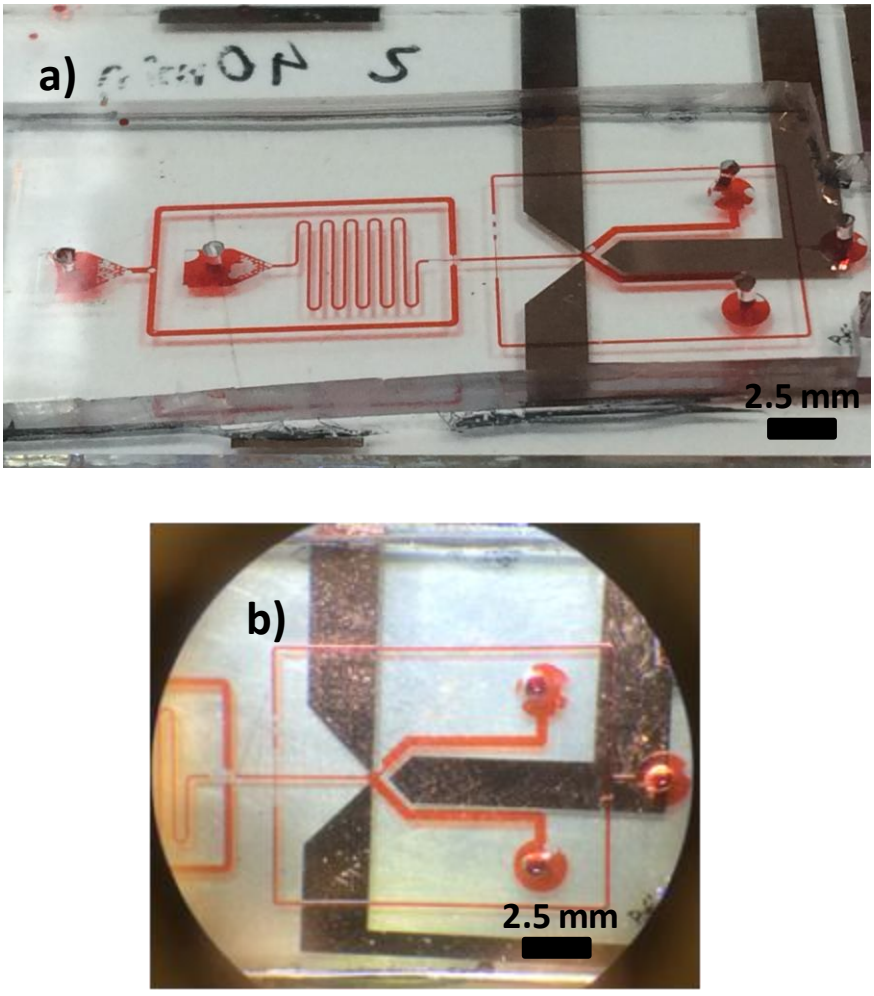

Figure 5. 3 a) 2D DEP electrodes that are bonded to flow focusing device with side junctions. b) 3D microscope photograph that shows microchannel bifurcation

Unlike the first microchannel design, in second design, after bifurcation sorting channels were not expanded in order to prevent droplets from merging. Also, side injection channels were removed. The distance between ground and voltage applied DEP electrodes was increased, so electrode tips were not under but by side of the channels. This not only prevents electrode tips from degradation, but also exerts DEP force on droplets way before bifurcation. Since electrode tips are not beneath the microchannel, there is no need for thin film deposition as a passivation layer. The fabricated device is shown in Figure 5.4. The microchannel and electrode fabrication are same as discussed in Chapter 3. Same characterization techniques were also used for second design. Therefore, channel and electrode heights were measured as 80 μm and 220 nm, respectively. Droplet sorting on demand was accomplished using this design.

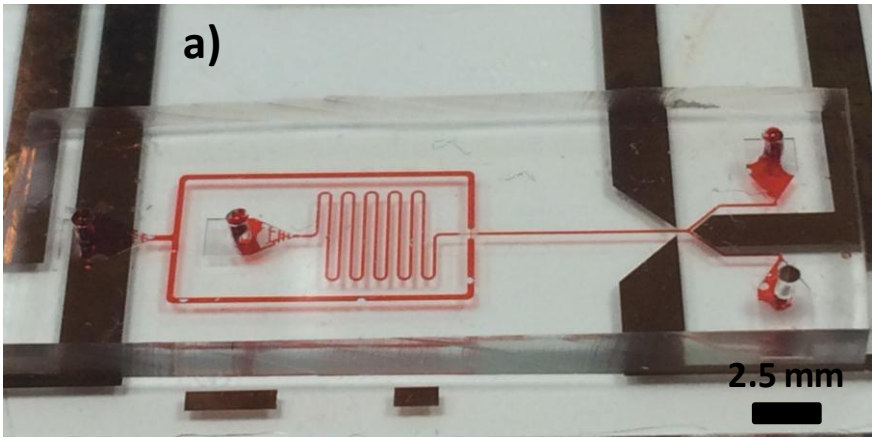

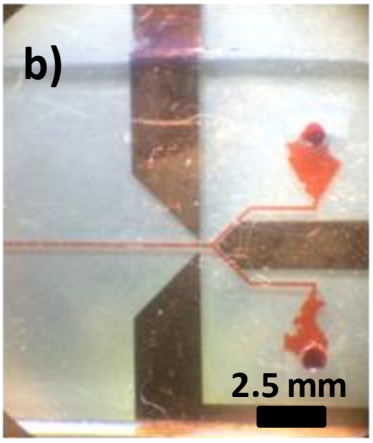

Figure 5. 4. a) 2D DEP electrodes that are bonded to flow focusing device. b) 3D microscope photograph that shows microchannel bifurcation, after bifurcation channels do not expand.

Alignment of DEP electrodes to the channels were done manually. After microchannels and glass slides that have electrodes on it were subjected to the air plasma, a drop of methanol dripped onto the glass [52]. Under the microscope, alignment was done and bonded device were put to the 100 ^{o}C hot plate. Since the methanol is volatile liquid, it does not affect bonding of channel to the glass slide. Bonding parameters can be found in Chapter 3.

A microscope stage is designed and fabricated in order to do 2D DEP experiments. As can be seen from Figure 5.5, a regular microscope stage is

replaced with a polymethylmethacyrlate (PMMA) stage that a peripheral component interconnect (PCI) and a connector (MERITEC, 980550-120-ACFR) were integrated to it. The stage is designed in CAD software and manufactured using a laser cutting system. PCI was used to provide connection between DC to AC inverter and connector. This connector eliminates welding procedure and fixes the device to the stage. Since all the connector contacts are only at one side, electrode contact pads are designed and fabricated accordingly.

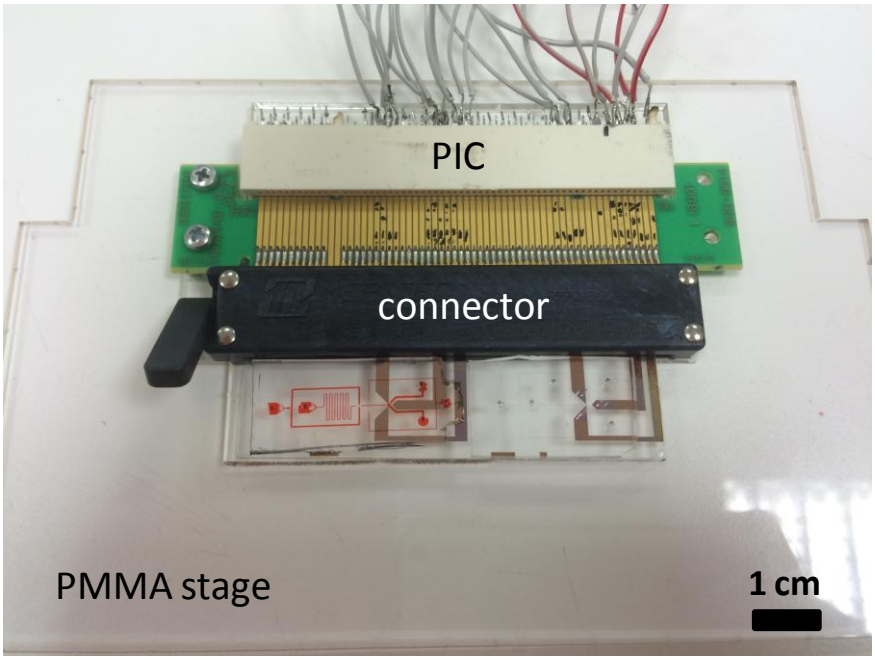

Figure 5. 5. Photograph of the PMMA stage. A PIC and a connector is integrated to PMMA in order to provide connection between DC to AC inverter and 2D DEP device.

5.3.2 3D EGaIn electrode and channel design and fabrication

Taking the technique that was developed by So *et al*. as an example, we fabricated 3D EGaIn electrodes. The same microchannel design in Figure 5.4

was used for 3D DEP device. To fabricate 3D DEP electrodes, three more microchannel structures were designed as shown in Figure 5.6. Different than fabrication of 2D DEP device, which requires both soft lithography techniques and thin film metal deposition, in the case of 3D DEP device fabrication only standard soft lithography techniques were used for both microchannels and DEP electrodes. These additional microchannels are filled by eutectic gallium indium (EGaIn, 75.5% Ga and 24.5% In, by weight) to turn them into DEP electrodes. The height of microchannels and DEP electrodes were measured as 80 μm using a profilometer. As noticed in Figure 5.6, all of the DEP electrode channels have two branches and holes. EGaIn filled pipette tip was placed one of the holes of the DEP electrode channel. Then, EGaIn was sucked from the other hole of the same electrode channel. Two-branched structure of DEP channels ensures uniform distribution of EGaIn throughout the DEP electrode. Since the electrodes are embedded in PDMS, there is no need for manual alignment like we did for 2D DEP electrodes.

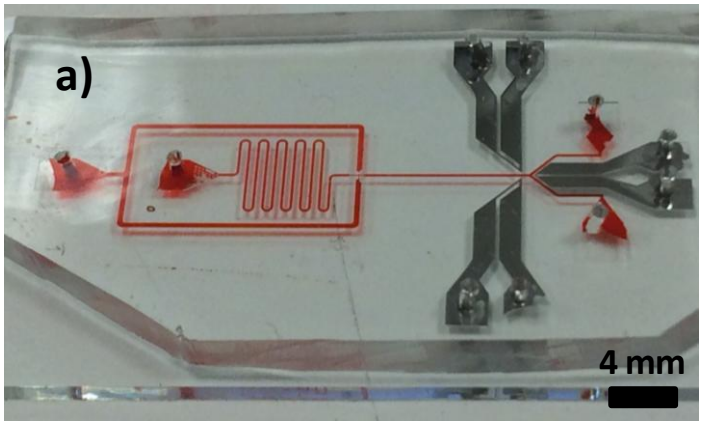

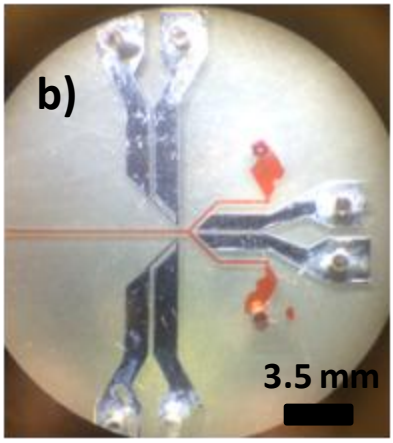

Figure 5. 6. a) 3D DEP electrodes that are bonded to flow focusing device. b) 3D microscope photograph that shows microchannel bifurcation, after bifurcation channels do not expand. EGaIn was injected to microchannels in order to fabricate 3D DEP electrodes.

5.4 Experimental Procedure

Experiments were conducted using devices that are shown in Figure 5.7. Hydrodynamic flow-focusing device was used to generate droplets at different size and speeds. After droplet generation section, there is a bifurcation for droplet sorting on demand. Bifurcation channels have equal resistances. 2D and 3D DEP electrodes both placed close to the bifurcation. Droplets were generated using a pressure pump. Silicone oil with 50 mPa s viscosity and DI

water were used as continuous and dispersed phase respectively. In order to observe droplet size, speed and sorting an inverted microscope was used.

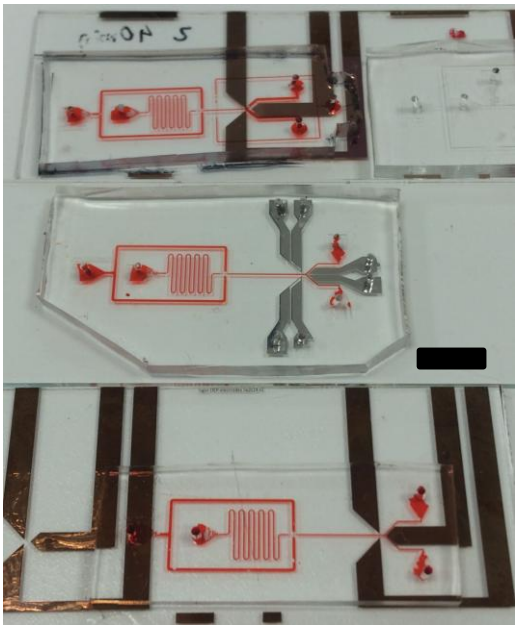

Figure 5. 7. Photograph of all DEP sorters. Scale bar is 1 cm.

Generally for DEP experiments signal generators are used for finding optimum frequency and voltage. However, these equipments are both bulky and expensive for a hand-held, integrated microfluidic system. Instead of a signal generator, we used a portable and cheap DC to AC inverter (TDK, CXA-M10L-L) for supplying AC signal to the system. This inverter was fed by 12V DC voltage. It transforms the DC voltage to fixed frequency and voltage AC signal. The inverter gives 31 kHz frequency and 1200 V AC signal. DC power supply (T-T Technic, MCH-305T- II) was used to feed the inverter. Also, 9V and 3V two batteries can be serially connected in order to feed inverter. Although it is not possible to find optimum frequency and voltage with this inverter, it is a quite useful and cheap tool. Having small foot-print and being portable, this inverter gives chance to get rid of bulky components i.e signal generators.

The experiment set-up for 2D DEP experiments can be seen in Figure 5.8. A laser cutted PMMA microscope stage was used. The connector was fixed to the stage and a PIC was locked to the connector. The connector has a special locking mechanism that the device can be fixed easily. The electrical connections were done between PIC, inverter and DC power supply using alligator cables. 3D DEP experiment set-up is same as 2D experiment set-up without PMMA stage (Figure 5.8). For 3D DEP experiments, needles were utilized to make the connection between the DEP electrodes and the inverter.

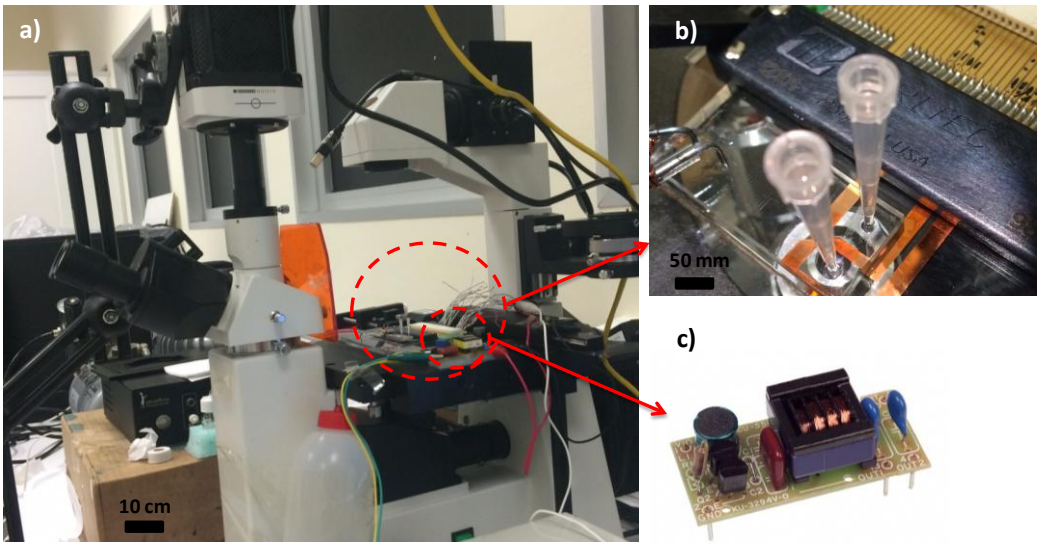

Figure 5. 8. a) 2D DEP set-up. b) Close-up view of 2D DEP device. c) CXA-M10L-L DC to AC inverter.

Droplet sorting depends on different factors ; radius of the droplet, dielectric permittivity and conductivity of medium and droplet, voltage and frequency of electric field according to dielectrophoretic force formula (Equation 6.1). Also droplet speed is important, since it determines the time the droplet is subjected to the electric field. In our experiments, voltage and frequency of the electric field is fixed due to DC to AC inverter. Therefore, to accomplish sorting both using 2D and 3D DEP devices we changed pressure of the inlets that feed liquids for understanding the affect of droplet size and speed on droplet sorting.

In order to understand droplet behavior, the Clausius-Mossotti factor calculation was done for varying conductivity and frequency. For verification of the results, 4,45M NaCl (table salt) water solution was used as dispersed phase. This solution is saturated solution, adding more salt does not change the amount of dissolved salt in water and causes precipitation. 2D DEP devices were used to perform experiments since they are similar to DEP electrodes on a printed circuit board in terms of aspect ratio. Droplet behavior, whether it is inclined to the electrodes, were observed using a high speed camera.

For droplet sorting experiments, droplets were observed under no electric field through microscope. We waited system to become stable, i.e until droplets go to the channels in equal number, one up one down. Potential difference was applied to upper and ground electrode pairs and also lower and ground electrodes to direct droplets to upper and lower channel, respectively. Since the conductivity of dispersed phase is much more than continuous phase, we expect droplets to experience pDEP. For instance, when upper electrode were energized, we statistically found the percentage of droplets going to the upper channel. After voltage was switched off, we verified whether the system became stable.

5.5 Results

In order to characterize 2D coplanar and 3D EGaIn electrodes, we took videos at varying droplet sizes and speeds. The results can be seen in in Table 5.1. As can be seen from Table 5.1, plug like droplets is not sorted, although their speed is on the order of μm/sec, for both 2D coplanar and 3D EGaIn electrodes. Smaller droplets are sorted more likely than bigger droplets. Since videos are taken by normal camera, it is not possible to detect droplet speed and size for smallest droplets at high speeds due to spectroscopic effect. However, smallest droplets is not sorted at high speeds because they do not find time to change their charge orientation at these speeds. Also, droplet sorting with 3D electrodes

are slightly better than with 2D electrodes. Figure 5.3 shows on-demand droplet sorting using 3D EGaIn DEP electrodes.

Table 5.1. Droplet sorting efficiency with respect to droplet speed, droplet size and electrode type.

Electrode type	**Droplet diameter/length**	**Droplet speed**	**Efficiency**
2D coplanar	100 µm (diameter)	4 mm/sec	%70
2D coplanar	150 µm (length)	37 µm/sec	Can not be sorted
3D EGaIn	75 µm (diameter)	3 mm/sec	%100
3D EGaIn	125 µm (length)	16 µm/sec	Can not be sorted.

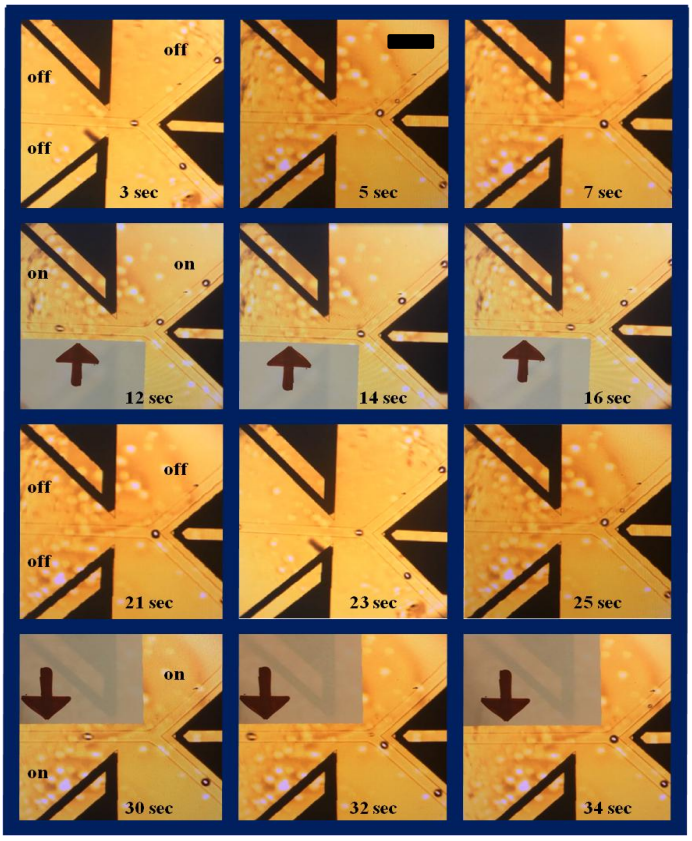

Figure 5.9. On-demand droplet sorting using 3D electrodes. When the AC signal is off, droplets go either channel. When AC signal is given to the upper electrodes, droplets are sorted towards the upper channel, vice versa. Scale bar is 500 µm.

In order to understand DI water droplet behavior in a silicone oil, we calculated real part of Clausius-Mossotti factor at varying frequencies and droplet conductivities using Equation 5.24. As can be seen in Figure 5.10, a DI droplet (0,0002 S/m) is affected by positive dielectrophoresis and pushed towards the energized electrodes. Increasing conductivity of DI water droplet does not change this behavior.

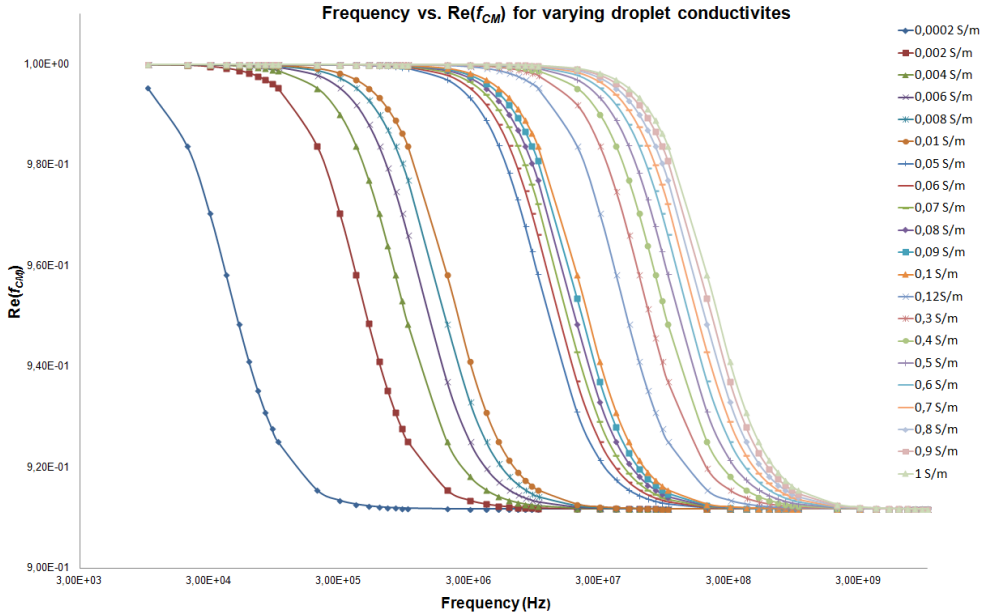

Figure 5. 10. Frequency dependent real part of Clausius-Mossotti factor calculation at varying droplet conductivities.

In order to observe droplet behavior, whether it is inclined to the electrodes when salt is added to the water, we used 2D DEP devices. We observed that, droplets that are generated using saturated salt water solution are inclined to the channel walls after voltage electrodes and before bifurcation. Therefore, increasing conductivity of the dispersed phase ease droplet sorting.

5.6 Conclusion

In this chapter, we demonstrated microdroplet sorting using both 2D coplanar and 3D EGaIn electrodes. 3D EGaIn electrodes were fabricated without a need of clean room unlike 2D coplanar electrodes. CXA-M10L-L DC to AC inverter is an asset to eliminate a signal generator for DEP applications. Therefore, this small footprint inverter is a useful tool to achieve portable microfluidic systems. A water droplet in a silicone oil always sees positive dielectrophoresis according to Clausius-Mossotti calculation due to stark conductivity change from oil to water. We verified that the increasing conductivity of a droplet, increases the DEP force. For a better sorting, droplets should be inclined to the voltage electrode that is energized before the bifurcation. Therefore, the diameter of the droplet should be smaller than channel width. Both 2D and 3D electrodes can be used for droplet sorting depending on the application.

Chapter 6

Droplet Detection and Sorting on a Printed Circuit Board (PCB)

6.1 Introduction

Nowadays, printed circuit boards (PCBs) are used in nearly all of the electronic devices. A PCB provides mechanical support and electrical connection for electronic components using etched copper that is coated on a non-conductive substrate, FR4 (flame retardant 4). PCB provides several advantages as,

- easy and automated manufacture,
- decreased footprint of a circuit,
- being cheaper with respect to other methods,
- increased signal to noise ratio (SNR) for electrical sensors that is mounted on it.

As explained in Chapter 4, micron-sized electrodes were manufactured as capacitive sensors on a standard glass slide underneath microchannels coated with passivation layer in order to detect droplet content. These capacitive sensors were fabricated using photolithography and physical vapor deposition method (PVD), therefore a clean room was needed. The pin that provides

connection between contact pads and the coaxial cable experience ambient conditions, therefore the capacitance signal is prone to noise. The setup is still bulky, although the sensitivity of the system is increased with respect to other capacitive sensing systems in the literature [2], [53].

Eventhough the microdroplet based microfluidic systems are introduced as lab-on-a-chip systems, they really are not [54]. The connection between microchannels and the outer world needs precision tips, tubing, pumps (syringe or pressure), detection systems (fluorescence microscopy, lasers, photomultiplier tubes etc [51]) et cetera. Therefore, for realizing a truly hand-held lab-on-chip system, all the bulky components should be replaced with small foot print components, preferably integrated circuits (ICs).

In the literature, there are different studies that use PCB as a detection system for chemical identification, cell detection, trapping and lysis, droplet detection, DNA amplification and virus detection, air bubble detection [55]–[57], [3], [58], [59]. Although PCB is used in the study, it still requires a clean-room or an optical detection system. Kemna *et al.* and Ameri *et al.* deposited electrodes on a glass slide and then connect electrode pads to a PCB via wire bonding. Guijt *et al.* detects different chemical in a continuous flow microfluidic system not in a droplet based system with a painful fabrication process. Although, Li *et al.*'s study is quite impressive in terms of compactness, they detect droplets on the order picoFarad (pF). Prakash *et al.* need an additional optical detection system which is far off becoming a hand-held system.

For dielectrophoretic studies in which PCB used as a platform, the main aim is to provide contact between electronic components and the electrodes that are patterned on glass slides [60]–[65]. In all aforementioned studies, continuous flow is used to separate cells or particles. Even in some of the studies, optical detection is used additional to a PCB [65], [66]. Although they add literature dielectrophoresis based cell/particle sorting systems, all of the systems for

experimentation are quite bulky. To the best of our knowledge, droplet-based dielectrophoretic sorting system on a printed circuit board has never been demonstrated in the literature.

In order to realize a hand-held microdroplet-based microfluidic system, we transferred all the electrical connections and electrodes onto a PCB which can be mounted on Arduino as a shield. On top of a PCB, a microchannel is placed in order to detect and sort the droplets. The microchannel is bonded to 20 μm PDMS membrane in order to enhance sensitivity of the system. Then, it is fixated to the PCB using laser cutted plexiglass and nuts. This method enables usage of the system repeatedly by only changing microchannels, i.e cartridges. Moreover, most of the bulky components are eliminated and footprint of the circuit is decreased.

6.2 Comsol Simulations

Under an AC field, time-averaged DEP force for a spherical particle is

$$< F_{DEP} >= 2 * \pi * \varepsilon_m * \varepsilon_0 * r^3 * Re(f_{CM}) \nabla |E|^2 \qquad (6.1)$$

As can be seen from Equation 6.1, gradient of electric field square is directly proportional to dielectrophoretic force. At an optimum condition, this force ensures droplet movement, therefore droplet sorting, in up or down direction at a bifurcation. For deciding channel and DEP electrode dimensions and understanding droplet behavior at a proximity of the bifurcation, we calculated gradient of electric field square at different directions and conditions using COMSOL.

Electric field is a vectoral field. A vectoral field is a function $\vec{F}$ that assings each point (x,y,z) in space to a vector $\vec{F}$(x,y,z). This field represents each point both by a magnitude and direction, but a scalar field is defined only by

magnitude. Gradient is a vector field being partial derivatives of a scalar field function, measures the rate and direction of a change in a scalar field. Gradient of a scalar field, f, is calculated making dot product of the field and the gradient.

A vector field, $\vec{F}$(x,y,z), is represented using the following notation for three dimensional space,

$$\vec{F}(x,y,z) = P(x,y,z)\vec{x} + Q(x,y,z)\vec{y} + R(x,y,z)\vec{z} \tag{6.2}$$

where P,Q and R are scalar functions and $\vec{\mathrm{x}}$, $\vec{\mathrm{y}}$, and $\vec{\mathrm{z}}$ are unit vectors. In three dimension, gradient of a scalar field, f, is,

$$\nabla f = \frac{\partial f}{\partial x}\,\vec{\mathrm{x}} + \frac{\partial f}{\partial y}\,\vec{\mathrm{y}} + \frac{\partial f}{\partial z}\,\vec{\mathrm{z}} \tag{6.3}$$

Electric field in three dimension is,

$$\vec{E}(x,y) = E_x\vec{x} + E_y\vec{y} + E_z\vec{z} \tag{6.4}$$

Electric field amplitude and its square is,

$$\left|\vec{E}\right| = \sqrt{E_x^2 + E_y^2 + E_z^2} \tag{6.5.a}$$

$$\left|\vec{E}\right|^2 = E_x^2 + E_y^2 + E_z^2 \tag{6.5.b}$$

Gradient of electric field square is,

$$\nabla\left|\vec{E}\right|^2 = \left(\frac{\partial}{\partial x}\,\vec{\mathrm{x}} + \frac{\partial}{\partial y}\,\vec{\mathrm{y}} + \frac{\partial}{\partial z}\,\vec{\mathrm{z}}\right)\cdot\left(E_x^2 + E_y^2 + E_z^2\right) \tag{6.6}$$

$$\nabla\left|\vec{E}\right|^2 = \frac{\partial E_x^2}{\partial x}\,\vec{\mathrm{x}} + \frac{\partial E_y^2}{\partial x}\,\vec{\mathrm{x}} + \frac{\partial E_z^2}{\partial x}\,\vec{\mathrm{x}} + \frac{\partial E_x^2}{\partial y}\,\vec{\mathrm{y}} + \frac{\partial E_y^2}{\partial y}\,\vec{\mathrm{y}} + \frac{\partial E_z^2}{\partial y}\,\vec{\mathrm{y}} + \frac{\partial E_x^2}{\partial z}\,\vec{\mathrm{z}} + \frac{\partial E_y^2}{\partial z}\,\vec{\mathrm{z}} + \frac{\partial E_z^2}{\partial z}\,\vec{\mathrm{z}} \quad (6.7)$$

$$\nabla\left|\vec{E}\right|^2 = \left(\frac{\partial E_x^2}{\partial x} + \frac{\partial E_y^2}{\partial x} + \frac{\partial E_z^2}{\partial x}\right)\vec{\mathrm{x}} + \left(\frac{\partial E_x^2}{\partial y} + \frac{\partial E_y^2}{\partial y} + \frac{\partial E_z^2}{\partial y}\right)\vec{\mathrm{y}} + \left(\frac{\partial E_x^2}{\partial z} + \frac{\partial E_y^2}{\partial z} + \frac{\partial E_z^2}{\partial z}\right)\vec{\mathrm{z}} \quad (6.8)$$

$$\nabla\left|\vec{E}\right|^2 = \frac{\partial}{\partial x}\left(E_x^2 + E_y^2 + E_z^2\right)\vec{\mathrm{x}} + \frac{\partial}{\partial y}\left(E_x^2 + E_y^2 + E_z^2\right)\vec{\mathrm{y}} + \frac{\partial}{\partial z}\left(E_x^2 + E_y^2 + E_z^2\right)\vec{\mathrm{z}} \quad (6.9)$$

In COMSOL Equation 6.9 can be written as

$$(d(es.Ex\text{^}2 + es.Ey\text{^}2 + es.Ez\text{^}2), x) + (d(es.Ex\text{^}2 + es.Ey\text{^}2 + es.Ez\text{^}2), y) + (d(es.Ex\text{^}2 + es.Ey\text{^}2 + es.Ez\text{^}2), z) \quad (6.10)$$

for three dimensional space where *es.Ex* is the notation for normalized x component of the electric field in x direction, *es.Ex^2* is square of x component of the electric field in x direction, $(d(A), x)$ is for calculating derivative of function A with respect to x. This is also valid for other directions.

In two dimension, gradient of electric field square is,

$$\nabla\left|\vec{E}\right|^2 = \left(\frac{\partial}{\partial x}\,\vec{\mathrm{x}} + \frac{\partial}{\partial y}\,\vec{\mathrm{y}}\right)\cdot\left(E_x^2 + E_y^2\right) \quad (6.11)$$

$$\nabla\left|\vec{E}\right|^2 = \frac{\partial}{\partial x}\left(E_x^2 + E_y^2\right)\vec{\mathrm{x}} + \frac{\partial}{\partial y}\left(E_x^2 + E_y^2\right) \quad (6.12)$$

In COMSOL Equation 6.12 can be written as

$$(d(es.Ex\text{^}2 + es.Ey\text{^}2), x\ ) + (d(es.Ex\text{^}2 + es.Ey\text{^}2), y) \qquad (6.13)$$

Since y component of the dielectrophoretic force is essential for a droplet being inclined to either upside or downside channel, we calculated only

$$(d(es.Ex\text{^}2 + es.Ey\text{^}2 + es.Ez\text{^}2), y) \text{ for 3D space,} \qquad (6.14)$$

$$(d(es.Ex\text{^}2 + es.Ey\text{^}2), y) \qquad \text{for 2D space,} \qquad (6.15)$$

The resulting unit for calculating electric field square gradient is $\frac{V^2}{m^3}$ or $\frac{kg^2}{s^6}\frac{m}{A^6}$ where V is volt, m is meter, kg is kilogram, s is second, and A is Ampere.

For finding the DEP electrode configuration that provides the highest value in terms of electric field square gradient, we simulated different electrode shapes, orientations and locations in 2D space using Equation 6.15. For this purpose, ground electrode shape and location are fixed, whereas voltage electrode shape, orientation and location are changed. The length of the line in which the force is calculated on is kept constant between different designs. The information about electrodes are given in Table 6.2, Table 6.3 and Table 6.4.

In order to calculate dielectrophoretic force in y direction at different heights, 2 μm and 80 μm height electrodes used in COMSOL simulation (Figure 6.1 & Figure 6.2). The shape of both electrode type and the distance between voltage and ground electrodes are exactly same. Although the thickness of 2D electrodes are 220 nm, for ease of calculation, 2 μm electrodes are used (Figure 6.1). This calculation is useful for understanding the relation of dielectrophoretic force to height of electrodes. In terms of aspect ratio, PCB electrodes are alike 2D DEP electrodes on glass slides. Therefore, the calculation provides information about PCB electrodes. The distance between voltage electrode tip and the line in which the force is calculated is 75 μm.

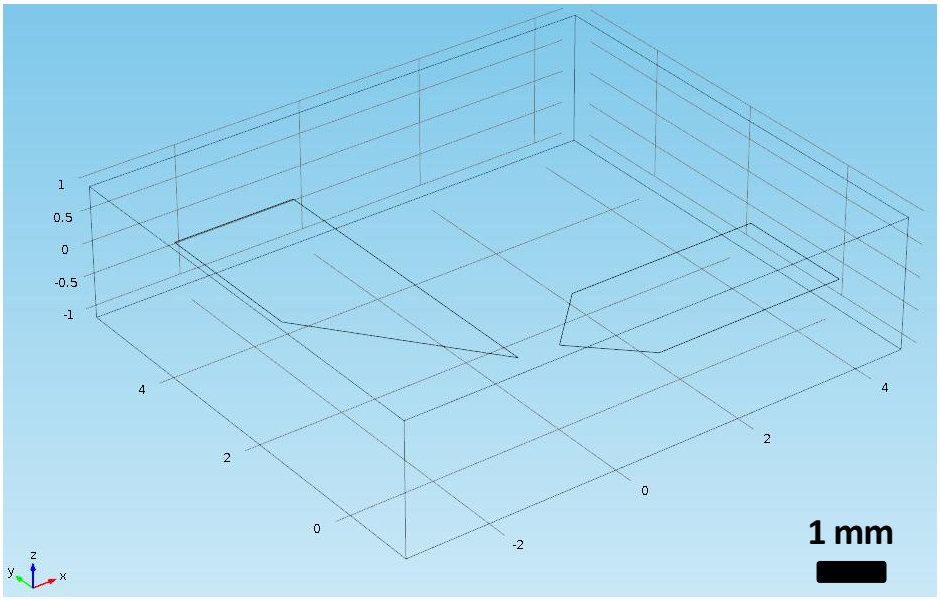

Figure 6. 1. COMSOL snapshot of DEP electrodes that have 2 µm height in z direction.

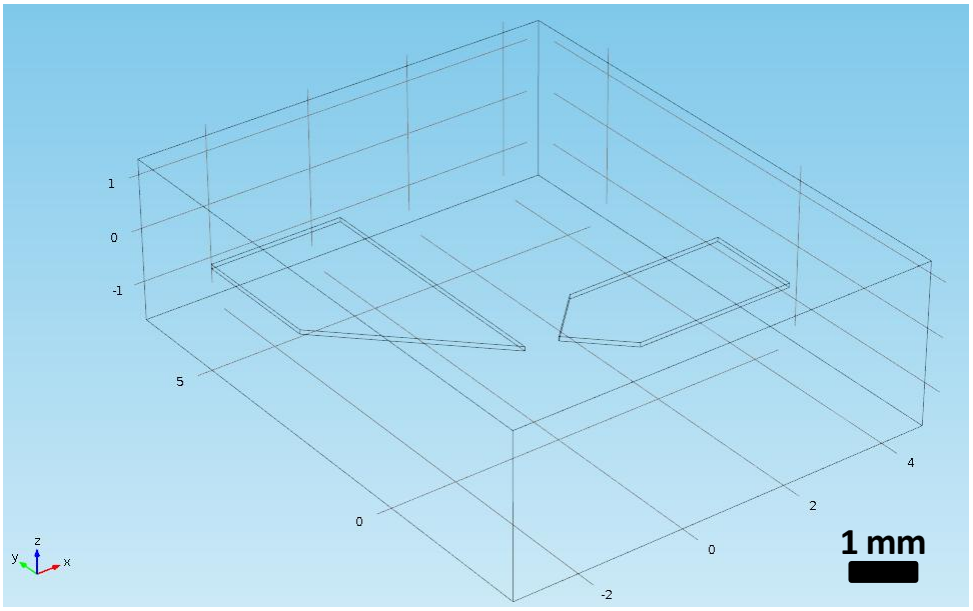

Figure 6. 2. COMSOL snapshot of DEP electrodes that have 80 µm height in z direction.

In the literature, DEP electrodes where both voltage and ground electrodes placed same side of the microchannels (denoted as side electrodes) were used for sorting applications (Figure 6.3) [67]. In order to understand the difference

between side electrodes and the electrodes that are placed with an 60° angle (denoted as our electrodes) (Figure 6.4), we compared the DEP force in y direction on the same line for both side and our electrodes. The electrode thickness is 60 µm since this is the thickness of PCB electrodes. The distance between voltage electrode tip and the line in which the force is calculated is 75 µm.

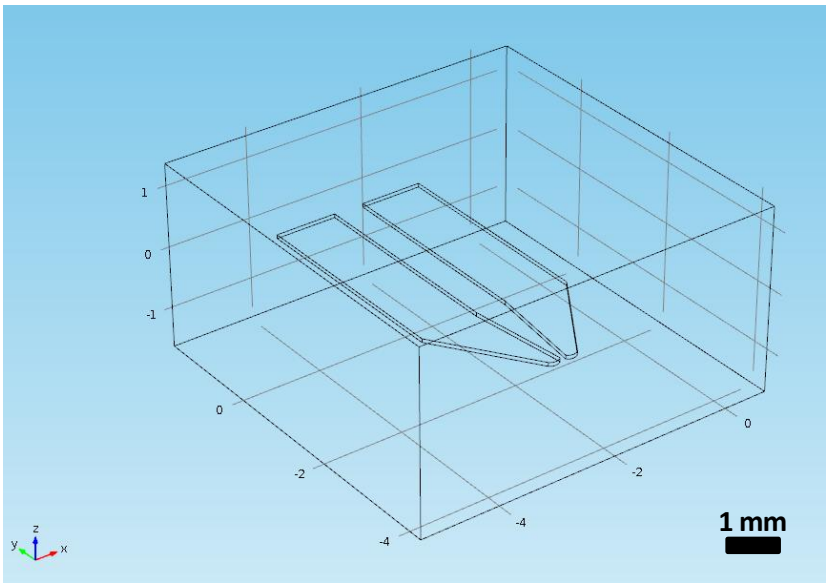

Figure 6. 3. COMSOL snapshot of side electrodes.

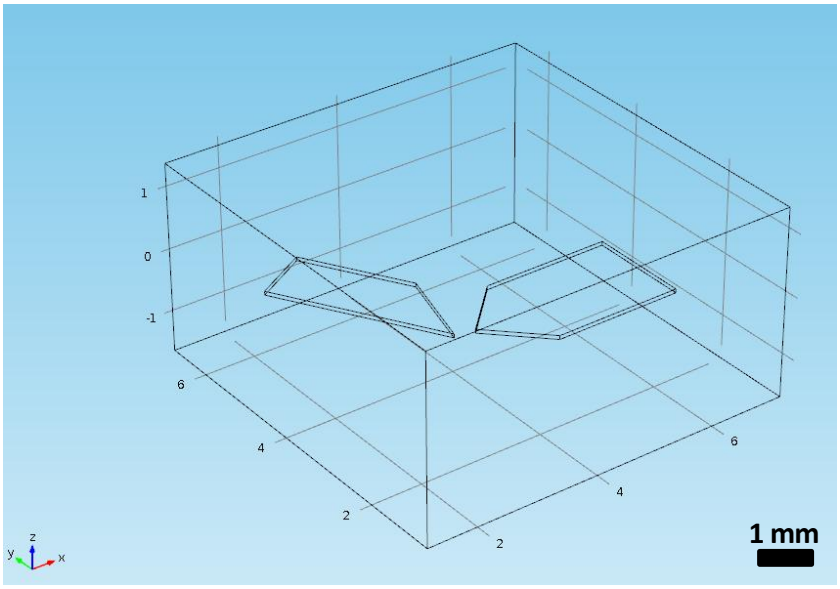

Figure 6. 4. COMSOL snapshot of our electrodes.

In Chapter 5, we state that space is needed for a droplet to incline before the bifurcation. However, side electrodes are placed quite close to the microchannels in the literature [67]. Therefore, sorting droplets in a microchannel using side electrodes becomes a design problem requiring optimization of channel width. For this purpose, we calculated DEP force changing channel width, therefore the distance between the DEP electrodes and the calculation line. The lines are placed at 65 µm , 75 µm and 500 µm. The thickness of the electrodes is 60 µm.

Both aforementioned calculations are done in 3D space in an air box using stationary solver. 5V DC applied to the voltage electrode. The line in which the force is calculated is placed at different z heights to understand the effect of the distance between DEP electrodes and microchannel on DEP force.

6.3 Design and Fabrication

In order to realize a truly portable integrated microfluidic system, we designed a cartridge like structure that is mounted on a printed circuit board. This printed

circuit board replaces coplanar and DEP electrodes that are deposited on glass slides. Also, brings capacitance to digital converter (AD7746), DC to AC inverter and Arduino together in a small footprint. By aligning PDMS microchannels to electrodes on a printed circuit board, this set-up becomes a hand-held device with a cartridge.

For making a PDMS cartridge that contains microchannels, different materials were considered as substrate instead of glass slide. We found that the distance between coplanar electrodes and the microchannel (thickness of the passivation layer) affect the signal amplitude and the resolution of the system as explained in Chapter 4. Therefore, a thin but durable substrate was needed. We tried different materials such as polyimide film, tape, stretch film, and double sided tape. Although, thickness of these materials are not above 30 μm, they are still so thick for high resolution capacitive detection. Also, PDMS does not make proper bonds with these materials despite oxygen plasma treatment. Eventhough the substrates and PDMS stay together after oxygen plasma, applying pressure to microchannels for generating droplets destructs devices and causes leakage.

As substrate, both 100 μm thick glass slide and spin coated PDMS were used. Glass slide is highly durable with respect to spin coated PDMS, but it is thick. Unlike glass slide, it is possible to adjust PDMS thickness down to 8 μm when it is spin coated. In order to use PDMS as substrate, we spin coated PDMS on a SU-8 2005 coated Si wafer, Si wafer and an aluminum pan at 2000 rpm. Amongst them only aluminum pan is a suitable candidate for generating thin PDMS membranes. Therefore, PDMS was spin coated on an aluminum pan and put onto hot plate at 100 ℃ for half an hour. After bonding microchannels to PDMS coatings, microchannels were peeled off without any damage. Until 150 mbar pressure, PDMS membrane did not leak any liquid. However, higher pressure was needed for droplet sorting experiments. Therefore, we spin coated 500 nm 495PMMA A2 resist (MicroChem) on PDMS membrane to prevent leakage.

For droplet detection experiments on a printed circuit board, we used a simple T-junction microchannel. Microchannels were fabricated using standard soft lithography methods as explained in Chapter 3. The width and height of the channel were measured as 300 μm and 80 μm, respectively. We designed coplanar electrodes at varying widths and gaps using Proteus ARES software. The PCB that contains coplanar electrodes was manufactured using ProtoMat PCB manufacturing apparatus on a two layer substrate. This substrate composed of FR-4 (flame retardant 4) insulation layer and a thin copper foil laminated on top of FR-4. The machine forms electrodes by scratching copper with a laser. The T-junction microchannels were bonded to both 100 μm glass slides and 20 μm PDMS membrane to compare capacitive signal amplitudes (Figure 6.1). The bonding recipe is given in Chapter 3.

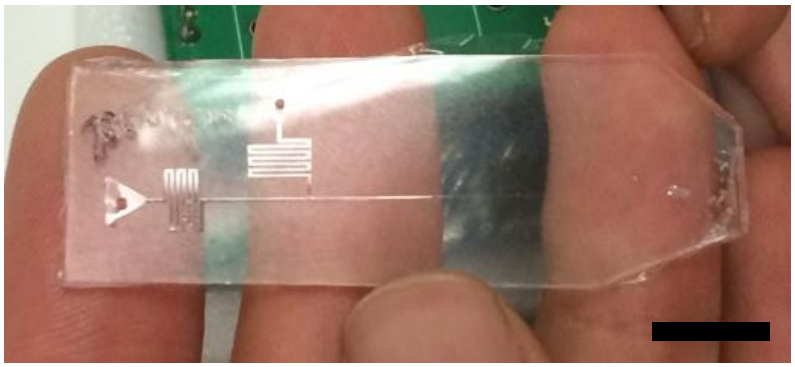

Figure 6.5. T-junction microchannel bonded to 20 μm PDMS membrane. Scale bar is 1 cm.

We designed three different DEP electrodes. In the first DEP electrode design, voltage electrodes consist of 4 sharp edges. We believed that increasing sharp edges before bifurcation increases DEP force in y direction (Design 1). However, this was proved wrong after COMSOL simulations were ran. After running COMSOL simulations, we found that voltage electrode with one sharp edge at an angle of 60° with respect to microchannel gave the highest DEP force in y direction. We designed our DEP electrodes accordingly (Design 2).

As explained above, we compared the DEP force in y direction for both side electrodes and electrodes placed with an 60° angle. Since the force was calculated higher for side electrodes, we designed and manufactured these electrodes (Design 3). All of the fabricated on PCB DEP electrodes are given in Figure 6.6. These designs were manufactured in China in order to have higher resolution (less than 75 µm).

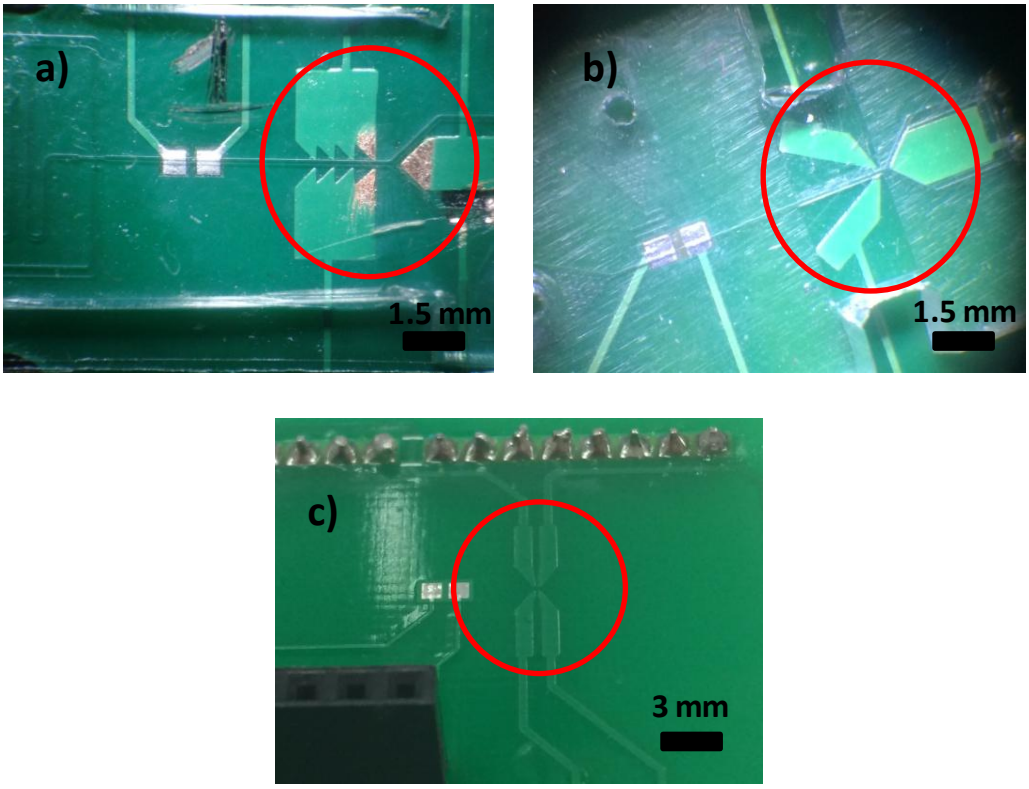

Figure 6. 6. Three different on-PCB DEP electrodes. a) Design 1, b) Design 2, c) Design 3.

Since the increasing distance between electrode tips (voltage and ground) decreases the DEP force, the microchannel width was limited to 150 µm when Design 1 and Design 2 of DEP electrodes were used. For DEP sorting, we designed two different microchannels. The height of both microchannels is 80 µm. A T- junction was designed to generate droplets for both designs. Since the thickness of the copper traces on PCB is 60 µm and the DEP force diminishes in z direction, rectangle channels were designed for DEP electrodes to level

bottom of microchannels to bottom of traces. In order to equate channel resistance after bifurcation, both channel outlets were opened to one reservoir (Design 1). Channel width expands from 40 µm to 90 µm after T-junction. After bifurcation, channel width increases to 150 µm. The reason for expanding channels was to create room for droplets to incline proper direction before the bifurcation. However, this design did not work for generating droplets with diameter less than one third of the channel width because one reservoir as an outlet disrupts the system dynamics. As a result, droplets always inclined one channel. Also, the droplets did not align through the centerline of the microchannel after T-junction. Moreover, increased speed of droplets did not enable proper sorting. To overcome this problem, we designed another microchannel with two outlets and added side junctions. One usage of side junctions was to decrease droplet speed by sucking silicone oil from the main channel. Another usage of side junctions was to align droplet through the centerline of the microchannel and increase the distance between consecutive droplets by driving silicone oil to main channels. However, either usage of side junctions did not work. The reason for generating droplets using a T-junction instead of a flow focusing device was to decrease pressure level driven to the microchannel since higher pressure causes dripping of liquids from PDMS membrane. The dripping problem was overcame by spin coating PMMA on PDMS membrane. Therefore, aforementioned flow focusing device was used to generate droplets.

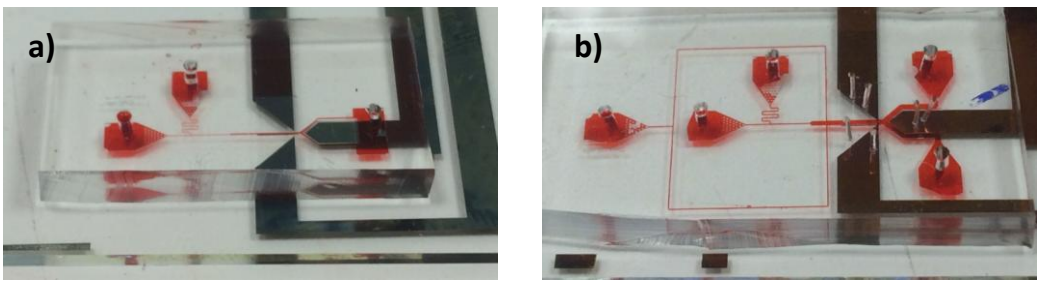

Figure 6. 7. Both microchannel types were designed for on PCB droplet sorting experiments. a) Design 1, b) Design 2

The PCB for droplet sensing and sorting designed as an Arduino shield (Figure 6.8). It provides connections between AD7746 capacitive to digital inverter, Arduino and coplanar electrodes. Also, DC to AC inverter, DEP electrodes and manual switching mechanism were placed onto PCB. The microfluidic channel were placed onto coplanar electrodes and in proximity of DEP electrodes. After placing microfluidic channel, it was fixed through laser cutted plexiglass and nuts. For this purpose, holes were drilled onto PCB using a dremel.

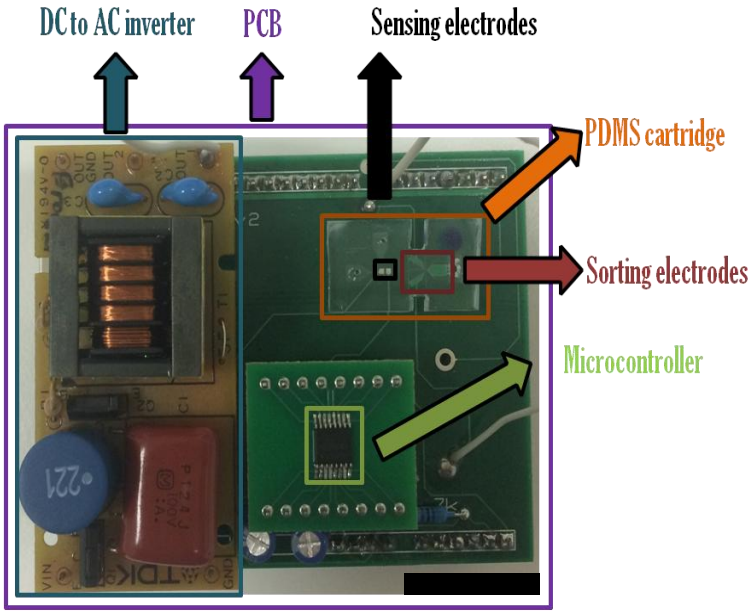

Figure 6.8. The portable system photograph. This system includes AD7746 capacitance-to-digital converter, DC to AC inverter, Arduino Duemilanove, droplet sensing electrodes, DEP electrodes and microchannel. Scale bar is 1 cm.

6.4 Experimental Procedure

For proof-of-concept droplet detection experiments, PCB that is shown in Figure 6.9 was used. Droplets were generated using a T-junction device and pressure pump. 50 mPa s viscosity silicone oil and DI water were used as continuous and dispersed phase respectively. AD7746 was connected to Arduino through BNC (Bayonet Neill–Concelman) connectors and welded on

an Arduino shield. Coaxial cables provide connection between coplanar electrodes and electronic set-up. These cables carry the signal with minimum noise interference. Capacitance signal change due to dielectric permittivity contrast between droplet and the surrounding medium were displayed through LabView interface. 100 µm glass slide bonded T-junction microchannels were used while characterizing different coplanar electrodes (Figure 6.9). The capacitance signal was recorded for 50 droplets. These results were averaged. Coplanar electrodes that gave the highest signal amplitude were chosen for further experiments with PDMS membrane bonded T-junction microchannels. For membrane experiments, capacitance signal was recorded for 10 droplets. The results were averaged. A load was put onto microchannels to prevent kinking of PDMS.

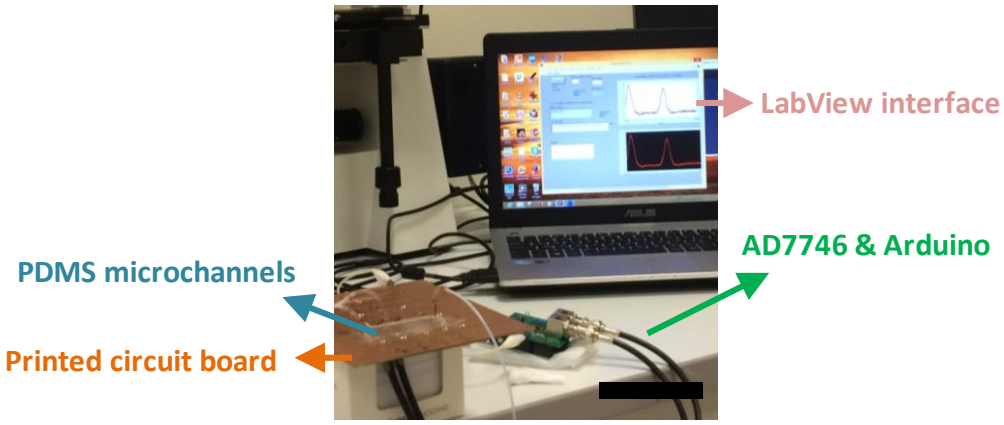

Figure 6.9. On-PCB droplet detection set-up. T-junction microchannels that have 300 µm width and 80 µm height was used. Scale bar is 20 cm.

Droplet sorting experiments were conducted using two different DEP electrode type (Design 1 and Design 2)(Figure 6.6).The system photograph is shown in Figure 6.8. Two type of T-junction devices (Design 1 and Design 2) were used to generate droplets (Figure 6.7). 50 mPa s viscosity silicone oil and DI water were driven to channels using a pressure pump. As explained in Section 6.3, DC to AC inverter and DEP electrodes were welded on an Arduino shield. DC to AC inverter transforms 12 V DC voltage to 31 kHz frequency and 1200 V AC signal. 12 V DC was given to the inverter through DC power supply.

Microchannels bonded to 20 μm PDMS membrane were placed onto PCB and fixed with plexiglass and nuts. The pressure of inlets were changed in order to adjust droplet size and speed.

Under no electric field, droplet behavior was observed through 3D microscope. Until the system became stable, droplets go either channel in equal number, we did not apply voltage. In order to direct droplets upper and lower channels, potential difference was applied to upper and ground electrodes and also lower and ground electrodes channel, respectively. A manual switching mechanism was used to apply potential difference.

6.5 Results

6.5.1 On-PCB droplet content detection

On-PCB droplet detection experiments were done using specified electrodes in Table 6.1. 100 μm glass slide is bonded to 300 μm width T-junction to generate droplets. As can be seen from Table 6.1, increasing electrode width does not necessarily increase capacitance signal amplitude. These are preliminary results to show proof-of-concept. We showed that, coplanar PCB electrodes can be used for droplet detection experiments without depositing electrodes on glass slides.

Table 6. 1. Capacitance change results (ΔC) when a DI droplet in silicone oil passes through PCB electrodes. 100 μm thick glass slide is bonded to microchannels. Devices 1 to 13 are square electrodes and devices 14 to 16 are rectangular electrodes. Capacitance signal amplitudes averaged over 50 droplets for each device.

Device Numbers	Electrode width(μm)	Electrode gap (2a) (μm)	Capacitance change (fF)	Standard deviation
Device 1	762	275	14,598	0,87
Device 2	762	375	13,086	0,69
Device 3	1016	275	14,515	0,93
Device 4	1016	375	14,034	0,69
Device 5	1270	125	18,104	1,22
Device 6	1270	275	18,263	1,17
Device 7	1270	375	21,757	1,5
Device 8	1524	125	21,943	1,47
Device 9	1524	375	18,063	1,76
Device 10	1778	275	21,604	1,42
Device 11	1778	375	18,204	1,39
Device 12	2032	375	14,619	0,68
Device 13	2032	475	10,349	0,68
Device 14	1524*2032	175	22,81	1,08
Device 15	1524*2032	325	22,168	1,33
Device 16	1524*2032	425	20,779	1,81

In order to decrease the distance between coplanar PCB electrodes and the microchannel, 300 μm width T-junction microchannel was bonded to 20 μm PDMS membrane. Device 14 was used during the experiments since this electrode design gave the highest capacitance signal amplitude during the experiments that was done using 100 μm thick glass. Capacitance signal amplitude was recorded and averaged over 10 droplets. Data averaging was done using MATLAB code. The average is 117,7 fF and the standard deviation is 11,7 (Figure 6.10).

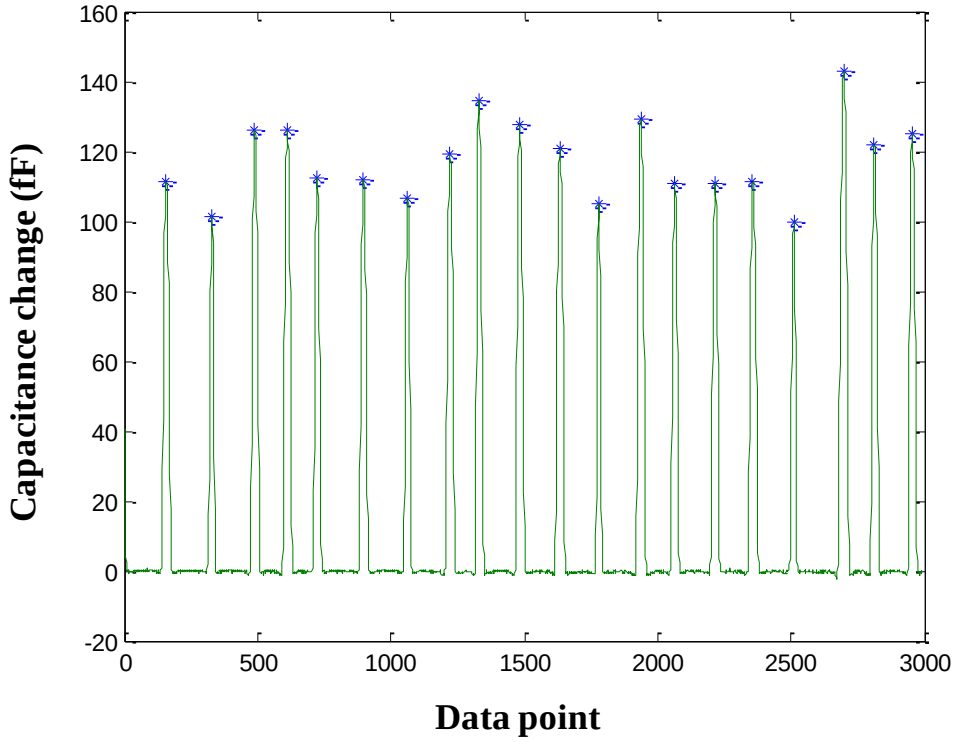

Figure 6.10. Data point versus capacitance signal amplitude graph. The plot was taken using T-junction microchannel bonded with 20 µm PDMS membrane. After collecting data from LabView, the data was processed in MATLAB. Each peak represents a droplet in the plot.

The results in Table 6.1 and Figure 6.10 show that decreasing distance between coplanar electrodes and the microchannel increases capacitance signal amplitude. The same electrode pair gives 22 fF for 100 µm thick substrate and 117 fF for 20 µ substrate. Therefore, using thinner substrate underneath microchannels increases resolution of the system.

6.5.2 COMSOL Simulation results

In order to find the highest value of electric field square gradient different DEP electrode configurations were used for COMSOL simulations in 2D space. For ease of comparison, electrode designs are given in three tables.

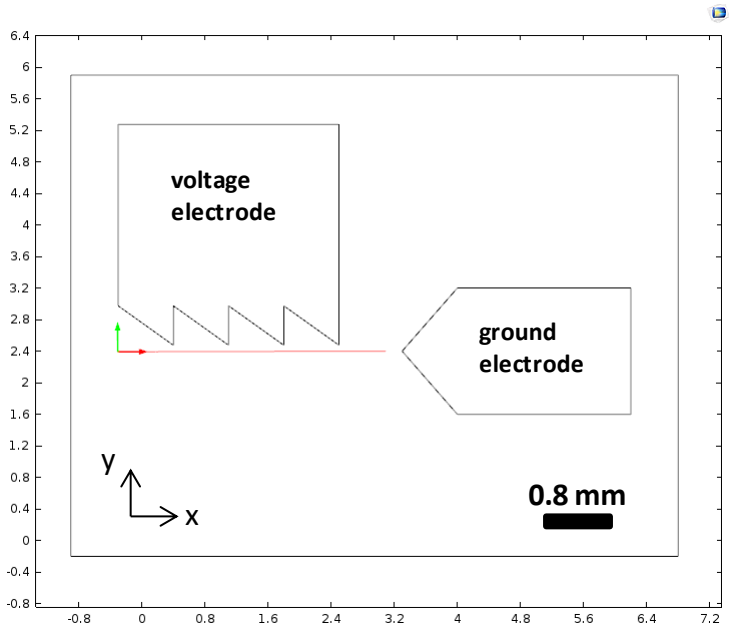

Figure 6. 11. All electrode configurations in Table 6.2 are derivatives of this configuration (Design 1 for DEP electrode).

Table 6.2. Electric field square gradient results when different configurations of PCB DEP electrode Design 1 is used (Figure 6.11).

Electrode x y	**Distance between electrode tips in x direction (µm)**	**Distance between electrode tips in y direction (µm)**	**Electric field square gradient (V^2/m^3)**
Configuration 1	75	700	1,76E + 08
Configuration 2	75	300	5,35E + 08
Configuration 3	1000	300	1,87E + 07
Configuration 4	750	700	1,59E+07

As can be seen in Table 6.2, for same distance between electrode tips in x direction, closer electrodes in y direction give higher result. Also, increasing distance in x direction for equal distance in y direction results in an order of magnitude decrease. Therefore, electrode tips should be designed close to each other in both directions.

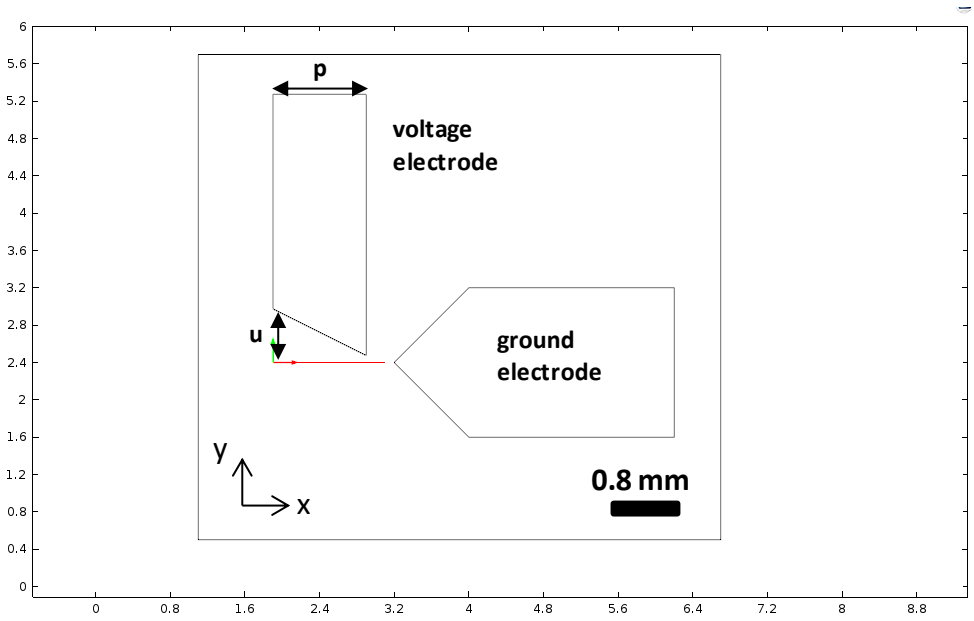

Figure 6. 12. All electrode configurations in Table 6.3 are derivatives of this configuration.

Table 6.3. Electric field square gradient results. In PCB DEP electrode Design 1, there are four sharp edges at voltage electrode. In all of these designs, there is only one sharp edge at voltage electrode (Figure 6.12).

Electrode configuration x ↑ → y	**Distance between electrode tips in x direction (µm)**	**Distance between electrode tips in y direction (µm)**	**Electrode length (p) (µm)**	**The distance determines voltage electrode sharpness (u) (µm)**	**Electric field square gradient (V^2/m^3)**
Configuration 5	75	300	1000	500	4,31E + 08
Configuration 6	100	500	1000	500	1,08E + 08
Configuration 7	100	500	1000	1000	2,16E + 08
Configuration 8	100	500	1000	2000	1,18E + 08
Configuration 9	100	500	2000	1000	1,51E + 08
Configuration 10	75	300	1000	1000	5,13E + 08
Configuration 11	75	300	2000	1000	4,86E + 08

Eventhough the result does not decrease an order of magnitude like in 4 sharp tip voltage electrodes, increasing distance in x direction for equal distance in y direction results in decline. Decreasing electrode length (p) gives higher results. The distance determines voltage electrode sharpness (u) has an optimum value, increasing or decreasing it too much results in decline.

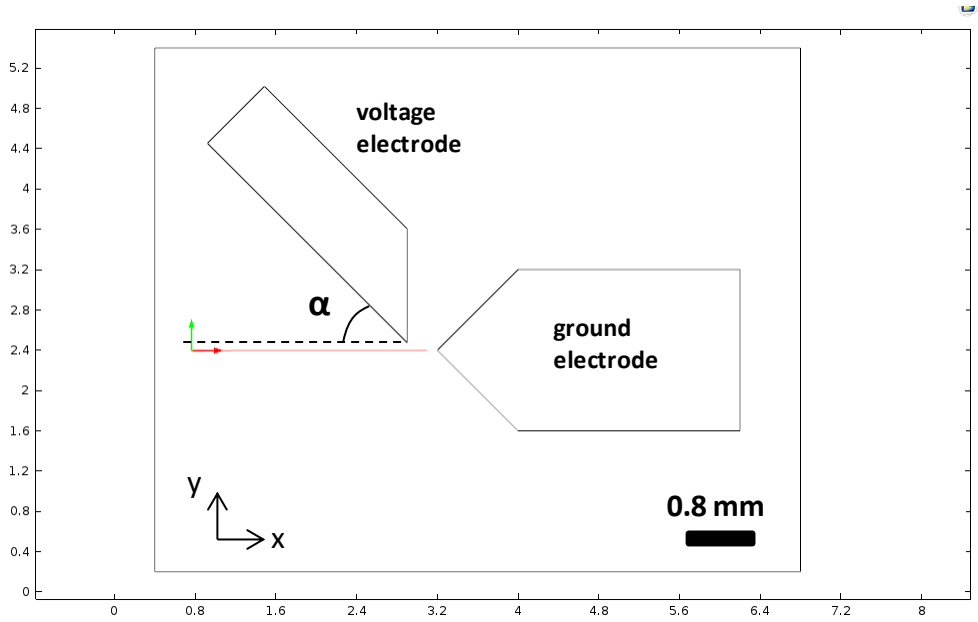

Figure 6. 13. All electrode configurations in Table 6.4 are derivatives of this configuration.

Table 6.4. Electric field square gradient results. PCB DEP electrode Design 2 is fabricated version of Configuration 15. Electrode length (p) is 800 µm and the distance determines the voltage electrode sharpness (u) is 800 µm for all configurations.

Electrode configuration 	Distance between electrode tips in x direction (µm)	Distance between electrode tips in y direction (µm)	Voltage electrode angle (α) with respect to x axis	Electric field square gradient (V^2/m^3)
Configuration 12	75	300	0°	4,80E + 08
Configuration 13	100	500	0°	2,06E + 08
Configuration 14	75	300	45°	5,39E + 08
Configuration 15	**75**	**300**	**60°**	**6,99E + 08**
Configuration 16	100	400	60°	3,98E + 08

Increasing angle with respect to y axis for voltage electrode gives higher results. The electrode Configuration 15 shows the highest result in all electrode configurations. Therefore, this configuration was fabricated on PCB as DEP electrodes Design 2.

In order to understand the relation between the electrode height and dielectrophoretic force, the dielectrophoretic force was calculated for 2 µm and 80 µm height electrodes. The calculation was done in 3D space at different heights in z direction. The results can be seen in Table 6.5.

Table 6.5. Electric field square gradient results calculated through a line in y direction. The distance between the tip of the voltage electrode and the line is 75 µm. The calculation was done by changing line height in z direction. Figure 6.1 & Figure 6.2 show COMSOL snapshots of these electrodes.

Height in z direction	$\nabla\left\|\vec{E}\right\|^2$ for 2 µm height electrodes (1)	$\nabla\left\|\vec{E}\right\|^2$ for 80 µm height electrodes (2)	Ratio of (2) to (1)
1 µm	1,0137E + 08	3,9806E + 08	3,9268
2 µm	1,0164E + 08	3,9966E + 08	3,9321
5 µm	1,0206E + 08	4,0392E + 08	3,9577
10 µm	1,0209E + 08	4,0921E + 08	4,0083
20 µm	1,0049E + 08	4,1115E + 08	4,0915
40 µm	8,4630E + 07	3,4872E + 08	4,1205
80 µm	5,1150E + 07	2,2040E + 08	4,3089
100 µm	4,0130E + 07	2,4745E + 08	6,1662
150 µm	2,1750E + 07	9,8090E + 07	4,5099
250 µm	1,1560E + 07	2,8110E + 07	2,4317
500 µm	2,6900E + 06	4,9100E + 06	1,8253
1000 µm	7,8000E + 05	1,0600E + 06	1,3590

Table 6.5 shows that the increasing distance between the microchannel and the electrodes results in order of magnitude decrease. Therefore it is important to decrease the distance between microchannel and the electrodes. 2 µm height coplanar electrodes are alike PCB DEP electrodes in terms of aspect ratio. Therefore, microchannels should be fixated during the experiments in order to increase DEP force. The ratio of results shows that higher force can be obtained using 80 µm height electrodes (3D electrodes).

Side PCB electrodes and our PCB electrodes were compared using 3D space in COMSOL. We calculated DEP force through a line lies in y direction. The distance between the line and voltage electrode is 75 µm. The calculation was done for 60 µm height PCB electrodes. Table 6.6 demonstrates that side PCB electrodes exert more DEP force than our PCB electrodes at different z heights. Therefore, it is wise to use side DEP electrodes instead of our PCB electrodes.

Table 6.6. Side PCB electrode and our PCB electrode comparison. Electric field square gradient results calculated through a line that lies in y direction. The distance between the tip of the voltage electrode and the line is 75 µm. The calculation was done by changing line height in z direction. The height of electrodes is 60 µm. Figure 6.3 & Figure 6.4 show COMSOL snapshots of these electrodes.

Height in z direction	$\nabla\|\vec{E}\|^2$ **for our electrodes (1)**	$\nabla\|\vec{E}\|^2$ **for side electrodes (2)**	**Ratio of (2) to (1)**
1 µm	5,5566E + 08	1,5836E + 09	2,8499
2 µm	5,6322E + 08	1,6137E + 09	2,8652
5 µm	5,8472E + 08	1,6970E + 09	2,9023
10 µm	6,2000E + 08	1,7235E + 09	2,7798
20 µm	6,9070E + 08	1,6773E + 09	2,4284
40 µm	7,8513E + 08	1,6520E + 09	2,1041
60 µm	7,3319E + 08	1,4901E+09	2,0323
80 µm	6,0298E + 08	1,2301E + 09	2,0400
100 µm	4,0375E + 08	7,7559E + 08	1,9210
150 µm	9,3870E + 07	1,9264E + 08	2,0522
250 µm	2,4420E + 07	6,6170E + 07	2,7097
500 µm	3,0700E + 06	9,6700E + 06	3,1498
1000 µm	9,1000E + 05	6,8000E + 05	0,7473

In order to adjust microchannel width properly, therefore, the distance between the droplet and the voltage electrode tip, we calculated DEP force through a line at different y and z directions. As can be seen Table 6.7, increasing distance between the voltage electrode tip and the droplet center, decreases DEP force. Therefore, channel width was kept at 150 µm.

Table 6.7. DEP force comparison at different y and z for 60 µm height side PCB electrodes (Figure 6.3). Electric field square gradient results calculated through a line that lies in y direction. The distance between the tip of the voltage electrode and the line was varied as 65 µm, 75 µm and 500 µm.

Height in z direction	$\nabla\left\|\vec{E}\right\|^2$ for side electrodes at 65 µm in y direction (1)	$\nabla\left\|\vec{E}\right\|^2$ for side electrodes at 75 µm in y direction (2)	$\nabla\left\|\vec{E}\right\|^2$ for side electrodes at 500 µm in y direction (3)	Ratio of (1) to (2)	Ratio of (2) to (3)
1 µm	2,2307E + 09	1,5836E + 09	5,3383E + 06	1,4086	296,6450
2 µm	2,2521E + 09	1,6137E + 09	5,3464E + 06	1,3956	301,8311
5 µm	2,2480E + 09	1,6970E + 09	5,3702E + 06	1,3247	316,0106
10 µm	2,2274E + 09	1,7235E + 09	5,4019E + 06	1,2924	319,0489
20 µm	2,1689E + 09	1,6773E + 09	5,4396E + 06	1,2931	308,3517
40 µm	2,1375E + 09	1,6520E + 09	5,4728E + 06	1,2939	301,8619
60 µm	1,8882E + 09	1,4901E + 09	5,4316E + 06	1,2672	274,3354
80 µm	1,6508E + 09	1,2301E + 09	5,3013E + 06	1,3420	232,0374
100 µm	1,1388E + 09	7,7559E + 08	5,1769E + 06	1,4682	149,8175
150 µm	2,1645E + 08	1,9264E + 08	4,8945E + 06	1,1236	39,3585
250 µm	7,3490E + 07	6,6170E + 07	4,5270E + 06	1,1106	14,6167
500 µm	9,7300E + 06	9,6700E + 06	2,0780E + 06	1,0062	4,6535
1000 µm	6,9000E + 05	6,8000E + 05	9,1300E + 05	1,0147	0,7448

6.6 Conclusions

In this chapter, we demonstrated that capacitive droplet detection can be done using coplanar PCB electrodes. PDMS membrane is better choice than thin glass slide since it is thinner. Also, it increases the resolution of the system. Since microchannels fixated through only plexiglass and nuts, it is possible to use the system repeatedly by only changing PDMS cartridge. DEP force decreases both in y and z direction, therefore it is important to fixate microchannels onto the PCB. A hand-held device that brings microchannels, capacitive sensing electrodes, and AD7746 is feasible for capacitive droplet detection.

Chapter 7

Conclusions

7.1 Conclusions

Microdroplet based microfluidic systems ensure high-throughput, low cost, and enhanced analytical performance. Although microfluidic systems can be as small as a coin, the detection systems, pumps, microscopes that are needed for experimentation are quite bulky to realize a truly lab-on-a-chip system. In order to accomplish a truly hand-held microfluidic system, all bulky components should be replaced with small foot print components.

For most of the microdroplet based microfluidic systems detection of droplet content is one of the fundamental requirements. In the literature, using optical systems to detect droplets is a common technique due to high detection rates. However, these systems are not portable and scalable. Although, capacitive systems have been used for droplet sensing, they have been lacking the required sensitivity. In order to overcome this problem, we proposed highly sensitive integrated capacitive detection system. The system is portable, scalable and low cost. We achieved to detect droplet content using this system. The system resolution is 3 dielectric permittivity units. We demonstrated that capacitive signal amplitude decreases due to dielectric permittivity decrease in droplet.

The results were verified with a semiconductor parameter analyzer. We verified that minimizing the thickness between the microchannel and coplanar electrodes increases the capacitive signal amplitude. The two analytical models presented in this thesis can be used to determine coplanar electrode design.

We demonstrated microdroplet sorting using both 2D coplanar and 3D EGaIn electrodes. Unlike 2D coplanar electrodes, 3D EGaIn electrodes were fabricated without a need of clean room. We calculated Clausius-Mossotti factor to understand the behaviour of DI water droplet in silicone oil. According to results, a droplet always see positive dielectrophoresis. Moreover, the increasing conductivity of a droplet results in increasing DEP force. The channel width should be larger than droplet diameter for better sorting. CXA-M10L-L DC to AC inverter is a good choice to eliminate signal generator and decrease the footprint of the system.

A hand-held device that brings microchannels, capacitive sensing electrodes, and AD7746 is feasible for capacitive droplet detection. We demonstrated capacitive droplet detection on a printed circuit board. For a cartridge, PDMS membrane is preferrable since it is thinner than a glass slide and increases the system resolution. Microchannels should be fixated to the PCB since DEP force decreases both in y and z direction. The presented system is a useful tool for repetitive experimentation.

We believe that all of the systems presented here is an alternative for bulky and costly bench-top analyzers.

7.2 Future Work

For a truly hand-held microfluidic system, minimized pump and batteries should be integrated to the system. In order to use the system for cell experimentation, DEP sorting on printed circuit board should be accomplished.

We believe adding incubation and storage system will make this system quite useful for biological experimentation. A LabView code can be written to sort droplets on demand after detection of droplets. Moreover, adding another pair of detection electrodes after bifurcation simplify the droplet counting after DEP sorting. Instead of using a microscope to count number of droplets that is sorted, changing AD7746 code for droplet detection simplifies the process.

7.3 Contributions

This thesis resulted in one SCI (science citation index) publication. Also, I presented two posters in one national and one international conference.

[1] **P.K Isgor,** M. Marcali, M. Keser, C. Elbuken, "Microfluidic droplet content detection using integrated capacitive sensors", Sens. Actuators B-Chem., 210 (2015), pp. 669-675

[2] **P.K. Isgor,** M. Marcali, C. Elbuken, "Content detection of microdroplets using capacitive sensors" EMBL Microfluidics 2014, Heidelberg, Germany, 2014

[3] **P.K Isgor**, C. Elbuken, "On-PCB droplet detection and sorting", 2nd International Congress on Biosensors, Izmir, Turkey, 2015

Bibliography

[1] C. Elbuken, T. Glawdel, D. Chan, and C. L. Ren, “Detection of microdroplet size and speed using capacitive sensors,” *Sensors Actuators A Phys.*, vol. 171, no. 2, pp. 55–62, Nov. 2011.

[2] M. F. Abdullah, P. L. Leow, M. A. Abd Razak, and F. K. Che Harun, “On–Chip Droplets Sensing using Capacitive Technique,” *J. Teknol.*, vol. 61, no. 2, Mar. 2013.

[3] J. Li, Y. Wang, E. Dong, and H. Chen, “USB-driven microfluidic chips on printed circuit boards.,” *Lab Chip*, vol. 14, no. 5, pp. 860–4, Mar. 2014.

[4] J. Hong, J. B. Edel, and A. J. deMello, “Micro- and nanofluidic systems for high-throughput biological screening,” *Drug Discov. Today*, vol. 14, no. 3–4, pp. 134–146, Feb. 2009.

[5] E. Carrilho, A. W. Martinez, and G. M. Whitesides, “Understanding wax printing: a simple micropatterning process for paper-based microfluidics.,” *Anal. Chem.*, vol. 81, no. 16, pp. 7091–5, Aug. 2009.

[6] A. W. Martinez, S. T. Phillips, G. M. Whitesides, and E. Carrilho, “Diagnostics for the developing world: microfluidic paper-based analytical devices.,” *Anal. Chem.*, vol. 82, no. 1, pp. 3–10, Jan. 2010.

[7] J. C. McDonald, D. C. Duffy, J. R. Anderson, D. T. Chiu, H. Wu, O. J. Schueller, and G. M. Whitesides, “Fabrication of microfluidic systems in poly(dimethylsiloxane).,” *Electrophoresis*, vol. 21, no. 1, pp. 27–40, Jan. 2000.

[8] E. Y. Erdem, “Microfluidic Reactors for the Controlled Synthesis of Monodisperse Nanoparticles,” University of California Berkeley, 2013.

[9] H. Song, M. R. Bringer, J. D. Tice, C. J. Gerdts, and R. F. Ismagilov, “Experimental test of scaling of mixing by chaotic advection in droplets moving through microfluidic channels.,” *Appl. Phys. Lett.*, vol. 83, no. 12, pp. 4664–4666, Dec. 2003.

[10] H. Song, J. D. Tice, and R. F. Ismagilov, “A microfluidic system for controlling reaction networks in time.,” *Angew. Chem. Int. Ed. Engl.*, vol. 42, no. 7, pp. 768–72, Feb. 2003.

[11] B. Zheng, J. D. Tice, and R. F. Ismagilov, “Formation of droplets of alternating composition in microfluidic channels and applications to indexing of concentrations in droplet-based assays.,” *Anal. Chem.*, vol. 76, no. 17, pp. 4977–82, Sep. 2004.

[12] D. S. Tawfik and A. D. Griffiths, “Man-made cell-like compartments for molecular evolution.,” *Nat. Biotechnol.*, vol. 16, no. 7, pp. 652–6, Jul. 1998.

[13] R. Williams, S. G. Peisajovich, O. J. Miller, S. Magdassi, D. S. Tawfik, and A. D. Griffiths, “Amplification of complex gene libraries by emulsion PCR.,” *Nat. Methods*, vol. 3, no. 7, pp. 545–50, Jul. 2006.

[14] A. D. Griffiths and D. S. Tawfik, “Miniaturising the laboratory in emulsion droplets.,” *Trends Biotechnol.*, vol. 24, no. 9, pp. 395–402, Sep. 2006.

[15] A. Aharoni, A. D. Griffiths, and D. S. Tawfik, “High-throughput screens and selections of enzyme-encoding genes.,” *Curr. Opin. Chem. Biol.*, vol. 9, no. 2, pp. 210–6, Apr. 2005.

[16] T. Thorsen, R. W. Roberts, F. H. Arnold, and S. R. Quake, “Dynamic Pattern Formation in a Vesicle-Generating Microfluidic Device,” *Phys. Rev. Lett.*, vol. 86, no. 18, pp. 4163–4166, Apr. 2001.

[17] S. L. Anna, N. Bontoux, and H. A. Stone, “Formation of dispersions using ‘flow focusing’ in microchannels,” *Appl. Phys. Lett.*, vol. 82, no. 3, p. 364, Jan. 2003.

[18] J. K. Nunes, S. S. H. Tsai, J. Wan, and H. A. Stone, “Dripping and jetting in microfluidic multiphase flows applied to particle and fiber synthesis.,” *J. Phys. D. Appl. Phys.*, vol. 46, no. 11, p. 114002, Mar. 2013.

[19] A. R. Abate, A. Poitzsch, Y. Hwang, J. Lee, J. Czerwinska, and D. A. Weitz, “Impact of inlet channel geometry on microfluidic drop formation,” *Phys. Rev. E*, vol. 80, no. 2, p. 026310, Aug. 2009.

[20] S. Zeng, B. Li, X. Su, J. Qin, and B. Lin, “Microvalve-actuated precise control of individual droplets in microfluidic devices.,” *Lab Chip*, vol. 9, no. 10, pp. 1340–3, May 2009.

[21] A. R. Abate and D. A. Weitz, “Air-bubble-triggered drop formation in microfluidics.,” *Lab Chip*, vol. 11, no. 10, pp. 1713–6, May 2011.

[22] D. Link, S. Anna, D. Weitz, and H. Stone, “Geometrically Mediated Breakup of Drops in Microfluidic Devices,” *Phys. Rev. Lett.*, vol. 92, no. 5, p. 054503, Feb. 2004.

[23] D. R. Link, E. Grasland-Mongrain, A. Duri, F. Sarrazin, Z. Cheng, G. Cristobal, M. Marquez, and D. A. Weitz, “Electric control of droplets in microfluidic devices.,” *Angew. Chem. Int. Ed. Engl.*, vol. 45, no. 16, pp. 2556–60, May 2006.

[24] T. H. Ting, Y. F. Yap, N.-T. Nguyen, T. N. Wong, J. C. K. Chai, and L. Yobas, “Thermally mediated breakup of drops in microchannels,” *Appl. Phys. Lett.*, vol. 89, no. 23, p. 234101, Dec. 2006.

[25] N. Bremond, A. R. Thiam, and J. Bibette, “Decompressing Emulsion Droplets Favors Coalescence,” *Phys. Rev. Lett.*, vol. 100, no. 2, p. 024501, Jan. 2008.

[26] C. N. Baroud, M. R. de Saint Vincent, and J.-P. Delville, “An optical toolbox for total control of droplet microfluidics.,” *Lab Chip*, vol. 7, no. 8, pp. 1029–33, Aug. 2007.

[27] L. M. Fidalgo, C. Abell, and W. T. S. Huck, “Surface-induced droplet fusion in microfluidic devices.,” *Lab Chip*, vol. 7, no. 8, pp. 984–6, Aug. 2007.

[28] X. Niu, S. Gulati, J. B. Edel, and A. J. deMello, “Pillar-induced droplet merging in microfluidic circuits.,” *Lab Chip*, vol. 8, no. 11, pp. 1837–41, Dec. 2008.

[29] M. Zagnoni, C. N. Baroud, and J. M. Cooper, “Electrically initiated upstream coalescence cascade of droplets in a microfluidic flow,” *Phys. Rev. E*, vol. 80, no. 4, p. 046303, Oct. 2009.

[30] G. Binnig and C. F. Quate, “Atomic Force Microscope,” *Phys. Rev. Lett.*, vol. 56, no. 9, pp. 930–933, Mar. 1986.

[31] H. N. Joensson, M. Uhlén, and H. A. Svahn, “Droplet size based separation by deterministic lateral displacement-separating droplets by cell--induced shrinking.,” *Lab Chip*, vol. 11, no. 7, pp. 1305–10, Apr. 2011.

[32] J. Li, Y. Wang, E. Dong, and H. Chen, “USB-driven microfluidic chips on printed circuit boards.,” *Lab Chip*, vol. 14, no. 5, pp. 860–4, Mar. 2014.

[33] J. Z. Chen, A. A. Darhuber, S. M. Troian, and S. Wagner, “Capacitive sensing of droplets for microfluidic devices based on thermocapillary actuation.,” *Lab Chip*, vol. 4, no. 5, pp. 473–80, Oct. 2004.

[34] M. W. den Otter, “Approximate expressions for the capacitance and electrostatic potential of interdigitated electrodes,” *Sensors Actuators A Phys.*, vol. 96, no. 2–3, pp. 140–144, Feb. 2002.

[35] H. Engan, “Excitation of elastic surface waves by spatial harmonics of interdigital transducers,” *IEEE Trans. Electron Devices*, vol. 16, no. 12, pp. 1014–1017, Dec. 1969.

[36] T. Sun, N. G. Green, S. Gawad, and H. Morgan, “Analytical electric field and sensitivity analysis for two microfluidic impedance cytometer designs.,” *IET Nanobiotechnol.*, vol. 1, no. 5, pp. 69–79, Oct. 2007.

[37] P. Garstecki, M. J. Fuerstman, H. A. Stone, and G. M. Whitesides, “Formation of droplets and bubbles in a microfluidic T-junction-scaling and mechanism of break-up.,” *Lab Chip*, vol. 6, no. 3, pp. 437–46, Mar. 2006.

[38] D. C. Duffy, J. C. McDonald, O. J. A. Schueller, and G. M. Whitesides, “Rapid Prototyping of Microfluidic Systems in Poly(dimethylsiloxane),” *Anal. Chem.*, vol. 70, no. 23, pp. 4974–4984, Dec. 1998.

[39] L. L. Sohn, O. A. Saleh, G. R. Facer, A. J. Beavis, R. S. Allan, and D. A. Notterman, “Capacitance cytometry: measuring biological cells one by one.,” *Proc. Natl. Acad. Sci. U. S. A.*, vol. 97, no. 20, pp. 10687–90, Oct. 2000.

[40] T. Sun, D. Holmes, S. Gawad, N. G. Green, and H. Morgan, “High speed multi-frequency impedance analysis of single particles in a microfluidic cytometer using maximum length sequences.,” *Lab Chip*, vol. 7, no. 8, pp. 1034–40, Aug. 2007.

[41] K. Braeckmans, S. C. De Smedt, M. Leblans, R. Pauwels, and J. Demeester, “Encoding microcarriers: Present and future technologies,” *Nature Reviews Drug Discovery*, vol. 1, no. 6. pp. 447–456, 2002.

[42] K. Khoshmanesh, S. Nahavandi, S. Baratchi, A. Mitchell, and K. Kalantar-zadeh, “Dielectrophoretic platforms for bio-microfluidic systems.,” *Biosens. Bioelectron.*, vol. 26, no. 5, pp. 1800–14, Jan. 2011.

[43] Y. Demircan, E. Özgür, and H. Külah, “Dielectrophoresis: applications and future outlook in point of care.,” *Electrophoresis*, vol. 34, no. 7, pp. 1008–27, Apr. 2013.

[44] I. Doh and Y.-H. Cho, “A continuous cell separation chip using hydrodynamic dielectrophoresis (DEP) process,” *Sensors Actuators A Phys.*, vol. 121, no. 1, pp. 59–65, May 2005.

[45] S.-I. Han, S.-M. Lee, Y.-D. Joo, and K.-H. Han, “Lateral dielectrophoretic microseparators to measure the size distribution of blood cells.,” *Lab Chip*, vol. 11, no. 22, pp. 3864–72, Nov. 2011.

[46] K. Ahn, C. Kerbage, T. P. Hunt, R. M. Westervelt, D. R. Link, and D. A. Weitz, “Dielectrophoretic manipulation of drops for high-speed microfluidic sorting devices,” *Appl. Phys. Lett.*, vol. 88, no. 2, p. 024104, Jan. 2006.

[47] J.-H. So and M. D. Dickey, “Inherently aligned microfluidic electrodes composed of liquid metal.,” *Lab Chip*, vol. 11, no. 5, pp. 905–11, Mar. 2011.

[48] A. C. Siegel, S. S. Shevkoplyas, D. B. Weibel, D. A. Bruzewicz, A. W. Martinez, and G. M. Whitesides, “Cofabrication of electromagnets and microfluidic systems in poly(dimethylsiloxane).,” *Angew. Chem. Int. Ed. Engl.*, vol. 45, no. 41, pp. 6877–82, Oct. 2006.

[49] A. C. Siegel, D. A. Bruzewicz, D. B. Weibel, and G. M. Whitesides, “Microsolidics: Fabrication of Three-Dimensional Metallic Microstructures in Poly(dimethylsiloxane),” *Adv. Mater.*, vol. 19, no. 5, pp. 727–733, Mar. 2007.

[50] H. Morgan, T. Sun, D. Holmes, S. Gawad, and N. G. Green, “Single cell dielectric spectroscopy,” *J. Phys. D. Appl. Phys.*, vol. 40, no. 1, pp. 61–70, Jan. 2007.

[51] J.-C. Baret, O. J. Miller, V. Taly, M. Ryckelynck, A. El-Harrak, L. Frenz, C. Rick, M. L. Samuels, J. B. Hutchison, J. J. Agresti, D. R. Link, D. A. Weitz, and A. D. Griffiths, “Fluorescence-activated droplet sorting (FADS): efficient microfluidic cell sorting based on enzymatic activity.,” *Lab Chip*, vol. 9, no. 13, pp. 1850–8, Jul. 2009.

[52] J. Y. Kim, J. Y. Baek, K. A. Lee, and S. H. Lee, “Automatic aligning and bonding system of PDMS layer for the fabrication of 3D microfluidic channels,” *Sensors Actuators A Phys.*, vol. 119, no. 2, pp. 593–598, Apr. 2005.

[53] M. Demori, V. Ferrari, P. Poesio, and D. Strazza, “A microfluidic capacitance sensor for fluid discrimination and characterization,” *Sensors Actuators A Phys.*, vol. 172, no. 1, pp. 212–219, Dec. 2011.

[54] A. M. Streets and Y. Huang, “Chip in a lab: Microfluidics for next generation life science research.,” *Biomicrofluidics*, vol. 7, no. 1, p. 11302, Jan. 2013.

[55] R. M. Guijt, J. P. Armstrong, E. Candish, V. Lefleur, W. J. Percey, S. Shabala, P. C. Hauser, and M. C. Breadmore, “Microfluidic chips for capillary electrophoresis with integrated electrodes for capacitively coupled conductivity detection based on printed circuit board technology,” *Sensors Actuators B Chem.*, vol. 159, no. 1, pp. 307–313, Nov. 2011.

[56] E. W. M. Kemna, L. I. Segerink, F. Wolbers, I. Vermes, and A. van den Berg, “Label-free, high-throughput, electrical detection of cells in droplets.,” *Analyst*, vol. 138, no. 16, pp. 4585–92, Aug. 2013.

[57] S. K. Ameri, P. K. Singh, M. R. Dokmeci, A. Khademhosseini, Q. Xu, and S. R. Sonkusale, “All electronic approach for high-throughput cell trapping and lysis with electrical impedance monitoring.,” *Biosens. Bioelectron.*, vol. 54, pp. 462–7, Apr. 2014.

[58] R. Prakash, K. Pabbaraju, S. Wong, A. Wong, R. Tellier, and K. V. I. S. Kaler, “Droplet Microfluidic Chip Based Nucleic Acid Amplification and Real-Time Detection of Influenza Viruses,” *J. Electrochem. Soc.*, vol. 161, no. 2, pp. B3083–B3093, Dec. 2013.

[59] T. Vu Quoc, H. Nguyen Dac, T. Pham Quoc, D. Nguyen Dinh, and T. Chu Duc, “A printed circuit board capacitive sensor for air bubble inside fluidic flow detection,” *Microsyst. Technol.*, vol. 21, no. 4, pp. 911–918, Apr. 2014.

[60] Y. Li and K. V. I. S. Kaler, “Dielectrophoretic fluidic cell fractionation system,” *Anal. Chim. Acta*, vol. 507, no. 1, pp. 151–161, Apr. 2004.

[61] L. J. Millet, K. Park, N. N. Watkins, K. J. Hsia, and R. Bashir, “Separating beads and cells in multi-channel microfluidic devices using dielectrophoresis and laminar flow.,” *J. Vis. Exp.*, no. 48, Jan. 2011.

[62] T. Braschler, N. Demierre, E. Nascimento, T. Silva, A. G. Oliva, and P. Renaud, “Continuous separation of cells by balanced dielectrophoretic forces at multiple frequencies.,” *Lab Chip*, vol. 8, no. 2, pp. 280–6, Feb. 2008.

[63] E. M. Nascimento, N. Nogueira, T. Silva, T. Braschler, N. Demierre, P. Renaud, and A. G. Oliva, “Dielectrophoretic sorting on a microfabricated flow cytometer: label free separation of Babesia bovis infected erythrocytes.,” *Bioelectrochemistry*, vol. 73, no. 2, pp. 123–8, Aug. 2008.

[64] M. D. Vahey and J. Voldman, “An equilibrium method for continuous-flow cell sorting using dielectrophoresis.,” *Anal. Chem.*, vol. 80, no. 9, pp. 3135–43, May 2008.

[65] J. Voldman, M. L. Gray, M. Toner, and M. A. Schmidt, “A microfabrication-based dynamic array cytometer.,” *Anal. Chem.*, vol. 74, no. 16, pp. 3984–90, Aug. 2002.

[66] J. Cheng, E. L. Sheldon, L. Wu, M. J. Heller, and J. P. O’Connell, “Isolation of Cultured Cervical Carcinoma Cells Mixed with Peripheral Blood Cells on a Bioelectronic Chip,” *Anal. Chem.*, vol. 70, no. 11, pp. 2321–2326, Jun. 1998.

[67] L. Mazutis, J. Gilbert, W. L. Ung, D. A. Weitz, A. D. Griffiths, and J. A. Heyman, “Single-cell analysis and sorting using droplet-based microfluidics.,” *Nat. Protoc.*, vol. 8, no. 5, pp. 870–91, May 2013.